

Postseismic Deformation Following the 2010 $M = 7.2$ El Mayor-Cucapah Earthquake: Observations, Kinematic Inversions, and Dynamic Models

CHRISTOPHER ROLLINS,¹ SYLVAIN BARBOT,² and JEAN-PHILIPPE AVOUAC^{1,3}

Abstract—Due to its location on a transtensional section of the Pacific-North American plate boundary, the Salton Trough is a region featuring large strike-slip earthquakes within a regime of shallow asthenosphere, high heat flow, and complex faulting, and so postseismic deformation there may feature enhanced viscoelastic relaxation and afterslip that is particularly detectable at the surface. The 2010 $M = 7.2$ El Mayor-Cucapah earthquake was the largest shock in the Salton Trough since 1892 and occurred close to the US-Mexico border, and so the postseismic deformation recorded by the continuous GPS network of southern California provides an opportunity to study the rheology of this region. Three-year postseismic transients extracted from GPS displacement time-series show four key features: (1) 1–2 cm of cumulative uplift in the Imperial Valley and ~1 cm of subsidence in the Peninsular Ranges, (2) relatively large cumulative horizontal displacements > 150 km from the rupture in the Peninsular Ranges, (3) rapidly decaying horizontal displacement rates in the first few months after the earthquake in the Imperial Valley, and (4) sustained horizontal velocities, following the rapid early motions, that were still visibly ongoing 3 years after the earthquake. Kinematic inversions show that the cumulative 3-year postseismic displacement field can be well fit by afterslip on and below the coseismic rupture, though these solutions require afterslip with a total moment equivalent to at least a $M = 7.2$ earthquake and higher slip magnitudes than those predicted by coseismic stress changes. Forward modeling shows that stress-driven afterslip and viscoelastic relaxation in various configurations within the lithosphere can reproduce the early and later horizontal velocities in the Imperial Valley, while Newtonian viscoelastic relaxation in the asthenosphere can reproduce the uplift in the Imperial Valley and the subsidence and large westward displacements in the Peninsular Ranges. We present two forward models of dynamically coupled deformation mechanisms that fit the postseismic transient well: a model combining afterslip in the lower crust, Newtonian viscoelastic relaxation in a localized zone in the lower crust beneath areas of high heat flow and geothermal activity, and Newtonian viscoelastic relaxation in the asthenosphere; and a second model that replaces the afterslip in the

first model with viscoelastic relaxation with a stress-dependent viscosity in the mantle. The rheology of this high-heat-flow, high-strain-rate region may incorporate elements of both these models and may well be more complex than either of them.

1. Introduction

In addition to earthquakes, the earth's lithosphere accommodates tectonic strain through aseismic processes such as slow slip on faults, bulk ductile flow, and elastic deformation coupled with pore fluid motion. A large earthquake imparts stress changes to the crust and mantle that can accelerate these processes: segments of faults surrounding the coseismic rupture may be driven to slip aseismically (e.g., MARONE *et al.* 1991; HEARN *et al.* 2002; PERFETTINI and AVOUAC 2004; FREED 2007); sections of the crust and mantle may behave viscoelastically, relaxing coseismic elastic stress changes through ductile flow (e.g., NUR and MAVKO 1974; DENG *et al.* 1998; POLLITZ 2003); and pore fluids may move away from areas of increased pressure (e.g., PELTZER *et al.* 1998; JONSSON *et al.* 2003; FIALKO 2004). These processes may cause observable transient displacement at the surface, and the measurement of this transient with geodetic methods can in principle be used to identify the associated processes, thereby shedding light on the rheology of the crust and mantle. The Salton Trough is a region where surface displacements due to these processes may be particularly detectable. Located on a transtensional section of the Pacific-North American plate boundary in southernmost California and northwestern Mexico, this region represents a transition between the transform tectonics of southern California to the northwest and the

¹ Division of Geological and Planetary Sciences, California Institute of Technology, Pasadena, USA. E-mail: jrollin@caltech.edu

² Earth Observatory of Singapore, Nanyang Technological University, Singapore, Singapore.

³ Department of Earth Sciences, University of Cambridge, Cambridge, UK.

extensional regime of the East Pacific Rise to the southeast. The extensional component of relative plate motion has thinned the lithosphere, bringing the low-viscosity asthenosphere up to within ~ 45 km of the surface (compared to a regional average of ~ 80 km) (LEKIC *et al.* 2011) (Fig. 1), and the very high heat flow and geothermal activity in this region (e.g., LACHENBRUCH *et al.* 1985) imply that viscosities are also reduced in the crust (e.g., WILLIAMS *et al.* 2012). Meanwhile, the transform component of relative plate motion is accommodated by large strike-slip earthquakes that impart large stress changes to this structure, as well as a complex array of faults that may slip aseismically (e.g., RYMER *et al.* 2011). The 2010 $M = 7.2$ El Mayor-Cucapah earthquake was the largest shock in the Salton Trough since at least 1892 (HAUKSSON *et al.* 2011) and may have induced significant viscoelastic relaxation, afterslip, and poroelastic rebound, and so the surface deformation following this earthquake may yield unique insights into the rheology of this region. This earthquake also provides a unique opportunity to determine whether a rheological structure inferred by seismic methods—the (LEKIC *et al.* 2011) lithosphere–asthenosphere boundary—is also visible in geodetic deformation. A previous study of deformation following this earthquake (POLLITZ *et al.* 2012) found that the postseismic velocity field did indeed suggest a laterally heterogeneous rheological structure in the upper mantle beneath the Salton Trough. A more recent study (GONZALEZ-ORTEGA *et al.* 2014) found that early near-field GPS and InSAR displacements in Mexico could be fit to afterslip on the coseismic rupture but that geodetic displacements farther from the rupture required a longer-wavelength mechanism, for which they suggested distributed viscoelastic relaxation.

2. Coseismic Deformation and Implications for Postseismic Relaxation

The El Mayor-Cucapah earthquake ruptured ~ 110 km of a series of northwest-striking faults within the Sierra Cucapah and Sierra El Mayor ranges on the west side of the Mexicali Valley, just south of the US/Mexico border (HAUKSSON *et al.* 2011). WEI *et al.* (2011) used a joint inversion of seismic,

geodetic, and remote sensing data to produce a best-fitting rupture model for the earthquake. Although the surface rupture followed a roughly linear trace, the dominant slip surface at depth swung over from a southwest-dipping plane to a northeast-dipping plane over the length of the rupture. The earthquake featured approximately a 2:1 ratio of right-lateral to normal slip. We model the coseismic displacement and strain fields produced by the WEI *et al.* (2011) slip model in an elastic halfspace using Coulomb 3.3 (TODA *et al.* 2005; LIN and STEIN 2004). Both elastic modeling and coseismic vertical displacements at UNAVCO GPS stations (discussed in the next section) indicate that the Imperial Valley underwent uplift during the mainshock (Fig. 2a), a perhaps surprising finding given that the region north of a northwest-striking, right-lateral earthquake should be an extensional quadrant in seismological terms, where the first recorded motion should be downward. Cross sections of the coseismic displacement and strain fields (Fig. 2b) reveal that the crust and mantle in the Imperial Valley were pulled upwards and southeast towards the rupture during the mainshock, uplifting the surface there. The vertical extension ϵ_{zz} under the Imperial Valley was positive at >50 km depth, beneath the LEKIC *et al.* (2011) lithosphere–asthenosphere boundary, but negative at 20–30 km depth in the lower crust and mantle lithosphere. This distribution of coseismic uplift, subsidence and strain at depth may be characteristic of surface-rupturing strike-slip earthquakes (Fig. 2b). The normal component of coseismic slip imparted a similar vertical strain distribution beneath the rupture, with vertical extension at > 50 km depth, but vertical compression at 20–30 km depth (Fig. 3b). As we will show, this strain field has important implications for the simulated viscoelastic responses of the asthenosphere, lower crust, and mantle lithosphere.

3. GPS Data and Extraction of Postseismic Displacement Time Series

The UNAVCO Plate Boundary Observatory's network of continuous GPS stations provided coverage of surface deformation north of the US-Mexico border before, during, and after the El Mayor-

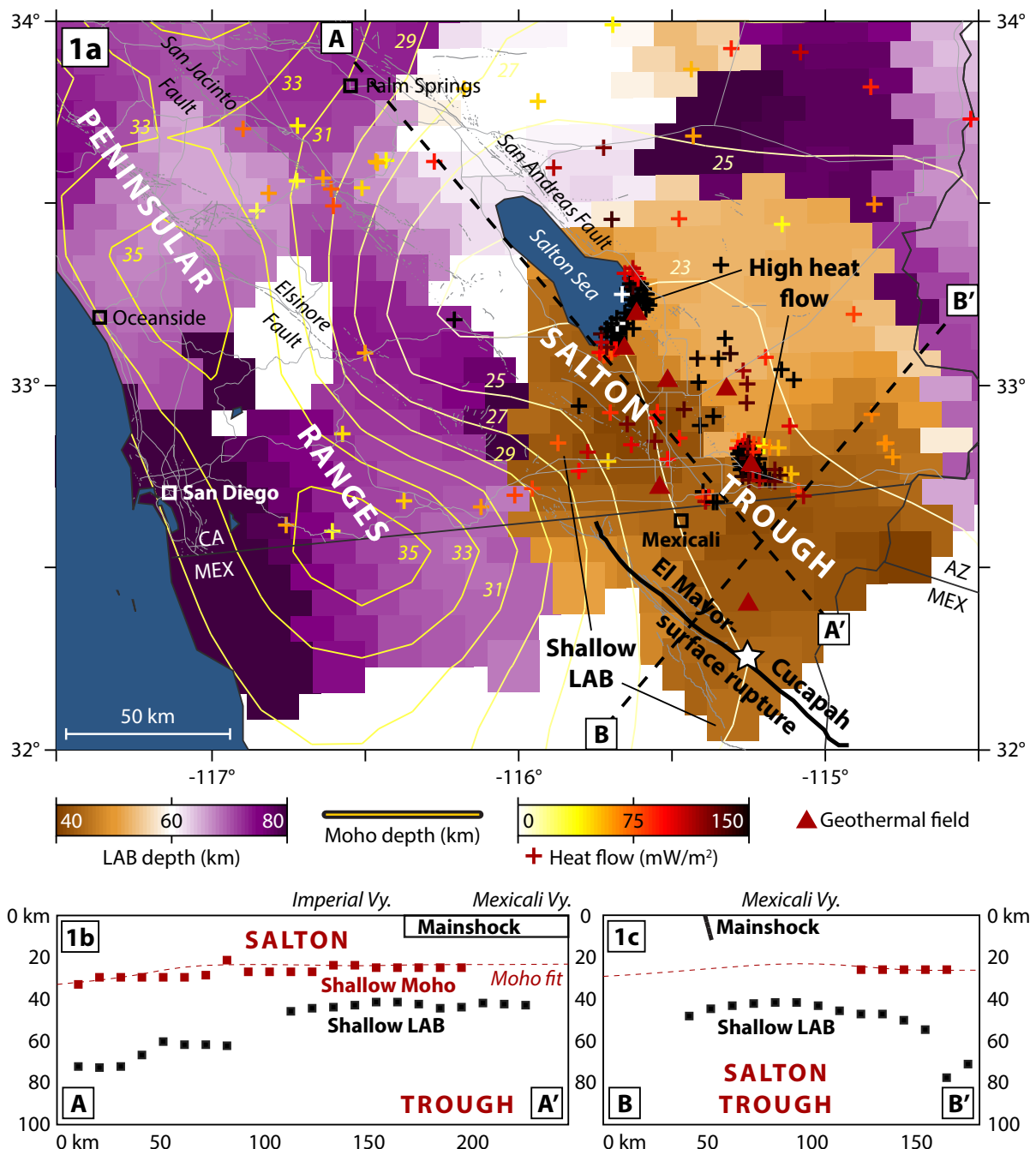


Figure 1

a The El Mayor-Cucapah earthquake occurred in the Salton Trough, a region featuring a shallow lithosphere–asthenosphere boundary (colored surface; data from LEKIC *et al.* 2011), shallow Moho (yellow contours; data from TAPE *et al.* 2012), high heat flow (brown crosses; data from USGS California Heat Flow Data Map), and geothermal activity (red triangles). **b, c** Cross sections through the Salton Trough, respectively, adapted from cross sections FF' and EE' in LEKIC *et al.* (2011), show that the earthquake occurred above shallow lithosphere–asthenosphere boundary and Moho

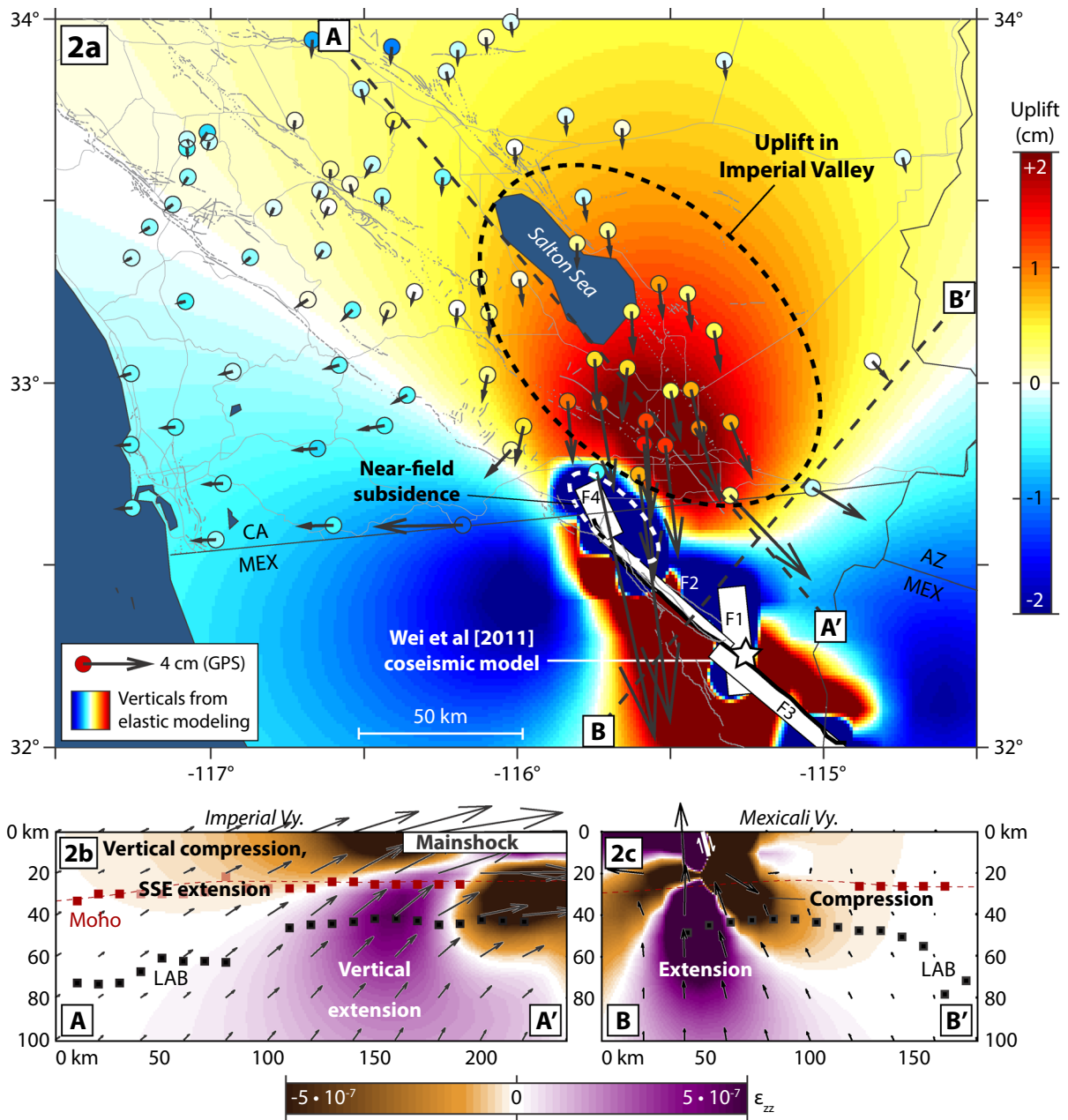


Figure 2

a Coseismic displacements at UNAVCO GPS stations (arrows are horizontal displacements; colored circles are vertical displacements) and in elastic modeling using the Wei *et al.* (2011) slip model for the El Mayor-Cucapah earthquake (colored surface represents modeled vertical displacements) indicate coseismic uplift in the Imperial Valley, a seismological extensional quadrant. **b, c** Cross sections of coseismic displacement and vertical extension ϵ_{zz} in elastic modeling show that material beneath the Imperial Valley was pulled upward and towards the rupture, uplifting the surface there and causing vertical extension below ~ 40 km depth and compression above that. The normal component of slip also pulled material upward beneath the rupture

Cucapah earthquake. The Scripps Orbit Processing and Array Center (SOPAC; sopac.ucsd.edu) uses the GAMIT/GLOBK processing software to produce

daily three-component position time series for each UNAVCO station. These time series contain a linear trend due to continuous plate motions; annual and

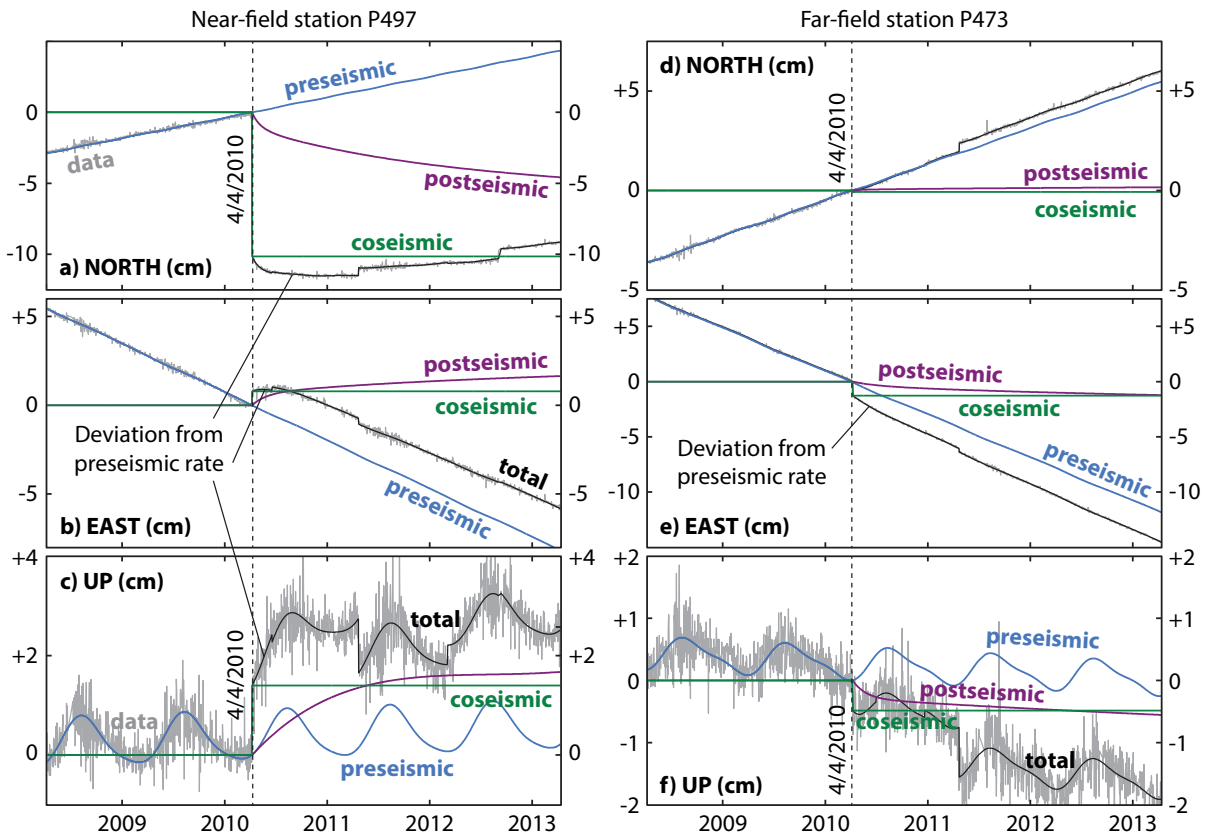


Figure 3

We extract coseismic and postseismic displacement signals from daily three-component position time series at UNAVCO GPS stations. **a–c** Time series at near-field station P497 show clear southward, eastward, and upward deviations from background rates following the mainshock. **d–f** Postseismic signals are more subtle at far-field station P473 but a westward postseismic transient is visible

semiannual oscillations; instantaneous offsets from earthquakes, station maintenance, and changes in processing methods; the offsets associated with the El Mayor-Cucapah mainshock; and finally, the decaying transient signal of postseismic deformation (Fig. 3). We use nonlinear least-squares to fit the time series to

$$\begin{aligned} x(t) = & C_1 + C_2 t + C_3 \sin(2\pi t) + C_4 \cos(2\pi t) \\ & + C_5 \sin(4\pi t) + C_6 \cos(4\pi t) + C_7 H(t) \\ & + C_8 \log(1 + t/C_9) + C_{10}(1 - \exp(-t/C_{11})) \\ & + D_i H(t - t_i) \end{aligned} \quad (1)$$

where C_1 is a constant offset, C_2 is the secular velocity, C_3 and C_4 are coefficients of the annual oscillation, C_5 and C_6 are coefficients of the semi-annual oscillation, C_7 is the magnitude of the coseismic offset, C_8 is the magnitude of a logarithmic decay function with characteristic time C_9 , C_{10} is the

magnitude of an exponential decay with characteristic time C_{11} , and D_i are the magnitudes of instantaneous offsets at times t_i represented by the Heaviside step functions $H(t - t_i)$. In this scheme the postseismic transient is fit to the combination of the logarithmic and exponential functions. Partly because of noise in the data, nonlinear least-squares has the potential to become caught in local minima and potentially miss the best-fitting decay parameters. To reduce the effect of this, we run nonlinear least-squares on the time series ten times using ten different pairs of initial values for C_9 and C_{11} randomized in log space between 0.1 and 10, then use the average of the ten best-fit decays as the comprehensive best-fit transient. To estimate the uncertainty in the fit due to noise and uncertainty in the data, we generate four supplementary time series consisting of the data plus a vector of Gaussian noise multiplied by

the SOPAC daily formal position errors, run the process ten times on each supplementary time series (with initial relaxation times randomized as before) to generate 40 alternative decays, and estimate the daily uncertainty in each component of position as the daily root-mean-squared difference between the 40 alternatives and the comprehensive best-fit decay. This method produces estimates of coseismic and cumulative postseismic displacements that are generally quite similar to those estimated by SOPAC (Figs. 22, 23). As a result of using a single decay function, the SOPAC methodology incorrectly ascribes some of the very early horizontal displacements in the Imperial Valley to coseismic displacement (Fig. 22b), while our method correctly separates the two (Fig. 3a).

Following the earthquake, UNAVCO installed a set of continuous GPS stations near the rupture in Mexico to image postseismic deformation there. These stations did not record the first segment of postseismic deformation, making estimates of total postseismic displacements intractable, and they do not contain preseismic time series from which linear motion rates and periodic oscillations could be reliably extracted. However, PLATTNER *et al.* (2007) calculated linear motion rates at sites near these stations using a previously installed campaign GPS network, and POLLITZ *et al.* (2012) estimated velocities of postseismic deformation at these stations by subtracting off the linear motion rate from the nearest PLATTNER *et al.* (2007) site to each station. We follow the same practice as POLLITZ *et al.* (2012) to obtain partial estimated time series of horizontal deformation at those stations.

4. Extracted Postseismic Displacements

Extracted postseismic transients in the first 3 years after the mainshock feature four key characteristics (Fig. 4). First, cumulative 3-year displacements include 1–2 cm of uplift in the Imperial Valley and ~1 cm of subsidence in the Peninsular Ranges relative to background rates (Fig. 4b). The uplift in the Imperial Valley can be robustly linked to postseismic processes because of its sign, magnitude, and

duration. GPS stations there were observed to be subsiding at ~0–4 mm/year prior to the earthquake, as expected for a region undergoing extension (CROWELL *et al.* 2013), meaning that the extracted postseismic uplift is both too large and of the wrong sign to be explainable by steady-state tectonic processes. It is also unlikely to result from seasonal surface processes; it appears to occur steadily over 18 months (Fig. 4b), and the dominant surface signal following an earthquake in April should be subsidence, not uplift, due to lowering of the water table during the dry summer. Second, cumulative horizontal postseismic displacements are approximately half the magnitude of horizontal coseismic displacements in the Imperial Valley, but of approximately equal magnitude to them > 150 km west of the rupture in the Peninsular Ranges (Fig. 4a), suggesting that a deep, long-wavelength deformation process featured in postseismic deformation. Third, displacement time series at stations in both the Imperial Valley and Peninsular Ranges feature rapidly decaying horizontal velocities in the first few months after the mainshock. Fourth, these rapid early motions decay to sustained horizontal velocities that were still visibly ongoing 3 years after the mainshock (Fig. 4b).

5. Kinematic Inversions for Afterslip

Fault zones may extend down into the lower crust and perhaps the mantle as discrete interfaces that may slip aseismically in response to coseismic stress changes (e.g., HEARN *et al.* 2002; PERFETTINI and AVOUAC 2004; BÜRGMANN and DRESEN 2008). To determine whether the entire postseismic displacement pattern can be explained by afterslip, we invert cumulative 3-year postseismic displacements (purple arrows in Fig. 4a, black arrows in Fig. 24b and all subsequent figures showing surface displacements) for slip on the principal rupture planes of the WEI *et al.* (2011) coseismic slip model and/or modeled downward extensions of those planes into the lower crust and mantle lithosphere, in various combinations. We run inversions for slip in five different depth ranges: (1) on the coseismic rupture, between 0 and 12 km downdip from the top edges of planes F2, F3, and F4 of the (WEI *et al.* 2011) coseismic model

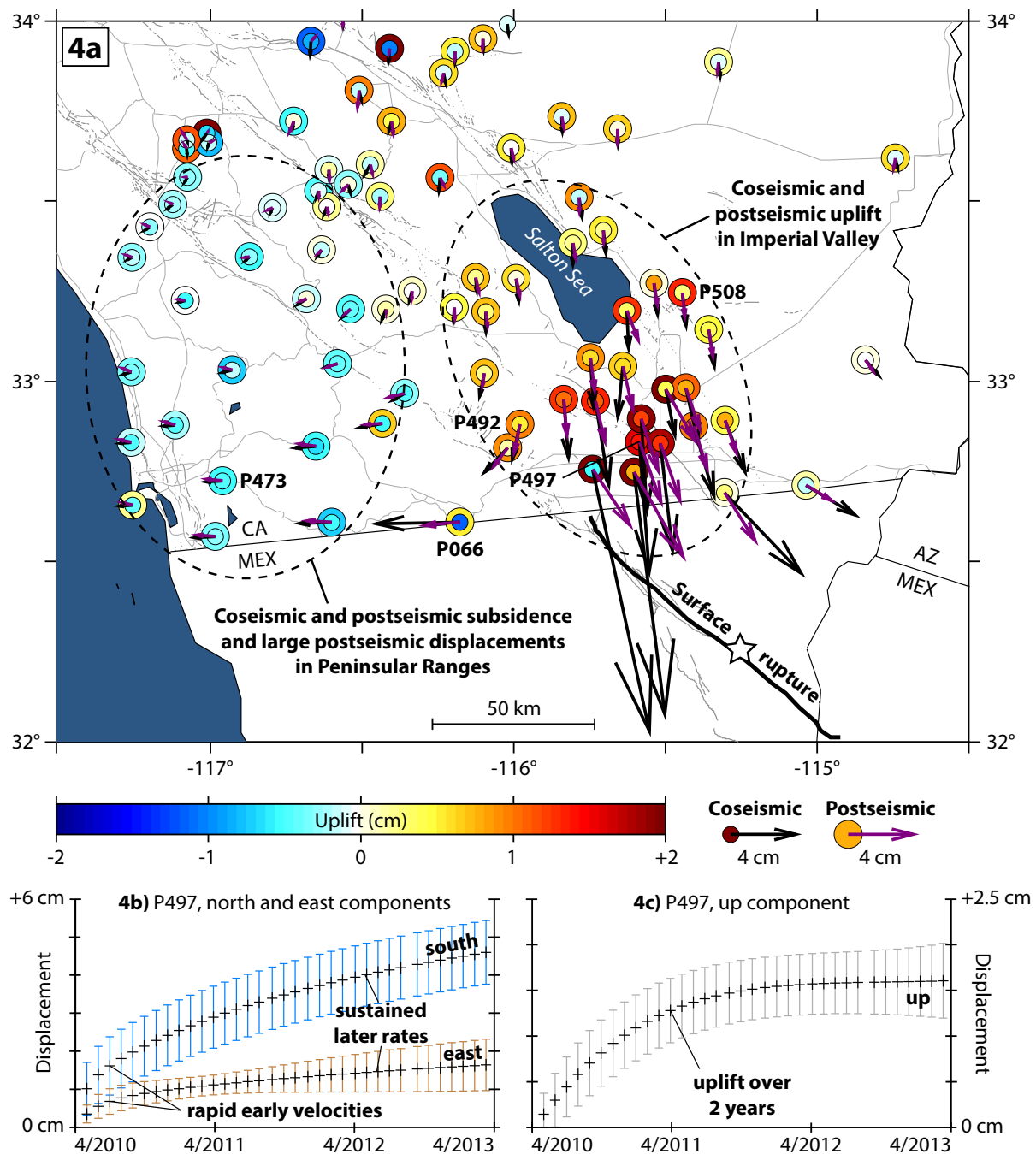


Figure 4

a Comparison of coseismic displacements (black arrows and small shaded circles) and cumulative 3-year extracted postseismic displacements (purple arrows and large shaded circles) shows that the postseismic deformation, like the coseismic, includes uplift in the Imperial Valley and subsidence in the Peninsular Ranges, and that horizontal postseismic displacements are approximately half the magnitude of coseismic horizontals in the near-field but equal in the far-field. **b, c** Extracted time series at station P497 show rapidly decaying horizontal motion rates in the first postseismic year followed by sustained horizontal motion that was still ongoing three years after the mainshock. Gray bars here and in subsequent time series figures are noise-based estimates of daily uncertainties in extracted postseismic decays

(Fig. 24); (2) on modeled downward extensions of planes F2 and F3 into the lower crust, between 12 and 24 km downdip from the top edges of those planes (extending approximately down to the TAPE *et al.* 2012 Moho) (Fig. 25); (3) on both the coseismic rupture and the modeled lower crustal extensions (Fig. 26); (4) on the downward extensions of planes F2 and F3 into the lower crust and mantle lithosphere, between 12 and 48 km downdip from the top edges of those planes (extending approximately down to the LEKIC *et al.* 2011 lithosphere–asthenosphere boundary) (Figs. 5, 27) on both the coseismic rupture and the modeled downward extensions into the lower crust and mantle lithosphere (Fig. 5). Slip plane F2, comprising most of the northwest half of the rupture, dips 75° to the northeast, while slip plane F3, comprising the southeast half, dips 60° to the southwest. In the geometries allowing slip on the downward extensions of these planes, we experiment with geometries in which (1) the downward extensions have the same dips as the coseismic planes; (2) the downward extensions dip 15° more shallowly than the planes do on the coseismic rupture; and (3) the downward extensions are vertical. We also allow slip on a 30-km-long segment extending northwest from the northwest end of plane F2 into the Yuha Desert, the site of distributed surface creep following the earthquake (RYMER *et al.* 2011) and a rich aftershock sequence (KROLL *et al.* 2013) including a $M = 5.7$ aftershock in June 2010. [For reference, POLLITZ *et al.* (2012) found that this deformation was well fit by slip on a similar 45-km-long dislocation extending northwest from the rupture.] This slip plane is assigned a vertical dip and in each inversion, it extends to the same depth that the main slip planes do. For consistency with coseismic slip, we enforce that the rake of the slip is between 180° (pure right-lateral) and −90° (pure normal). We subdivide the slip into square patches 6 km on a side and regularize the inversions using the $S^{-1/2}T$ methodology of ORTEGA (2013), where S is the matrix describing the data's sensitivity to slip on each patch (calculated as the diagonal of $G^T W_x G$, where G is the Green's function matrix and W_x is the matrix of uncertainty estimates in each component of 3-year transient displacements at each station, calculated using the aforementioned method) and T is the Laplacian

operator. As described in ORTEGA (2013), the matrix $S^{-1/2}T$ must be multiplied by a prefactor ϵ to be of suitable magnitude as a smoothing matrix. We find that the highest value in S —the sensitivity of the misfit to normal slip on the northwesternmost, shallowest patch on plane F4, approximately 4.1×10^{-4} —is a suitable value for ϵ , yielding a scheme that visibly heavily smoothes patches far into Mexico and at depth while allowing for visible spatial heterogeneity in slip on the segments closest to the southern California GPS network (e.g. Fig. 25). Other details of the inversion technique are given in BARBOT *et al.* (2013).

The inversion for afterslip on the coseismic rupture fits most of the 3-year cumulative displacement field, achieving a variance reduction of 97 % in horizontal displacements and 63 % in vertical displacements (Fig. 24). Because of the first-order similarities between the coseismic and postseismic displacement fields, particularly in vertical displacements (Fig. 4), it is not surprising that further slip on the coseismic rupture can fit most of the postseismic displacement field. In terms of the verticals, uniform slip between 0 and 10 km depth on a northwest-striking fault should produce uplift north of the rupture (Fig. 21a), and thus the inversions that allow for slip to the surface should have no problem reproducing the uplift in the Imperial Valley barring other factors. However, the inversion assigns up to 1.7 m of right-lateral slip on plane F2 and up to 3.3 m of right-lateral slip and 1.4 m of normal slip on plane F3, equivalent in total moment to an $M = 7.2$ earthquake, the same magnitude as the mainshock (Fig. 24). Allowing slip at greater depth does not reduce the total moment of slip required, but does smear the slip over a greater area and reduces the maximum slip required: the inversion that allows for slip on the downward lower crustal extensions of planes F2 and F3 as well as on the coseismic rupture (Fig. 26) assigns up to 2.2 m right-lateral slip and 1.1 m normal slip on plane F3, and the inversion that allows for slip into the mantle lithosphere as well as on the coseismic rupture (Fig. 5) assigns only up to 1.4 m right-lateral slip on plane F2 and 1.2 m right-lateral slip and 0.7 m normal slip on plane F3. Making the dips of the downward extensions 15° shallower than on the coseismic rupture has little effect on the fit to the displacement field, though making the downward

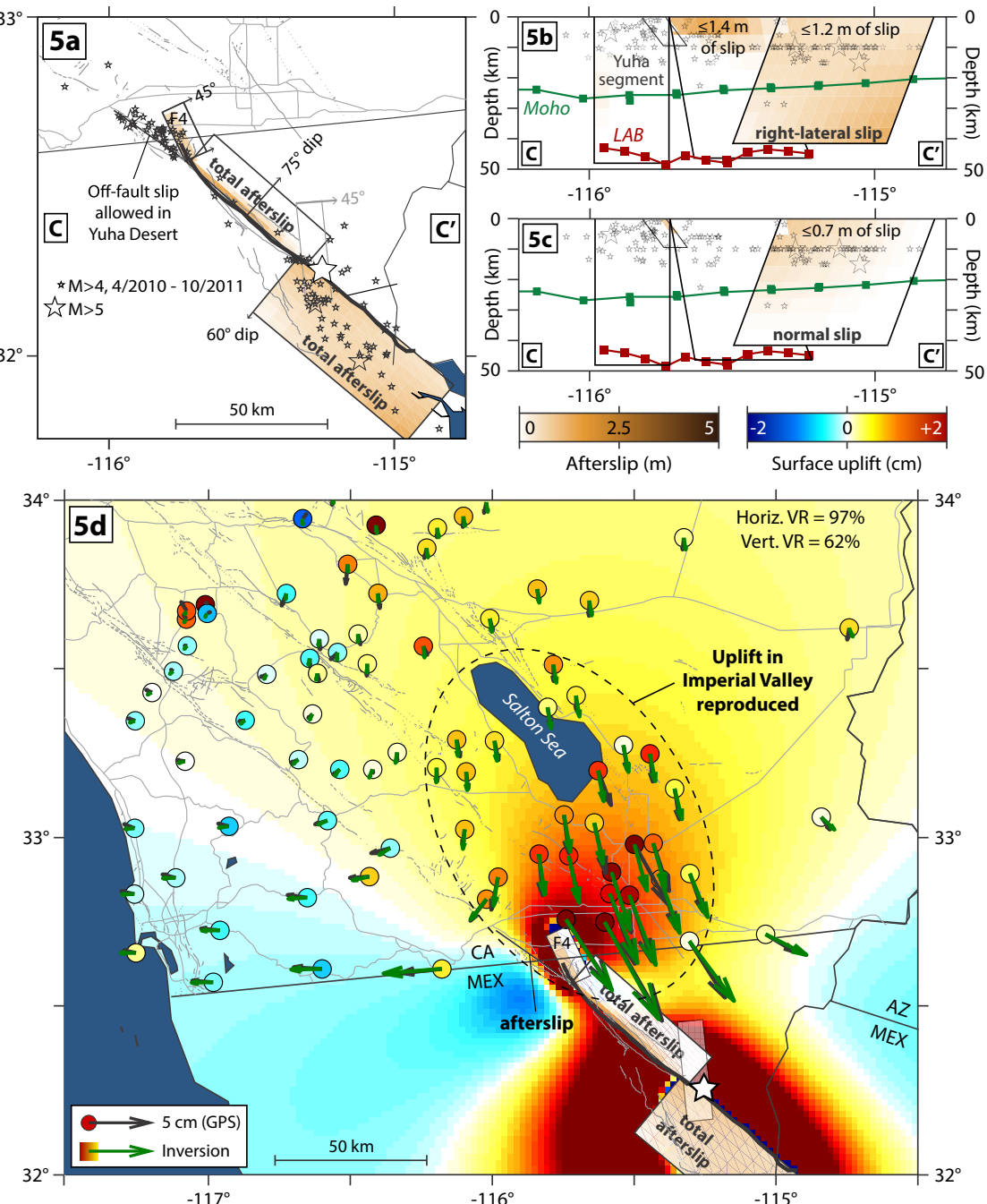


Figure 5

Inversion of 3-year cumulative postseismic GPS displacements for afterslip on the main coseismic rupture planes, on modeled downward extensions of the coseismic rupture planes into the lower crust and mantle lithosphere, and in the Yuha Desert. **a** Slip is allowed on planes F2, F3, and F4 of the Wei *et al.* (2011) model for the mainshock (between 0 and 12 km downdip from their top edges) and on downward extensions of F2 and F3 to the lithosphere–asthenosphere boundary (between 12 and 48 km downdip). Slip is also allowed on a 30-km long segment extending northwest into the Yuha Desert to fit the aftershocks and surface creep there to first order and any possible creep at greater depth; this segment has a vertical dip and extends to 48 km depth; **b, c** The inversion assigns up to 1.4 m of right-lateral slip on plane F2 and up to 1.2 m of right-lateral slip and 0.7 m of normal slip on the downward extension of plane F3, equivalent in total moment to a $M = 7.2$ earthquake. **d** The inversion produces variance reductions of 97 and 62 % in horizontal and vertical displacements, respectively

Table 1

Variance reductions of cumulative 3-year horizontal and vertical postseismic displacements in the kinematic inversions

| Inversion setup | Slip on coseismic rupture | Between rupture and Moho | Between Moho and LAB | Variance reduction (%) | |
|-----------------|---------------------------|--------------------------|----------------------|------------------------|----------|
| | | | | Horizontal | Vertical |
| Yes | No | No | No | 97 | 63 |
| Yes | Coseismic dips | No | No | 97 | 63 |
| Yes | Vertical dips | No | No | 97 | 62 |
| Yes | Dips 15° shallower | No | No | 97 | 63 |
| No | Coseismic dips | No | No | 94 | 49 |
| No | Vertical dips | No | No | 94 | 36 |
| No | Dips 15° shallower | No | No | 95 | 50 |
| No | Coseismic dips | Coseismic dips | Coseismic dips | 94 | 47 |
| No | Vertical dips | Vertical dips | Vertical dips | 94 | 31 |
| No | Dips 15° shallower | Dips 15° shallower | Dips 15° shallower | 95 | 47 |
| Yes | Coseismic dips | Coseismic dips | Coseismic dips | 97 | 62 |
| Yes | Vertical dips | Vertical dips | Vertical dips | 97 | 62 |
| Yes | Dips 15° shallower | Dips 15° shallower | Dips 15° shallower | 98 | 63 |

extensions vertical significantly reduces the fit to vertical displacements (Table 1).

As discussed previously, postseismic horizontal displacements were approximately half the magnitude of coseismic displacements in the near-field but of similar magnitude in the far-field, suggesting that postseismic deformation may have involved a deeper, longer-wavelength mechanism than a simple continuation of coseismic slip, and the contributions of slip in the lower crust and mantle in the inversions that allow for it are consistent with this. However, the inversions that disallow afterslip in the seismogenic zone have significantly more trouble fitting the pattern of vertical displacements. Uniform slip below the seismogenic depth range on a northwest-striking fault should produce subsidence north of the rupture (Fig. 21c), and so inversions that only allow for slip below the seismogenic depth range will struggle to reproduce the postseismic uplift in the Imperial Valley. The inversion that allows for slip on the downward lower crustal extensions of planes F2 and F3 without allowing slip on the coseismic rupture above them (Fig. 25) requires several meters of both right-lateral and normal slip on the lower crustal extension of plane F3—equivalent in total moment to an $M = 7.3$ earthquake, greater than the mainshock—and achieves only a 49 % variance reduction in the vertical displacement field, visibly fitting the uplift in the Imperial Valley and the subsidence in the Peninsular Ranges less well. As before, allowing for slip into the

mantle helps reduce the maximum slip required (Fig. 27), but does not help fit the vertical displacements, achieving only a 47 % variance reduction in the verticals and still requiring slip equivalent to an $M = 7.3$ earthquake.

The observation that slip on the coseismic rupture alone can fit the 3-year cumulative horizontal and vertical displacement field well, and that allowing slip at greater depth reduces the maximum slip required, suggests that much of the spatio-temporal postseismic transient in southern California may be explainable by some combination of shallow and deep afterslip. However, the requirement of a total moment of slip equivalent to at least an $M = 7.2$ earthquake may make these solutions physically implausible. We thus turn to forward modeling to determine whether simulated afterslip driven by coseismic stress changes can achieve the magnitudes of slip required by the kinematic inversions and can reproduce the time evolution of displacements observed at GPS stations.

6. Forward Modeling Methodology

We use Relax (geodynamics.org/cig/software/relax) to simulate the coseismic stress changes imparted by the Wei *et al.* (2011) coseismic slip model for the El Mayor-Cucapah earthquake to the surrounding medium, the relaxation of those

mechanisms by hypothesized postseismic processes, and the spatio-temporal evolution of surface deformation that would result from each process. At each time step, Relax simulates all postseismic mechanisms as equivalent body forces in a generalized viscoelastoplastic halfspace, allowing for the simulation of multiple dynamically coupled mechanisms relaxing coseismic stress changes in concert (BARBOT and FIALKO 2010a, b). The use of an elastic halfspace (here with a uniform shear modulus of $\mu = 30$ GPa) is required by the Fourier-domain Green's function used in Relax and may cause biases in estimated coseismic stress changes and in the response of postseismic deformation mechanisms, particularly in the mantle (HEARN and BÜRGMANN 2005). Consequently, the forward models presented in the following sections are best viewed as simple end-member models.

7. Forward Modeling of Stress-Driven Afterslip

We use Relax to model time-dependent afterslip on the modeled downward extensions of coseismic rupture planes F2 and F3, and on the previously described vertical plane extending northwest into the Yuha Desert. Afterslip in Relax is driven by coseismic shear stress transfer and governed by a constitutive rate-dependent friction law,

$$v = 2v_0 \exp \frac{-\mu_0}{(a - b)} \sinh \frac{\tau}{(a - b)\sigma} \quad (2)$$

where v is the slip rate on the segment, v_0 is a reference velocity, μ_0 is the friction at the reference velocity, a and b are frictional parameters, τ is the shear stress change on the fault, and σ is the normal stress on the fault, assumed constant in time (BARBOT *et al.* 2009). This is a regularized, steady-state version of the laboratory-derived rate-and-state friction law (e.g., MARONE 1998) that has been shown to be appropriate to model afterslip in a number of settings (e.g., MARONE *et al.* 1991; HEARN *et al.* 2002; MIYAZAKI *et al.* 2004; PERFETTINI and AVOUAC 2004; BARBOT *et al.* 2012). The two factors controlling the behavior of afterslip in this formulation are $2v_0 \exp \frac{-\mu_0}{(a - b)}$, which collectively is a constant with units of velocity, and $(a - b)\sigma$, which also controls

the total magnitude of afterslip. We explore a range of values for both factors. Appropriate values for $(a - b)\sigma$ estimated from previous studies of afterslip on continental faults are typically on the order of 1 MPa (e.g., PERFETTINI and AVOUAC 2004, 2007).

We model afterslip in nine different geometries: (1) on lower crustal extensions of planes F2 and F3 of the WEI *et al.* (2011) coseismic model (between 15 and 24 km downdip from the top edges of those planes) with the same dips as on the coseismic rupture; (2) on lower crustal extensions of F2 and F3 with dips 15° shallower than on the coseismic rupture; (3) on lower crustal extensions of F2 and F3 with vertical dips; (4) on extensions of F2 and F3 down to the lithosphere–asthenosphere boundary (between 15 and 48 km downdip from the top edges of those planes), with the same dips as on the coseismic rupture; (5) on the segment extending into the Yuha Desert, with vertical dip and extending down to 12 km depth; (6) on the Yuha segment extending down to 24 km depth; on the Yuha segment extending down to 48 km depth; (7) on both the lower crustal extensions of F2 and F3, with the same dips as the coseismic rupture, and the Yuha segment extending down to 12 km depth; (8) on the same extensions of F2 and F3 plus the Yuha segment extending down to 24 km depth; and (9) on the extensions of F2 and F3 down to the lithosphere–asthenosphere boundary plus the Yuha segment extending down to 48 km depth. The coseismic shear stress change that drives the afterslip is infinite at the edges of the coseismic slip patches, so for computational stability, we add 3 km of spacing between the bottom of coseismic slip (at ~ 12 km depth) and the top of the downward extensions of F2 and F3 (at ~ 15 km depth), and 6 km of spacing between the northwest end of F2 and the segment extending into the Yuha Desert (Fig. 6). The rake of the afterslip is unconstrained. Models that simulate afterslip on the coseismic rupture itself produce little afterslip there because the coseismic shear stress change for right-lateral slip is strongly negative on most of the rupture (due to the coseismic stress drop), and so we cannot estimate how afterslip on the coseismic rupture could have contributed to the postseismic transient in a time-dependent sense. This does not preclude the possibility that afterslip did occur on the coseismic

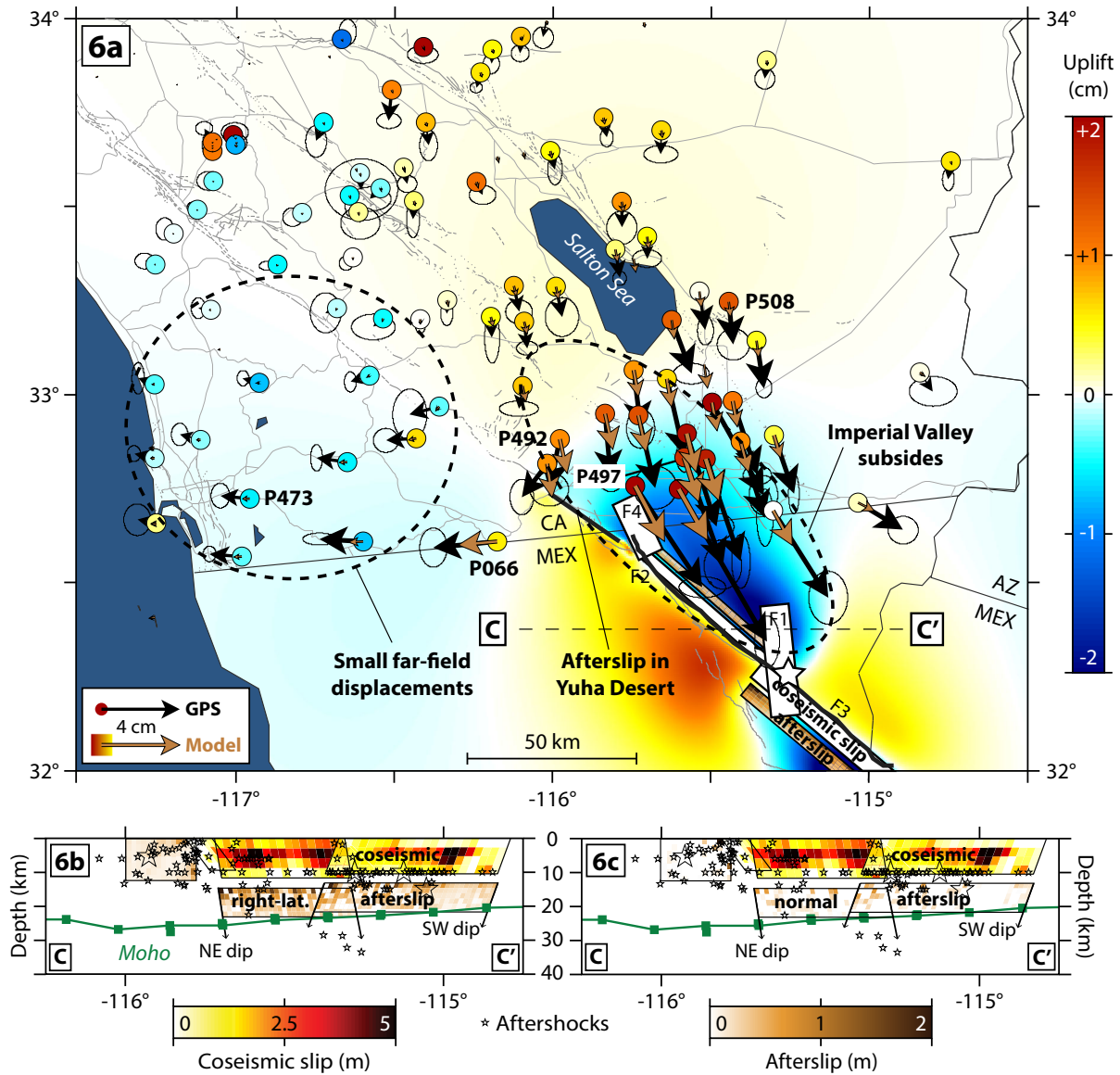


Figure 6

Forward modeling of stress-driven afterslip on modeled downward extensions of coseismic slip planes F2 and F3 in the Wei *et al.* (2011) coseismic model into the lower crust. The afterslip is allowed between 15 and 24 km downdip from the top edges of these planes, is driven by coseismic shear stress changes and is governed by a rate-strengthening friction law with $(a - b)\sigma = 1$ MPa. Slip is also allowed on a 30-km long segment extending northwest into the Yuha Desert to fit the aftershocks and surface creep there to first order; this segment has a vertical dip and extends to 12 km depth. **a** This afterslip model produces horizontal surface displacements with the correct azimuth but the wrong pattern of uplift and subsidence. **b, c** Slip decreases away from the coseismic rupture, as expected for a stress-driven mechanism

rupture, however, especially if the real slip distribution was more spatially heterogeneous at fine scales than that of Wei *et al.* (2011).

We find that afterslip on the downward extensions of the rupture and in the Yuha Desert produces subsidence in the Imperial Valley rather than the uplift

observed here (Figs. 6, 28), consistent with the observation that a northwest-striking dislocation below seismogenic depth should produce subsidence to the north (Fig. 21c). We find that afterslip on the lower crustal extensions of planes F2 and F3, and in the Yuha Desert extending down to 12 or 24 km

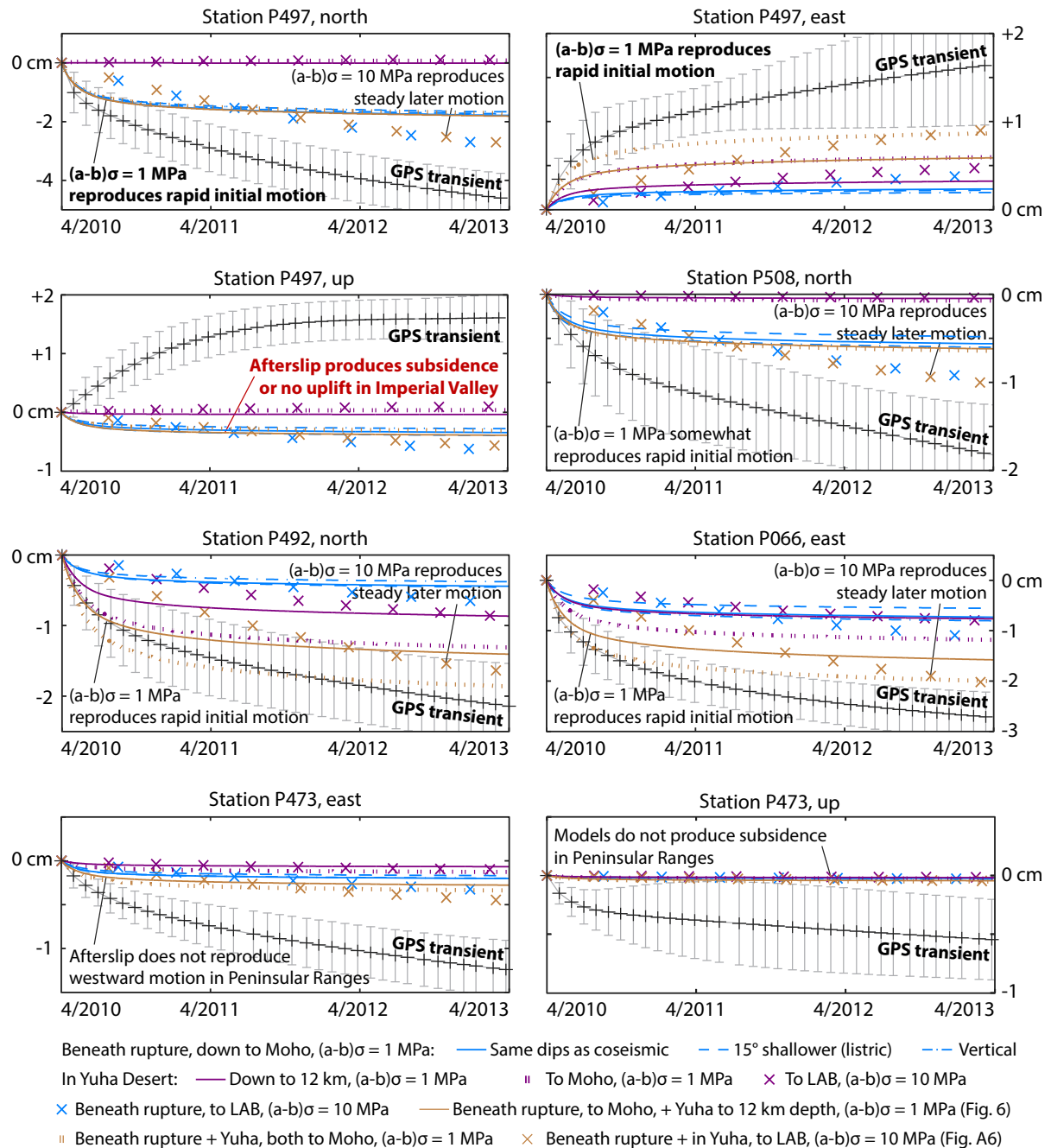


Figure 7

Comparison of extracted GPS time series at several GPS stations (locations indicated in Fig. 6) with synthetic time series of surface displacement generated by modeled stress-driven afterslip. While lower crustal afterslip with $(a - b)\sigma = 1 \text{ MPa}$ reproduces the rapid early displacement rates in the Imperial Valley, afterslip extending into the mantle lithosphere with $(a - b)\sigma = 10 \text{ MPa}$ reproduces the sustained later displacement rates in the Imperial Valley

depth, with $(a - b)\sigma = 1 \text{ MPa}$, can reproduce the rapidly decaying early horizontal motions in the Imperial Valley well (Fig. 7), and afterslip on planes

extending down to the lithosphere–asthenosphere boundary with $(a - b)\sigma = 10 \text{ MPa}$ can reproduce the later, sustained horizontal motions in the Imperial

Valley. (Although 10 MPa is an order of magnitude higher than values for $(a - b)\sigma$ estimated from previous studies of afterslip in the crust, it may not be inappropriate for slip in the mantle as σ should increase with depth.) Models featuring slip into the mantle with $(a - b)\sigma = 1$ MPa overshoot the rapid initial displacements in the Imperial Valley, and models featuring slip only into the crust with $(a - b)\sigma = 10$ MPa do not produce significant surface displacements. Although we are not able to simulate afterslip with spatially variable frictional parameters, the success of each model at reproducing a key aspect of displacement time series in the Imperial Valley suggests that much of the horizontal motion there could be fit to an afterslip mechanism that incorporates elements of both these models. However, none of the afterslip models reproduce the large displacements or the subsidence in the Peninsular Ranges (Fig. 7). Cumulative 3-year displacements on the afterslip planes in these forward models are considerably less than the displacements that were assigned to fit the far-field displacements in the kinematic inversions that allowed for slip into the mantle. Geometrically, the $(a - b)\sigma = 10$ MPa model is equivalent to the kinematic inversion that allows slip on downward extensions of planes F2 and F3 into the mantle but not on the coseismic rupture (Fig. 27). Whereas that inversion assigned well over a meter of right-lateral and normal slip on most of the slip planes, including beneath the Moho, the total stress-driven afterslip in the $(a - b)\sigma = 10$ MPa model after 3-years is well under a meter across most of the planes (Fig. 28). Even the kinematic inversion that allowed for slip on the coseismic rupture as well as into the mantle (Fig. 5) still assigned close to a meter of right-lateral and normal slip on much of the planes to fit the far-field displacements. Thus, it can be said that at least in this configuration, featuring a rate-strengthening friction law with $(a - b)\sigma = 10$ MPa, the cumulative afterslip at depth predicted after 3 years is not enough to fit 3-year surface displacements in the far-field. This motivates us to assess whether distributed viscoelastic relaxation could also have been responsible for some components of the observed postseismic transient.

8. Forward Modeling of Viscoelastic Relaxation in the Lower Crust

The very high heat flow in the Salton Trough (LACHENBRUCH *et al.* 1985) suggests that the lower crust there may have reduced viscosity (WILLIAMS *et al.* 2012) and thus might have produced a visible signal of viscoelastic relaxation following the El Mayor-Cucapah earthquake. However, the Moho shallows to ~ 22 km in the Salton Trough from > 30 km in much of southernmost California (TAPE *et al.* 2012) (Fig. 8), and so one might alternatively suppose that the lower crust of the surrounding regions, with a greater thickness of potentially low-viscosity material, might have featured more heavily in postseismic deformation than the Salton Trough lower crust. To test these hypotheses, we use Relax to model viscoelastic relaxation in eight different postulated geometries of ductile zones in the lower crust: (1) a layered ductile zone between a depth of 10 km and the TAPE *et al.* (2012) Moho surface at all locations; (2) a similar layered zone between a depth of 15 km and the Moho surface; (3) a layered ductile zone 0–12.5 km above the Moho surface at all locations; (4) a similar layered zone 0–7.5 km above the Moho surface; (5) a localized ductile zone from 10–22.5 km depth in the “geothermal” geometry, a narrow zone in the Salton Trough beneath locations of high heat flow and geothermal activity; (6) a localized zone from 15–22.5 km depth in the “geothermal” geometry; (7) a localized ductile zone at 10–22.5 km depth in the “ST” geometry, above the zone of shallow (LEKIC *et al.* 2011) lithosphere–asthenosphere boundary in the Salton Trough; and (8) a localized zone from 15–22.5 km depth in the “ST” geometry (Fig. 8). Viscoelastic relaxation in Relax is driven by coseismic changes in deviatoric stress and can be governed either by a Newtonian rheology,

$$\dot{\gamma} = \frac{\tau}{\eta} \quad (3)$$

where $\dot{\gamma}$ is the viscous strain rate, τ is the deviatoric stress and η is the Newtonian viscosity, or by a rheology featuring a stress-dependent viscosity

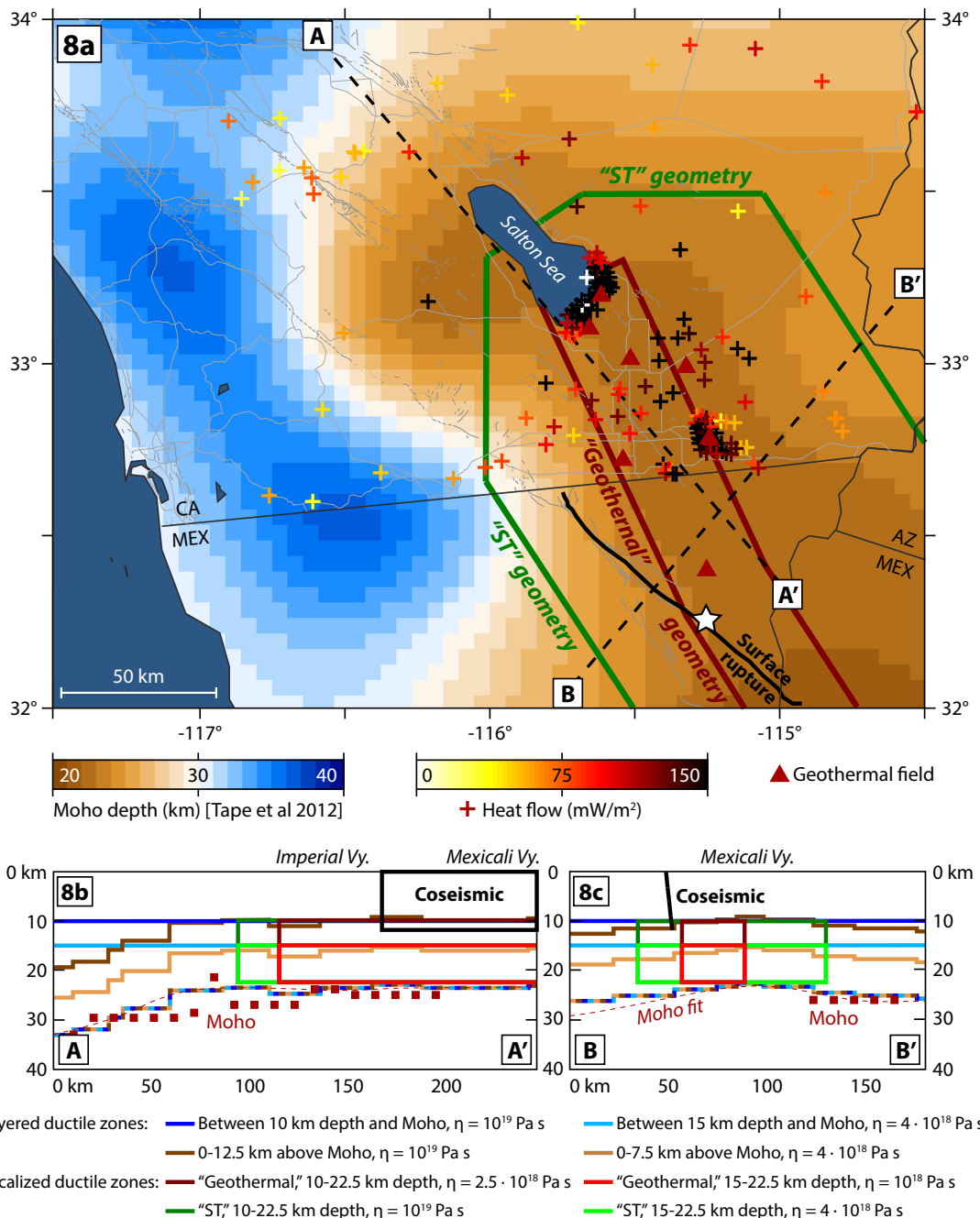


Figure 8

We simulate viscoelastic relaxation in eight postulated geometries for low-viscosity zones in the lower crust: (1) a ductile zone between 10 km depth and the TAPE *et al.* (2012) Moho surface at all locations; (2) the same geometry but with a top depth of 15 km; (3) a ductile zone 0–12.5 km above the Moho surface at all locations; (4) a ductile zone 0–7.5 km above the Moho surface; (5) a ductile zone from 10 to 22.5 km depth in the “geothermal” geometry, a narrow zone in the Salton Trough beneath locations of high heat flow and geothermal activity; (6) from 15 to 22.5 km depth in the “geothermal” geometry; (7) a ductile zone at 10–22.5 km depth in the “ST” geometry, above the zone of shallow (LEKIC *et al.* 2011) lithosphere–asthenosphere boundary in the Salton Trough; and (8) from 15 to 22.5 km depth in the “ST” geometry. **a** Mapview of Moho depth, heat flow, geothermal areas, and geometries of modeled localized ductile zones. **b, c** Cross sections of Moho depth and geometries of modeled ductile zones

$$\dot{\gamma} = C \left(\frac{\tau}{\mu} \right)^n \quad (4)$$

where C is a coefficient dependent on factors such as grain size, water content, and temperature (e.g., FREED and BÜRGMANN 2004), μ is the shear modulus and n is an exponent. Within each of the geometries, we model three alternative rheologies: (1) a Newtonian rheology, (2) a stress-dependent viscosity with $n = 2.5$, consistent to first order with laboratory observations of dry quartzite and some of wet quartzite, and (3) a stress-dependent viscosity with $n = 4$, consistent with other laboratory studies of wet quartzite (FREED and BÜRGMANN 2004).

The mainshock likely imparted vertical compression at 22.5 km depth (Moho depth) beneath the northern Imperial Valley and beneath and just northeast of the rupture (Fig. 29). Viscoelastic relaxation of this compression should have featured material flowing out of those regions at depth, causing subsidence at the surface, and indeed we find that simulated viscoelastic relaxation in the lower crust produces subsidence in the Imperial Valley regardless of the geometry or rheology prescribed (Figs. 30, 31, 33), meaning that it alone cannot explain the observed postseismic transient. However, we find that Newtonian viscoelastic relaxation in the modeled lower crustal ductile zones with $\eta = 10^{18} - 10^{19}$ Pa s can reproduce the sustained horizontal velocities that followed the rapidly decaying early motions at GPS stations in the Imperial Valley (Fig. 9). In particular, Newtonian viscoelastic relaxation in the “geothermal” geometry with $\eta = 2.5 \times 10^{18}$ Pa s (with a top depth of 10 km) or 10^{18} Pa s (with a top depth of 15 km) matches the azimuth of the sustained horizontal velocities in the Imperial Valley well, producing the highest ratio of eastward to southward velocities at station P497 of all geometries modeled (Fig. 9). A stress-dependent viscosity with $n = 2.5$ concentrates higher rates of displacement closer to the mainshock in both space and time and produces surface displacements that can match both the rapidly decaying early motion and the later sustained velocities at some stations, again with relaxation in the “geothermal” geometries producing the most eastwardly motions at station P497 (Fig. 32). A stress-dependent viscosity with $n = 4$ concentrates high displacement

rates even closer to the mainshock in time and cannot fit the sustained horizontal displacements well, but can fit some of the rapid initial velocities (Fig. 34).

9. Forward Modeling of Viscoelastic Relaxation in the Mantle Lithosphere

The models of viscoelastic relaxation in the lower crust assume a relatively weak crust over a relatively strong mantle. Alternative conceptions of lithospheric strength feature a relatively strong crust over a relatively weak mantle lithosphere, or both a weak lower crust and weak mantle lithosphere (e.g., BÜRGMANN and DRESEN 2008), and so it is useful to assess whether viscoelastic relaxation in the mantle lithosphere could also explain aspects of the observed postseismic deformation. We simulate viscoelastic relaxation with Newtonian and stress-dependent rheologies in three postulated geometries for low-viscosity zones in the mantle lithosphere (Fig. 10): the “ML” geometry, a ductile zone between the (TAPE *et al.* 2012) Moho surface and a simple geometric approximation to the (LEKIC *et al.* 2011) lithosphere–asthenosphere boundary at all locations; the “ST” geometry, a ductile zone at 22.5–45 km depth above the zone of shallow (LEKIC *et al.* 2011) lithosphere–asthenosphere boundary in the Salton Trough, and the “geothermal” geometry, a ductile zone at 22.5–45 km depth in a narrow zone in the Salton Trough beneath locations of high heat flow and geothermal activity. Within these three geometries, we model two alternate rheologies: a linear Newtonian rheology and a stress-dependent viscosity with $n = 3.5$, consistent with laboratory observations of dislocation creep in dry and wet olivine and thought to be perhaps the dominant rheology in the upper mantle (KIRBY 1983; HIRTH and KOHLSTEDT 2003; FREED and BÜRGMANN 2004; KARATO 2008).

We find that Newtonian viscoelastic relaxation with $\eta \sim 2 \times 10^{18}$ Pa s in the “ML” and “ST” geometries produces steady horizontal motion that resembles that observed in the Imperial Valley to first order (Fig. 11). However, this mechanism cannot reproduce the magnitude of the steady horizontal velocities at station P497 (at least with the geometries

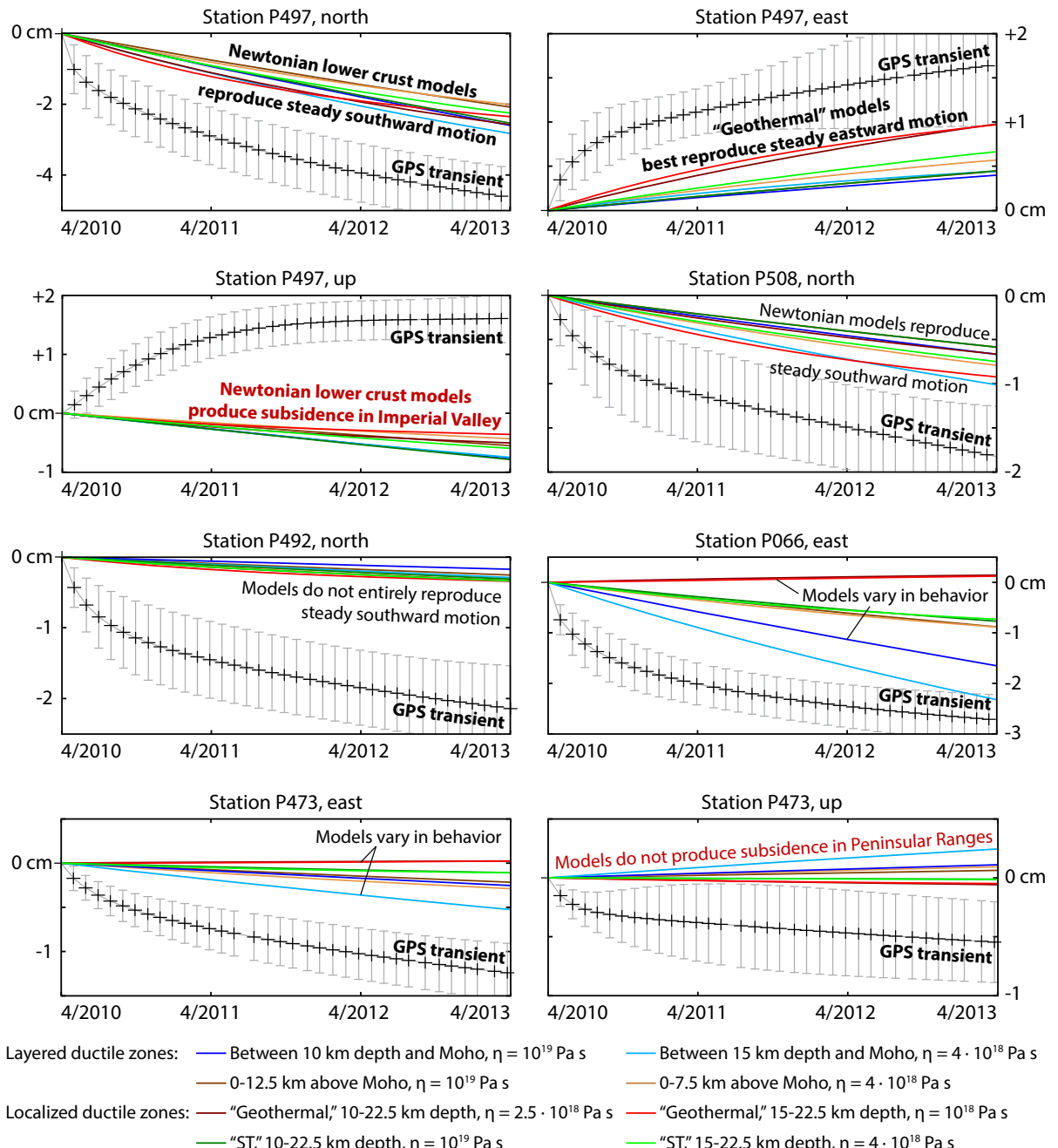


Figure 9
Comparison of extracted GPS time series at several GPS stations (locations indicated in Figs. 4a and 30) with synthetic time series of surface displacement generated by Newtonian viscoelastic relaxation in the modeled lower crustal ductile zones

used here) without overshooting the inferred velocities at station P508, further from the rupture on the northeast side of the Imperial Valley (Fig. 11), whereas Newtonian viscoelastic relaxation in the

lower crust had no problem reproducing the steady velocities at both stations (Fig. 9). This can be thought of as reflecting the fact that the mantle lithosphere is deeper than the lower crust and relaxation

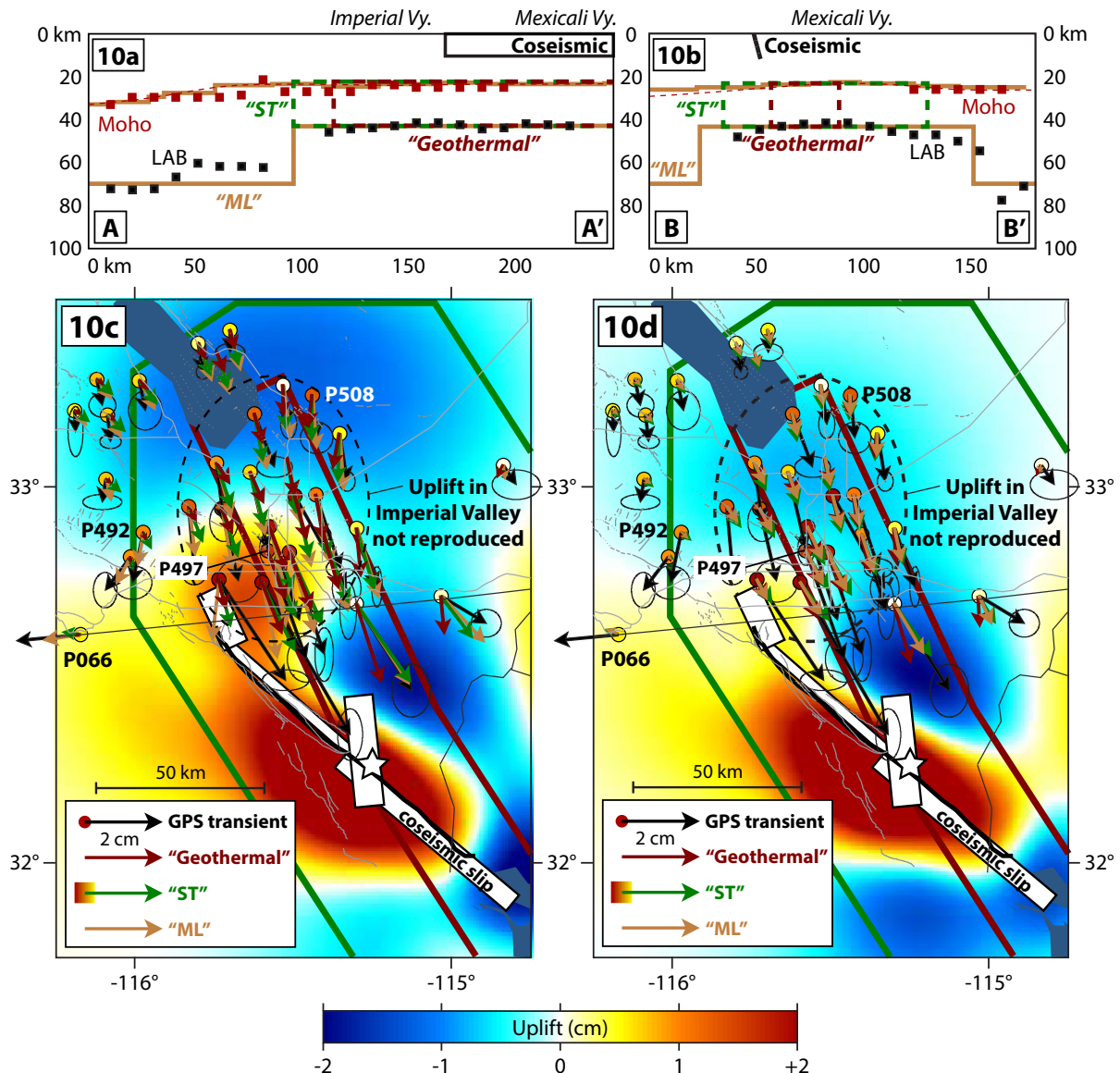


Figure 10

We simulate viscoelastic relaxation in three postulated geometries for low-viscosity zones in the mantle lithosphere: the “ML” geometry, a ductile zone between the (TAPE *et al.* 2012) Moho surface and the geometrically approximated (LEKIC *et al.* 2011) lithosphere–asthenosphere boundary at all locations; the “ST” geometry, from 22.5 to 45 km depth above the zone of shallow (LEKIC *et al.* 2011) lithosphere–asthenosphere boundary in the Salton Trough, and the “geothermal” geometry, from 22.5 to 45 km depth in a narrow zone in the Salton Trough beneath locations of high heat flow and geothermal activity. **a, b** Cross sections of the modeled geometries; the locations of the cross sections are depicted in Fig. 8. **c** Synthetic three-year surface displacements at GPS stations generated by Newtonian viscoelastic relaxation in the modeled lower crustal ductile zones. The vertical displacement field is from the “ST” model. **d** Synthetic 3-year surface displacements at GPS stations generated by viscoelastic relaxation with a stress-dependent viscosity ($n = 3.5$) in the modeled mantle lithosphere geometries. The vertical displacement field is from the “ST” model

there will produce a broader deformation pattern at the surface, with slower velocities closer to the rupture and faster velocities farther from the rupture. Viscoelastic relaxation with a stress-dependent

viscosity ($n = 3.5$) in the mantle lithosphere can to some extent reproduce the rapidly decaying early horizontals in the Imperial Valley (Fig. 11). Though Newtonian viscoelastic relaxation in the mantle

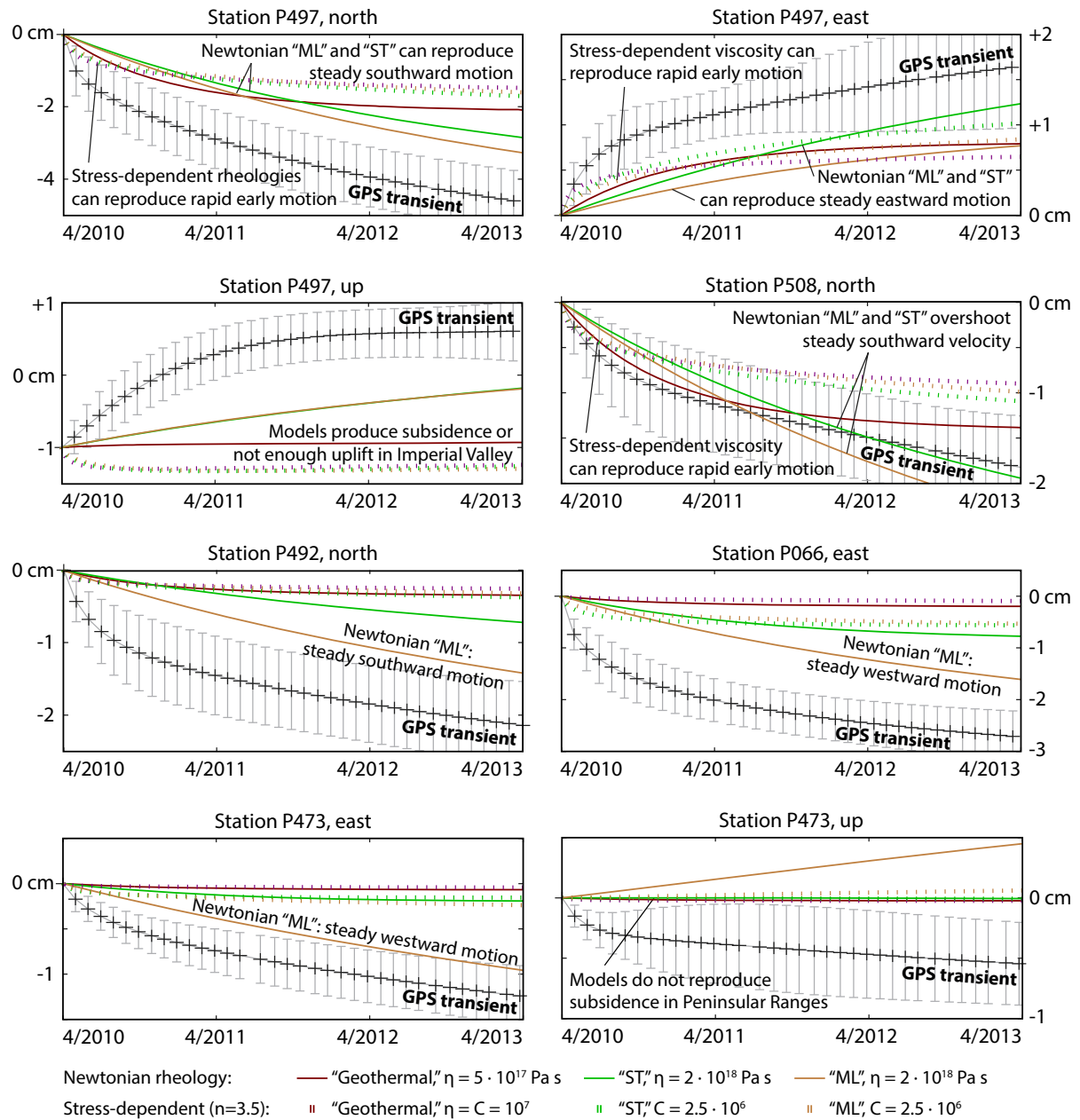


Figure 11

Comparison of extracted GPS time series at several GPS stations (locations indicated in Fig. 10 and other map view figures) with synthetic time series of surface displacement generated by viscoelastic relaxation with Newtonian and stress-dependent ($n = 3.5$) rheologies in the modeled ductile zones in the mantle lithosphere

lithosphere produces some uplift around the rupture and just northeast of it (Fig. 10), probably reflecting the coseismic vertical extension at 22.5–45 km depth there (Fig. 29), neither a Newtonian nor a stress-dependent viscosity can reproduce the systematic uplift observed at GPS stations in the Imperial Valley

(Fig. 10). This suggests that viscoelastic relaxation can produce uplift there only if it includes relaxation below the LEKIC *et al.* (2011) lithosphere–asthenosphere boundary. Newtonian viscoelastic relaxation in the "ML" geometry can reproduce the steady westward velocities at station in P473 in the

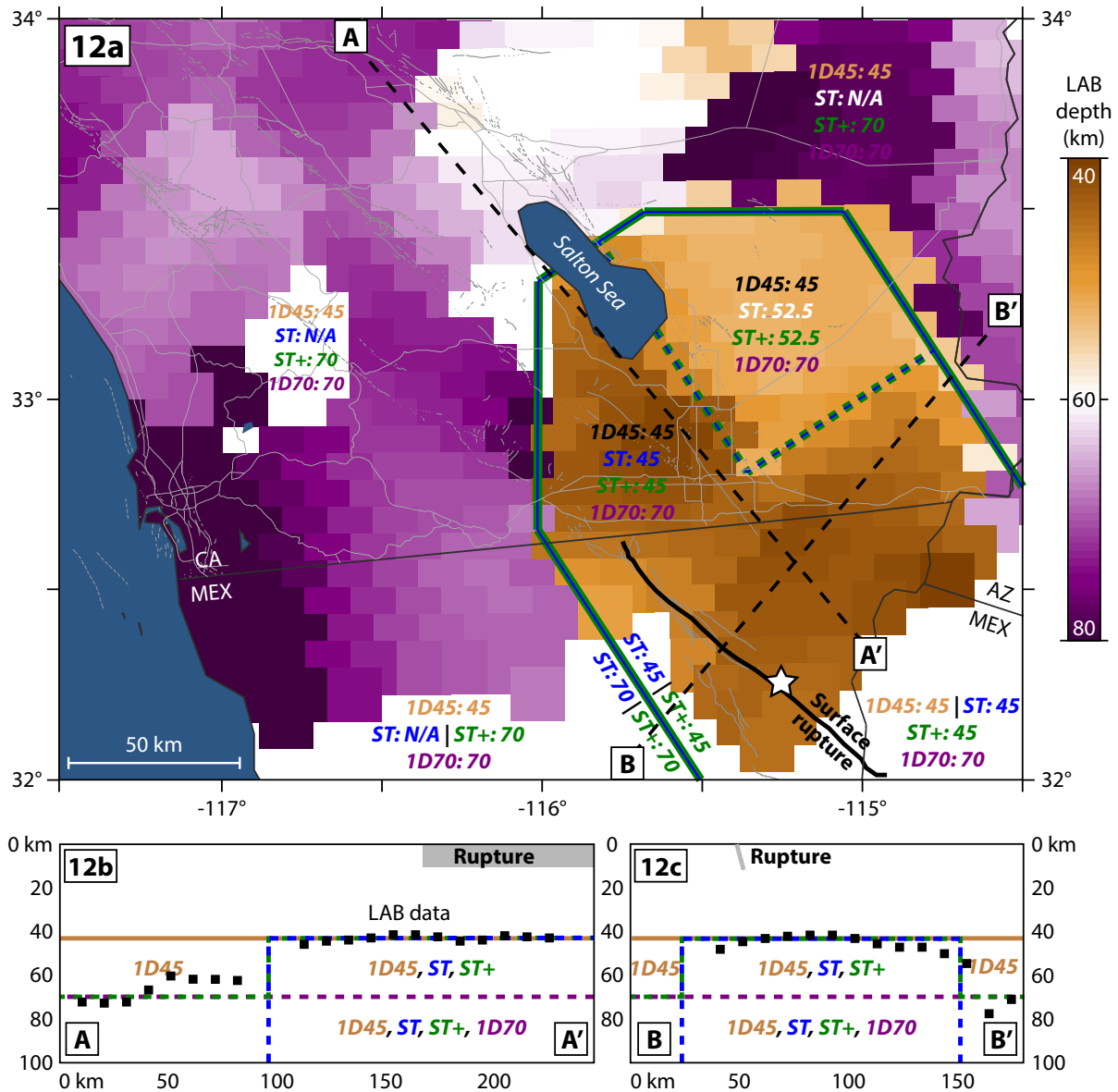
Peninsular Ranges but produces steady uplift there; none of the models can reproduce the subsidence observed there (Fig. 11).

10. Forward Modeling of Viscoelastic Relaxation in the Asthenosphere

LEKIC *et al.* (2011) imaged the lithosphere–asthenosphere boundary in southern California with receiver functions and found that the asthenosphere shallowed to a depth of ~ 45 km in the Salton Trough, compared to regional average of ~ 70 km. Thus, viscoelastic relaxation in the asthenosphere could have contributed to the observed postseismic transient, and if so, the lateral heterogeneity in its geometry imaged by seismic methods might also be visible using this method, which samples deformation over timescales many orders of magnitude longer. We model viscoelastic relaxation in four postulated geometries for the effective ductile asthenosphere: model “1D45,” in which viscoelastic relaxation is allowed between 45 km depth and the base of the elastic halfspace (~ 300 km depth); model “1D70,” a 1D model allowing relaxation below 70 km depth; model “ST+,” a 3D geometry approximating that of the LEKIC *et al.* (2011) lithosphere–asthenosphere boundary; and model “ST,” a 3D geometry that follows the LEKIC *et al.* (2011) lithosphere–asthenosphere boundary within the Salton Trough and disallows viscoelastic relaxation outside of it (Fig. 12). Within these four geometries, we model two alternate rheologies: a linear Newtonian rheology and a stress-dependent viscosity with $n = 3.5$.

The mainshock imparted vertical extension at 70 km depth beneath the Imperial Valley and beneath the central part of the rupture (Fig. 35). Viscoelastic relaxation should feature asthenospheric material rising from beneath the extended zones, causing recompression of material at the top of the asthenosphere and uplift at the surface. We find that Newtonian viscoelastic relaxation in the 1D45, ST+, and 1D70 models, the three geometries that allow for viscoelastic relaxation outside of the Salton Trough, can qualitatively reproduce the uplift in the

Imperial Valley and the subsidence and sustained westward velocities in the Peninsular Ranges (Fig. 13). Tradeoffs between Newtonian viscosity and geometry make identification of a best-fitting geometry difficult; for example, the sustained westward velocities at stations P066 and P473 can be qualitatively reproduced by Newtonian viscoelastic relaxation with $\eta \sim 1 - 2 \times 10^{18}$ Pa s in the 1D45 geometry, with $\eta \sim 5 \times 10^{17} - 10^{18}$ Pa s in the ST+ geometry, or with $\eta \sim 5 \times 10^{17}$ Pa s in the 1D70 geometry (Fig. 14). Newtonian viscoelastic relaxation in the ST geometry, confined to the Salton Trough, requires viscosities well below $\eta \sim 5 \times 10^{17}$ Pa s (the minimum tested) to fit the horizontal velocities in the Peninsular Ranges and does not reproduce the subsidence observed there. Cross sections of cumulative inelastic (viscous) strain after 3 years of viscoelastic relaxation (Fig. 36) show that although the major viscoelastic relaxation occurs close to the mainshock, some relaxation does occur outside of the Salton Trough in the 1D45, ST+, and 1D70 geometries, and the failure of the ST geometry to reproduce the far-field horizontals or verticals suggests that this relaxation outside the Salton Trough is important. Beyond this, however, the tradeoffs between viscosity and geometry suggest that surface displacements are relatively insensitive to the geometry of the modeled asthenosphere. Models featuring a stress-dependent viscosity with $n = 3.5$ concentrate the viscoelastic relaxation closer to the rupture and reproduce neither the far-field displacements nor the full distribution of vertical displacements (Figs. 37, 38). Neither a Newtonian nor a stress-dependent viscosity can reproduce the observed horizontal displacements in the Imperial Valley; the process is relatively deep and its surface displacements are broad, featuring small displacements close to the rupture and larger displacements far from the rupture. Nonetheless, Newtonian viscoelastic relaxation in the asthenosphere appears to be best candidate mechanism of those modeled to reproduce the subsidence, steady westward velocities and large cumulative displacements in the Peninsular Ranges, suggesting that this mechanism may well have played a role in postseismic deformation.



We simulate viscoelastic relaxation in four alternate postulated geometries for the asthenosphere: model 1D45 (gold), a 1D model in which viscoelastic relaxation is allowed below 45 km depth; model 1D70 (purple), in which viscoelastic relaxation is allowed below 70 km depth; model ST+ (green), in which the top of the viscoelastic zone approximates the geometry of the regional lithosphere–asthenosphere boundary inferred by LEKIC *et al.* (2011), and model ST (blue or white), which approximates the LEKIC *et al.* (2011) lithosphere–asthenosphere boundary in the Salton Trough and forbids viscoelastic relaxation outside of it. **a** Mapview of LEKIC *et al.* (2011) lithosphere–asthenosphere boundary depth and geometries of modeled ductile zones. Sets of numbers prefaced by model names are the top depths of each model at the specified locations. **b, c** Cross sections of LEKIC *et al.* (2011) lithosphere–asthenosphere boundary depth and geometries of modeled ductile zones

11. Multiple-Mechanism Models

No single deformation mechanism (as modeled here) reproduces the entire transient of postseismic displacement observed in GPS time series, suggesting

that the observed transient resulted from multiple processes acting in concert. Here we present two endmember models of multiple mechanisms acting in concert that offer good fits to the observed transient. These models operate on the assumption that each of

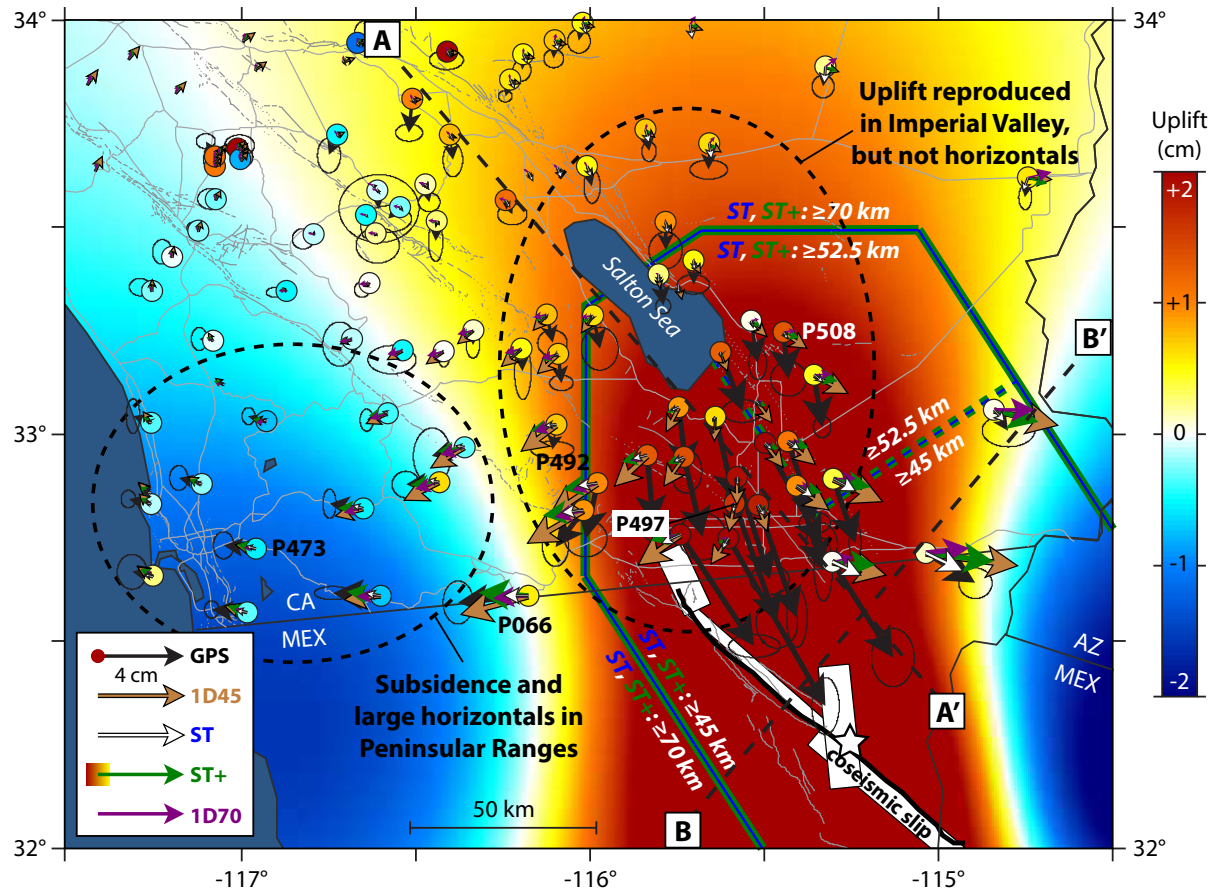


Figure 13

Three-year cumulative surface displacements produced by Newtonian viscoelastic relaxation ($\eta \sim 5 \times 10^{17} \text{ Pa s}$) in the four geometries for the asthenosphere. Viscoelastic relaxation in the asthenosphere reproduces the uplift observed in the Imperial Valley and the subsidence and westward displacements in the Peninsular Ranges

the four key aspects of postseismic deformation—uplift in the Imperial Valley, large westward displacements in the Peninsular Ranges, the rapid initial offset in near-field time series, and the sustained displacement signal that followed it—was essentially produced by a single deformation mechanism. As shown previously, the uplift in the Imperial Valley and the subsidence and relatively large westward displacements in the Peninsular Ranges can be reproduced by Newtonian viscoelastic relaxation in the asthenosphere; the sustained horizontal motions in the Imperial Valley can be reproduced by Newtonian viscoelastic relaxation in the lower crust and/or mantle lithosphere (and in particular, Newtonian viscoelastic relaxation in the localized “geothermal” lower crustal ductile zone fits the azimuth of the

sustained velocity at station P497 without overshooting the velocity at station P508); and the rapidly decaying early horizontal motions in the Imperial Valley and Peninsular Ranges can be reproduced by afterslip on the downward extensions of the rupture and in the Yuha Desert with $(a - b)\sigma \sim 1 \text{ MPa}$ or by viscoelastic relaxation with a stress-dependent viscosity in the lower crust and/or mantle. The two multiple-mechanism models presented here differ only in the mechanism they use to reproduce the rapidly decaying early motion. The first coupled model reproduces this signal with afterslip on downward extensions of coseismic rupture planes F2 and F3 extending down to the Moho and on a segment extending northwest into the Yuha Desert that extends down to 12 km depth [the approximate

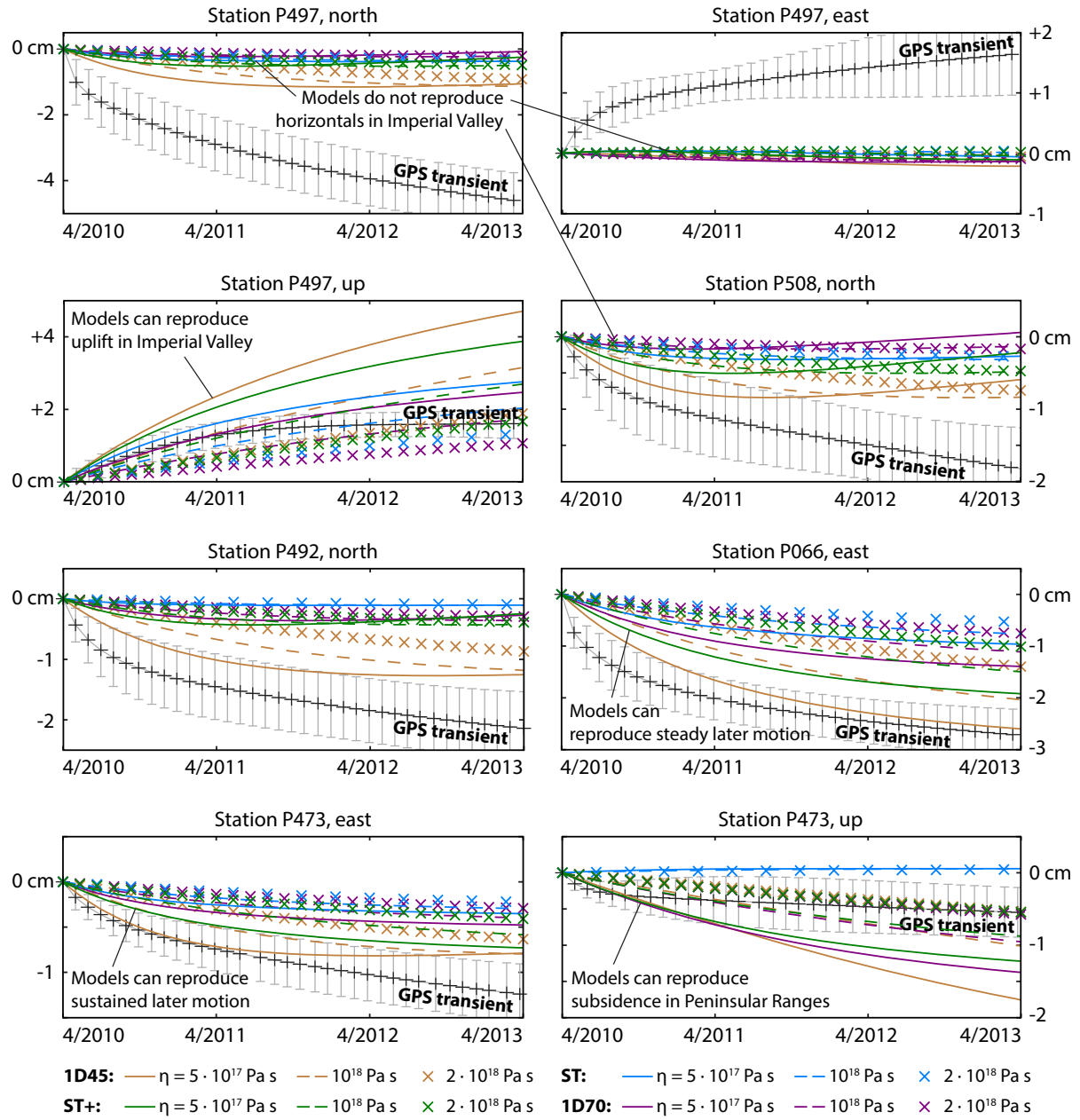


Figure 14

Comparison of extracted GPS time series at several GPS stations (locations indicated in Fig. 13) with synthetic time series of surface displacement generated by Newtonian viscoelastic relaxation in the modeled geometries for the asthenosphere. Viscoelastic relaxation in the “1D45”, “ST+”, and “1D70” geometries can qualitatively reproduce the uplift at station P497, the sustained westward velocities observed at stations P066 and P473, and the subsidence observed at station P473.

maximum depth of postseismic seismicity there from KROLL *et al.* (2013)]. This mechanism operates in concert with Newtonian viscoelastic relaxation with $\eta = 3 \times 10^{18}$ Pa s in the “geothermal” lower crustal ductile zone extending from 10 to 22.5 km

depth and Newtonian viscoelastic relaxation with $\eta = 10^{18}$ Pa s in the “ST+” model for the asthenosphere (Fig. 15). As such, this model can be viewed as an exploration of how well the postseismic transient can be fit without stress-dependent rheologies.

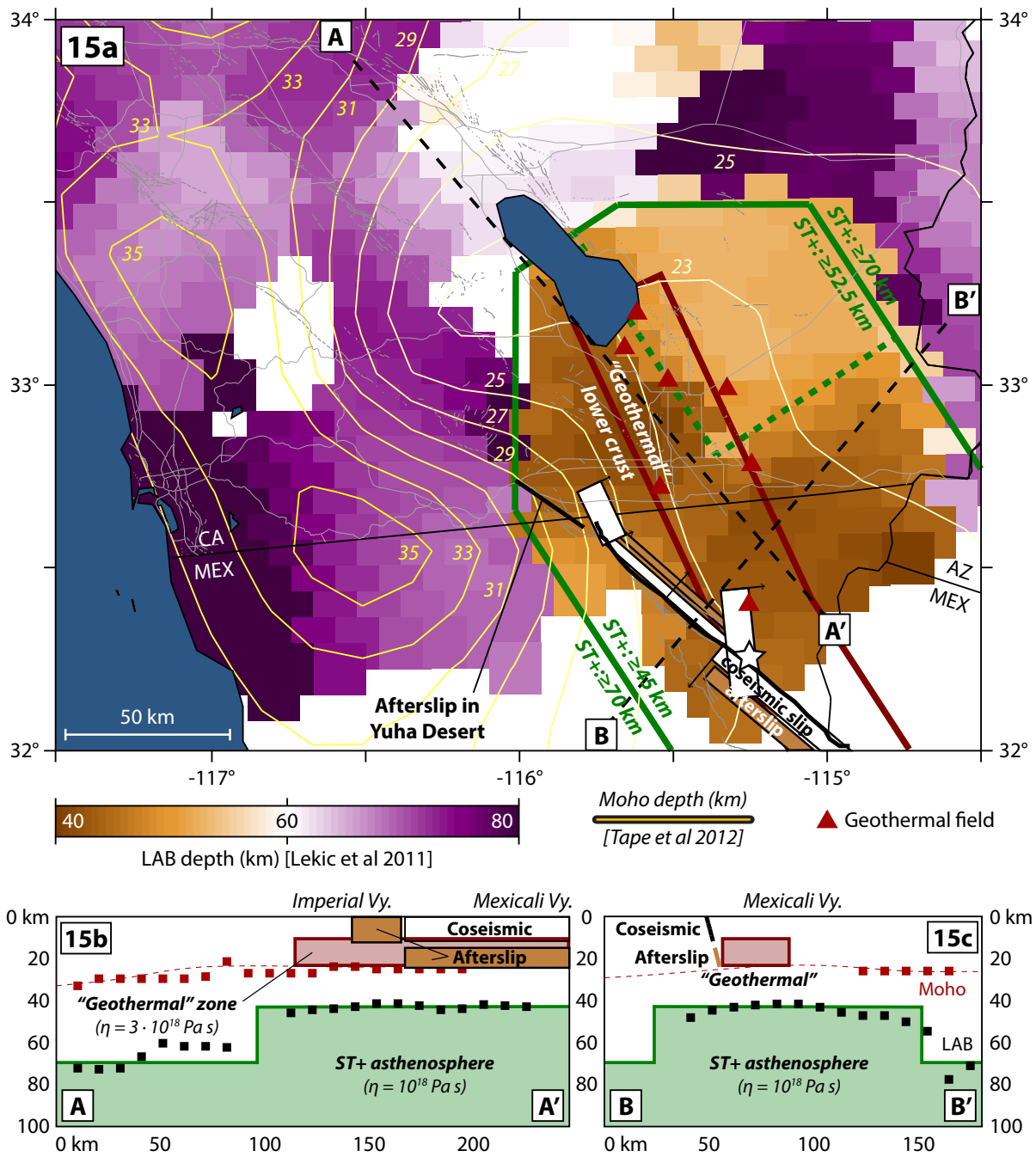


Figure 15

a Setup of the first coupled multiple-mechanism model, featuring afterslip on the downward extensions of the coseismic rupture down to the Moho and on a segment extending northwest into the Yuha Desert that extends down to 12 km depth, Newtonian viscoelastic relaxation from 10 to 22.5 km depth in the “geothermal” lower crust geometry ($\eta = 3 \times 10^{18} \text{ Pa s}$), and Newtonian viscoelastic relaxation in the “ST+” asthenosphere ($\eta = 10^{18} \text{ Pa s}$). **a** Mapview of LEKIC et al. (2011) lithosphere–asthenosphere boundary depth, TAPE et al. (2012) Moho depth, geothermal areas, and model setup. **b, c** Cross sections of LEKIC et al. (2011) lithosphere–asthenosphere boundary depth and Moho depth and model setup

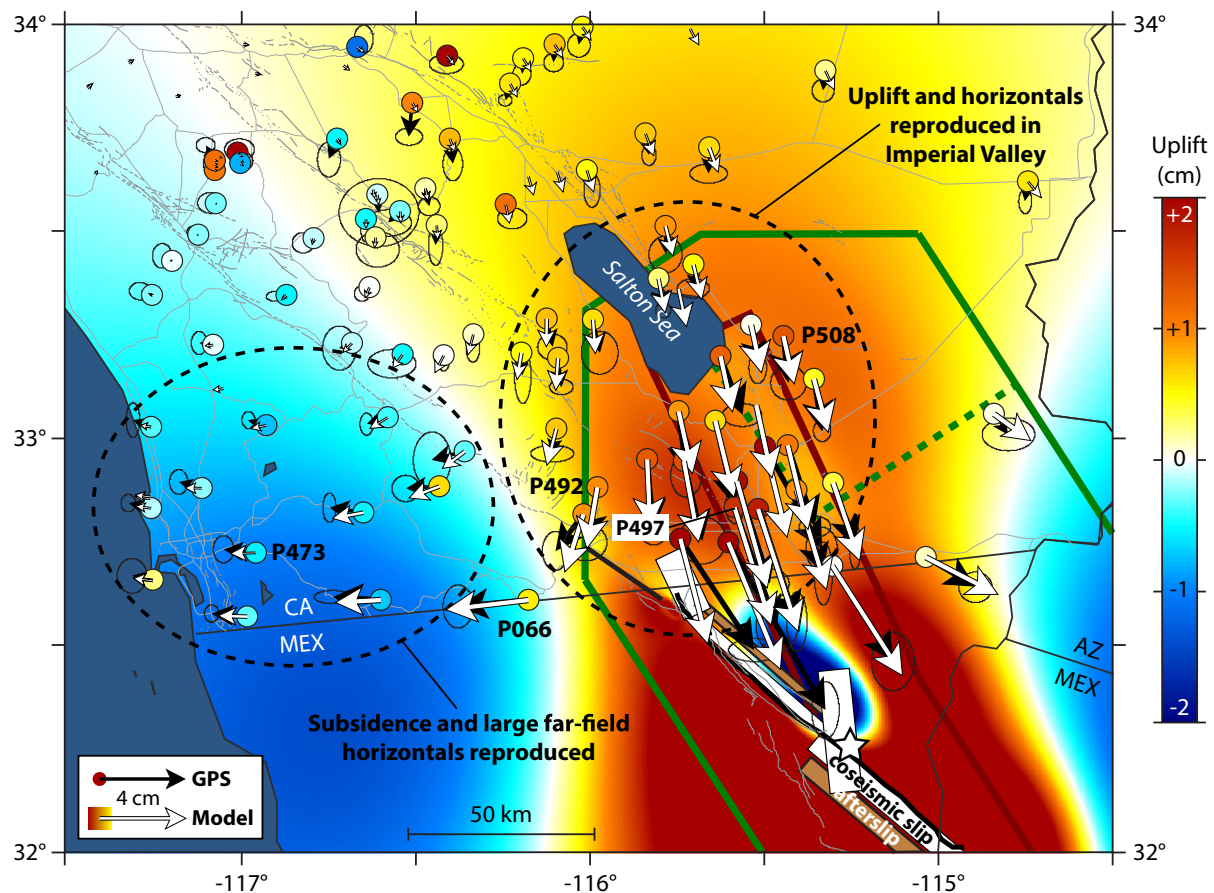


Figure 16

Comparison of three-year cumulative horizontal and vertical postseismic displacements at GPS stations with cumulative synthetic displacements generated by the first coupled model

The model reproduces the horizontal and vertical displacement field well, with variance reductions of 93 % in cumulative 3-year horizontal displacements, 92 % in time-dependent fits to horizontal displacement time series, 49 % in cumulative 3-year vertical displacements, and 48 % in time-dependent fits to vertical displacement time series (Fig. 16). The model reproduces time series of horizontal displacement within uncertainties at stations at a variety of azimuths from the rupture (Fig. 17). Although we cannot estimate variance reductions of cumulative displacements or in time series at stations in Mexico due to the incomplete temporal coverage there, this model also fits the estimated postseismic velocities there well to first order (Fig. 39). To assess the extent to which the different mechanisms in the model feed back on one another in a nonlinear way, we also plot

the summations of displacement time series of the individual mechanisms (Fig. 17). Surface displacement time series from the coupled model are markedly similar to these summed time series, suggesting a low degree of feedback between the mechanisms.

The second multiple-mechanism model retains the Newtonian viscoelastic relaxation with $\eta = 3 \times 10^{18}$ Pa s from 10 to 22.5 km depth in the “geothermal” lower crustal ductile zone and Newtonian viscoelastic relaxation with $\eta = 10^{18}$ Pa s in the “ST+” model for the asthenosphere, but replaces the afterslip in the first model with viscoelastic relaxation with a stress-dependent viscosity ($n = 3.5$) in the mantle lithosphere and “ST+” asthenosphere, with coefficients $C = 10^6$ in the mantle lithosphere and $C = 2 \times 10^8$ in the asthenosphere (Fig. 19). This

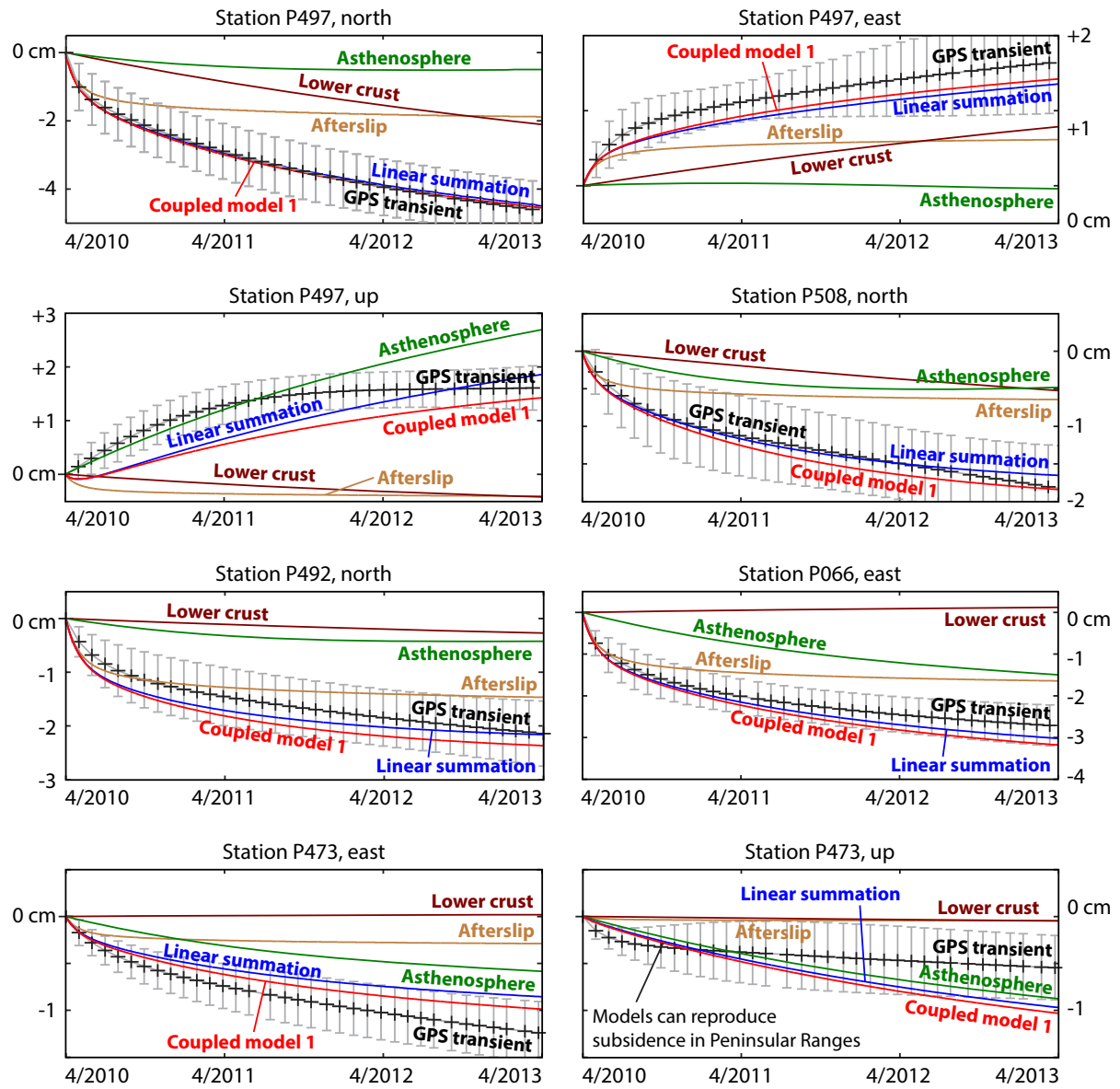


Figure 17

Comparison of extracted GPS time series at several GPS stations (locations indicated in Fig. 16) with synthetic time series of surface displacement generated by the first coupled model

model can be viewed as an exploration of how well the postseismic transient can be fit by a purely viscoelastic model. The model achieves variance reductions of 85 %, both in cumulative 3-year horizontal displacements and in time-dependent fits to horizontal displacement time series, and achieves a better fit to the verticals than the first coupled model, with a variance reduction of 59 % in cumulative 3-year vertical displacements, and 56 % in time-

dependent fits to vertical displacement time series (Fig. 19). The model reproduces the horizontal and vertical transients at station P497 relatively well (Fig. 20); it overshoots southward displacements in the eastern Imperial Valley (Fig. 19), but reproduces the general character of the southward displacement time series at station P508 (Fig. 20). The model undershoots the rapidly decaying early southward velocity at station P492 and the rapidly decaying

early westward velocity at station P066 (Fig. 20), two of the closest stations to the Yuha Desert, suggesting that those displacements were related to a more localized process than viscoelastic relaxation in the upper mantle. In Mexico, the model reproduces the approximate northward postseismic velocity at station PLPX and the eastward velocity at station PLTX less well than the first coupled model (Fig. 40), although high uncertainties in the approximate velocities at those stations make quantitative comparison impractical. As with the first coupled model, time series of surface displacement from the second model differ only subtly from summed time series of surface displacement from the individual participating mechanisms (Fig. 20).

12. Discussion

Many of the endmember mechanisms modeled here can reproduce key aspects of the observed postseismic transient (Table 2), consistent with well-known tradeoffs between mechanisms of postseismic deformation (e.g., Bürgmann and Dresen 2008). Kinematic inversions show that the cumulative 3-year postseismic displacement field in southern California can be well fit to afterslip on the coseismic rupture and possibly the downward extensions of the main rupture planes (Figs. 5, 24), hinting at the possibility that some combination of

shallow and deep afterslip could explain much of the postseismic transient in space and time. Forward modeling shows that stress-driven afterslip in the lower crust and Yuha Desert with $(a - b)\sigma \sim 1$ MPa can reproduce the rapidly decaying early horizontal velocities in the Imperial Valley, and afterslip extending into the upper mantle with $(a - b)\sigma \sim 10$ MPa can reproduce the sustained horizontal velocities following them. Although this combination of lower crustal and upper mantle afterslip does produce subsidence in the Imperial Valley rather than the uplift observed there, afterslip on the coseismic rupture could have produced uplift in the Imperial Valley as the coseismic rupture did (Fig. 2) and as expected for a northwest-striking dislocation that comes to the surface (Fig. 21a). And although these forward afterslip models fail to reproduce the subsidence or large displacements in the Peninsular Ranges due to the lower slip predicted at depth than required in the kinematic inversions, it is possible that afterslip obeying a different constitutive law than simple rate-strengthening friction, or even a different spatial variability of a similar friction law, may be able to produce more slip at depth than modeled here and may be able to fit the far-field displacements more successfully, possibly in conjunction with afterslip on the coseismic rupture. Another possibility is that either of the near-field signals could result from flow in a very weak ductile shear zone in the lithosphere, activated by coseismic slip and/or afterslip above

Table 2

Key aspects of the observed postseismic transient and the modeled deformation mechanisms that can reproduce them

| Key aspect of postseismic transient | Modeled mechanisms that can reproduce aspect |
|--|--|
| Uplift in Imperial Valley and subsidence in Peninsular Ranges | Afterslip on coseismic rupture (kinematic inversion) |
| Relatively large westward displacements in Peninsular Ranges | Newtonian viscoelastic relaxation in asthenosphere |
| Rapidly decaying early horizontal velocities in Imperial Valley | Newtonian viscoelastic relaxation in "ML" mantle lithosphere Newtonian viscoelastic relaxation in asthenosphere Afterslip with $(a - b)\sigma \sim 1$ MPa Viscoelastic relaxation with stress-dependent viscosity ($n = 2.5$) in lower crust Viscoelastic relaxation with stress-dependent viscosity ($n = 4$) in lower crust Viscoelastic relaxation with stress-dependent viscosity ($n = 3.5$) in mantle lithosphere |
| Sustained horizontal velocities in Imperial Valley following rapid early motions | Afterslip with $(a - b)\sigma \sim 10$ MPa Newtonian viscoelastic relaxation in lower crust Viscoelastic relaxation with stress-dependent viscosity ($n = 2.5$) in lower crust (?) Newtonian viscoelastic relaxation in mantle lithosphere |

it (MONTÉSI and HIRTH 2003). Although dynamically activated shear zones may generally be unlikely to produce significant postseismic surface deformation (TAKEUCHI and FIALKO 2013), the high heat flow in the Salton Trough could conceivably result in a very low-viscosity shear zone that does so here. Therefore, it is possible that much of the postseismic transient could be the result of afterslip or localized shear deformation.

Nevertheless, the best candidate mechanism to fit the subsidence and relatively large cumulative westward displacements in the Peninsular Ranges, as well as the uplift in the Imperial Valley, appears to be viscoelastic relaxation in the asthenosphere (Fig. 14). This is consistent with the findings of GONZALEZ-ORTEGA *et al.* (2014), who found that neither afterslip on the coseismic rupture nor poroelastic rebound in the crust could reproduce displacements at GPS stations in southernmost California, even in the first 6 months following the rupture and inferred that viscoelastic relaxation played a role in the postseismic transient (though that study did not consider afterslip below the coseismic rupture). Although we find that a Newtonian rheology in the asthenosphere can reproduce those aspects of the data well, a setting featuring a stress-dependent viscosity in the upper mantle and a background stress state of much greater magnitude than the coseismic stress changes could result in a quasi-linear viscoelastic behavior. Thus, we cannot unequivocally conclude that the asthenosphere beneath the Salton Trough has a dominantly Newtonian rheology—only that a Newtonian-looking response to coseismic stress changes fits these aspects of the postseismic transient well. Newtonian viscoelastic relaxation in the “ST” geometry for the asthenosphere, confining the ductile region to the Salton Trough, requires a viscosity well below 5×10^{17} Pa s to fit the westward velocities in the Peninsular Ranges and may not reproduce the subsidence observed there. Newtonian viscoelastic relaxation in the other three geometries can qualitatively reproduce the sustained westward velocities and subsidence in the Peninsular Ranges and the uplift in the Imperial Valley with viscosities of 5×10^{17} – 2×10^{18} Pa s, with tradeoffs between geometry and Newtonian viscosity (Fig. 14). The actual rheological structure of the upper mantle is undoubtedly more complex than

modeled here, in particular due to the inverse exponential dependence of viscosity on temperature (e.g., KARATO 2008), and thus the asthenosphere models used here are very much first-order approximations. Nevertheless, we can conclude that deep viscoelastic relaxation obeying a Newtonian rheology with an isotropic background stress state can reproduce several key aspects of the postseismic transient.

The inferred Newtonian viscosity of $\sim 10^{18}$ Pa s in the asthenosphere is consistent with a viscosity of 5×10^{17} – 10^{18} Pa s inferred for the upper mantle under the Gulf of California from postseismic relaxation following a $M = 6.9$ earthquake in 2009 (MALSERVISI *et al.* 2012) and with values in the range of 10^{18} Pa s inferred for the upper mantle beneath the Basin and Range, another extensional regime (KAUFMANN and AMELUNG 2000; BILLS *et al.* 2007). LUTTRELL *et al.* (2007) inferred an upper mantle viscosity of $\sim 10^{19}$ Pa s for the Salton Trough region, an order of magnitude higher than our estimates, from periodic surface loading associated with filling of prehistoric Lake Cahuilla. That value was obtained assuming an elastic thickness of 35 km, and Fig. 5a of LUTTRELL *et al.* (2007) suggests that the data could also be fit with a viscosity an order of magnitude lower and an elastic layer 40–50 km thick, closer to the inferred lithospheric thickness in the Salton Sea region (LEKIC *et al.* 2011). At the same time, the viscosity inferred here for the asthenosphere is a factor of 10^3 – 10^4 lower than estimates derived from postglacial rebound studies (e.g., BUROV 2007). Although this may to some extent reflect the extensional environment of the Salton Trough, it echoes longstanding discrepancies between mantle viscosity values inferred in postseismic deformation studies and those implied by longer-timescale processes. More locally, FAY and HUMPHREYS (2005) found that the distribution of slip rates across the San Andreas, San Jacinto and Elsinore faults required a strong lower crust with long-term viscosity of at least 5×10^{19} Pa s. One possibility is that inferred viscosities on the timescale of postseismic deformation could simply reflect the transient behavior of a biviscous or multiviscous upper mantle in which the effective steady-state viscosity could be one or more orders of magnitude higher (e.g., MEADE *et al.* 2013). The higher asthenospheric viscosity inferred

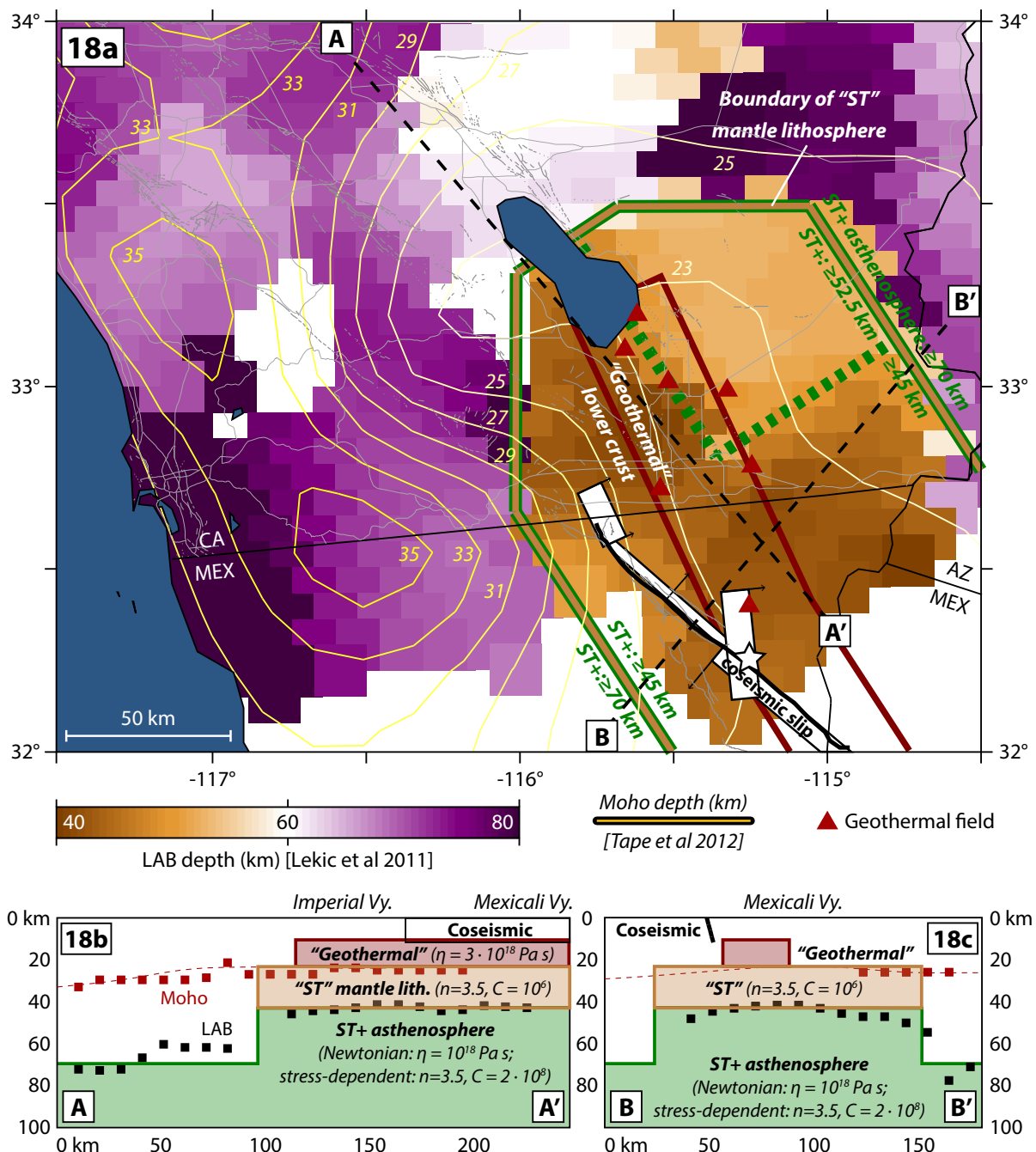


Figure 18

Setup of the second coupled model, featuring Newtonian viscoelastic relaxation in the "geothermal" lower crust geometry ($\eta = 3 \times 10^{18} \text{ Pa s}$), viscoelastic relaxation with a stress-dependent viscosity ($n = 3.5, C = 10^6$) in the "ST" geometry for the mantle lithosphere, and both a Newtonian ($\eta = 10^{18} \text{ Pa s}$) and stress-dependent ($n = 3.5, C = 2 \times 10^8$) rheology in the "ST+" asthenosphere. **a** Mapview of LEKIC et al. (2011) lithosphere–asthenosphere boundary depth, TAPE et al. (2012) Moho depth, geothermal areas, and model setup. **b, c** Cross sections of LEKIC et al. (2011) lithosphere–asthenosphere boundary depth and Moho depth and model setup

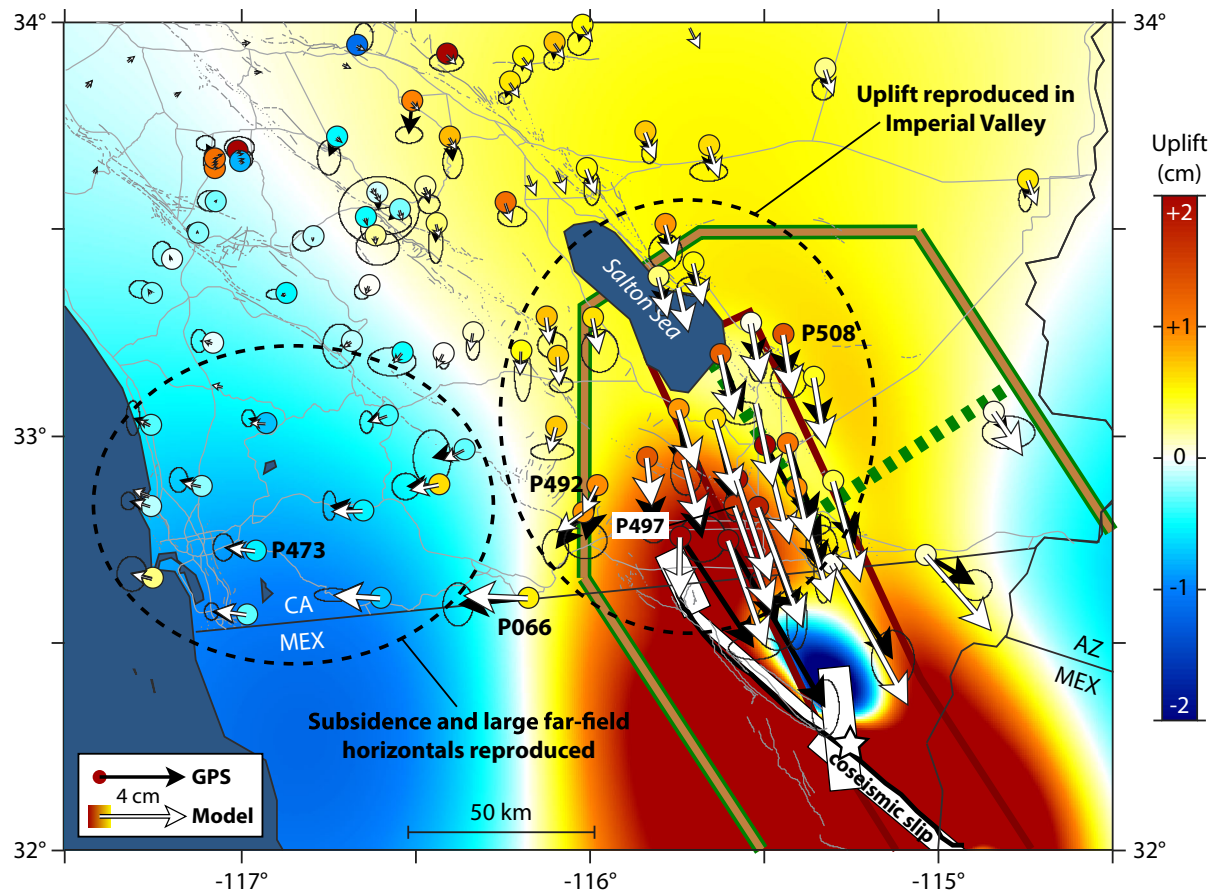


Figure 19

Comparison of three-year cumulative horizontal and vertical postseismic displacements at GPS stations with cumulative synthetic displacements generated by the second coupled model

by LUTTRELL *et al.* (2007), for example, could result from the longer relevant timescale of the process examined in that study.

POLLITZ *et al.* (2012) found that postseismic GPS displacements following the El Mayor-Cucapah earthquake were well fit by a model of viscoelastic relaxation in two regimes: a Newtonian lower crust with viscosity 3.2×10^{19} Pa s and an upper mantle with a biviscous rheology featuring a transient phase of relaxation followed by a steady-state phase. The best-fitting upper mantle featured a laterally heterogeneous rheological structure with transient and steady-state viscosities of 1.2×10^{17} Pa s and 3.2×10^{18} Pa s (respectively) beneath the Salton Trough and transient and steady-state viscosities of 3.4×10^{18} Pa s and 9.2×10^{19} Pa s (respectively) beneath the Peninsular Ranges to the west and the

Southern California River Desert to the east. Despite the different rheologies used here, our second multiple-mechanism model (Figs. 18, 19, 20, 40) is similar in principle to the best-fitting structure of POLLITZ *et al.* (2012), ascribing the rapid early velocities in the Salton Trough to nonlinear viscoelastic relaxation in a laterally heterogeneous upper mantle. Our first multiple-mechanism model (Figs. 15, 16, 17, 39) shows that the rapid early velocities can also be reproduced by afterslip in the crust, with the remaining aspects of the transient reproduced solely by Newtonian viscoelastic relaxation. The upper mantle may be more likely dominated by stress-dependent creep than a Newtonian rheology (e.g., HIRTH and KOHLSTEDT 2003; KARATO 2008), and the success of our first master model in reproducing much of the postseismic transient does not mean that

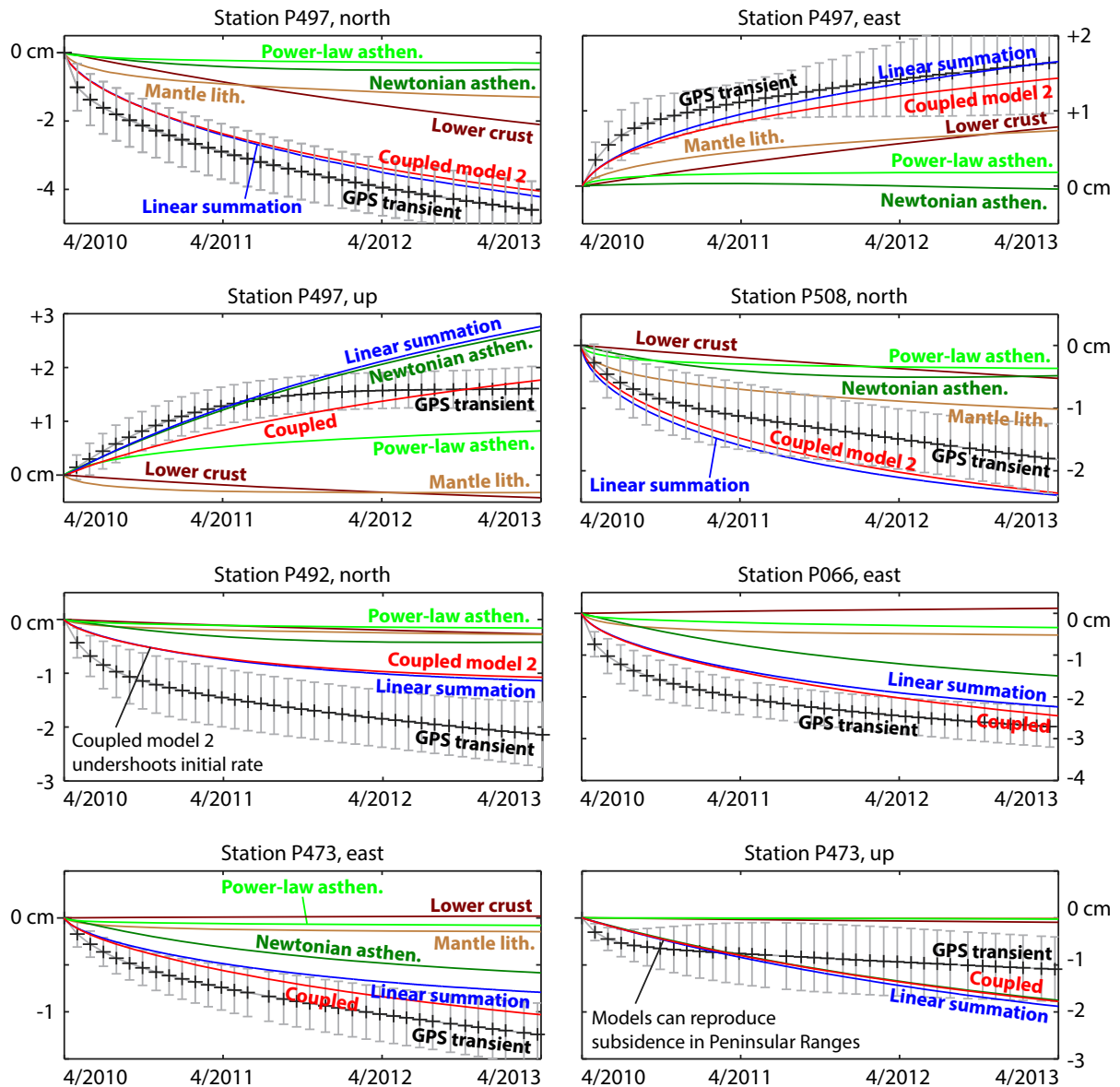


Figure 20

Comparison of extracted GPS time series at several GPS stations (locations indicated in Fig. 19) with synthetic time series of surface displacement generated by the second coupled model

stress-dependent rheologies are negligible in this region: as discussed previously, the deformation we fit to Newtonian viscoelasticity may actually result from relaxation in an upper mantle with a stress-dependent viscosity and a high background deviatoric stress state. Nonetheless, both of our coupled models can be useful in understanding the basic time behaviors of these processes as well as the tradeoffs

between afterslip and viscoelastic relaxation. In general, the high heat flow in the Salton Trough region and the high shear strain rates associated with the Pacific-North American plate boundary mean that the postseismic deformation following the El Mayor-Cucapah earthquake may have featured aspects of both these models and may have been much more complex than either of them.

13. Conclusions

Three-year cumulative postseismic surface displacements following the El Mayor-Cucapah earthquake can be fit intriguingly well by slip on the coseismic rupture and below, and forward models of afterslip in the lower crust and mantle can reproduce multiple key aspects of postseismic displacement time series in the Imperial Valley, making it conceivable that afterslip could possibly explain much of the observed transient in southern California. The key aspects of the transient can also be reproduced by viscoelastic relaxation in the crust and mantle, and in particular, viscoelastic relaxation in the asthenosphere may be the best candidate mechanism to explain the pattern of postseismic uplift and subsidence and relatively large westward displacements

observed far from the rupture in the Peninsular Ranges. We present two endmember models of multiple coupled mechanisms that reproduce much of the postseismic transient in space and time: one combining afterslip and Newtonian viscoelastic relaxation in the lower crust and asthenosphere, and one combining Newtonian and stress-dependent rheologies in the lower crust, mantle lithosphere and asthenosphere. The tradeoffs between these two models are consistent with well-known tradeoffs between afterslip and viscoelastic relaxation.

Appendix

See Figs. 21, 22, 23, 24, 25, 26, 27, 28, 29, 30, 31, 32, 33, 34, 35, 36, 37, 38, 39, 40.

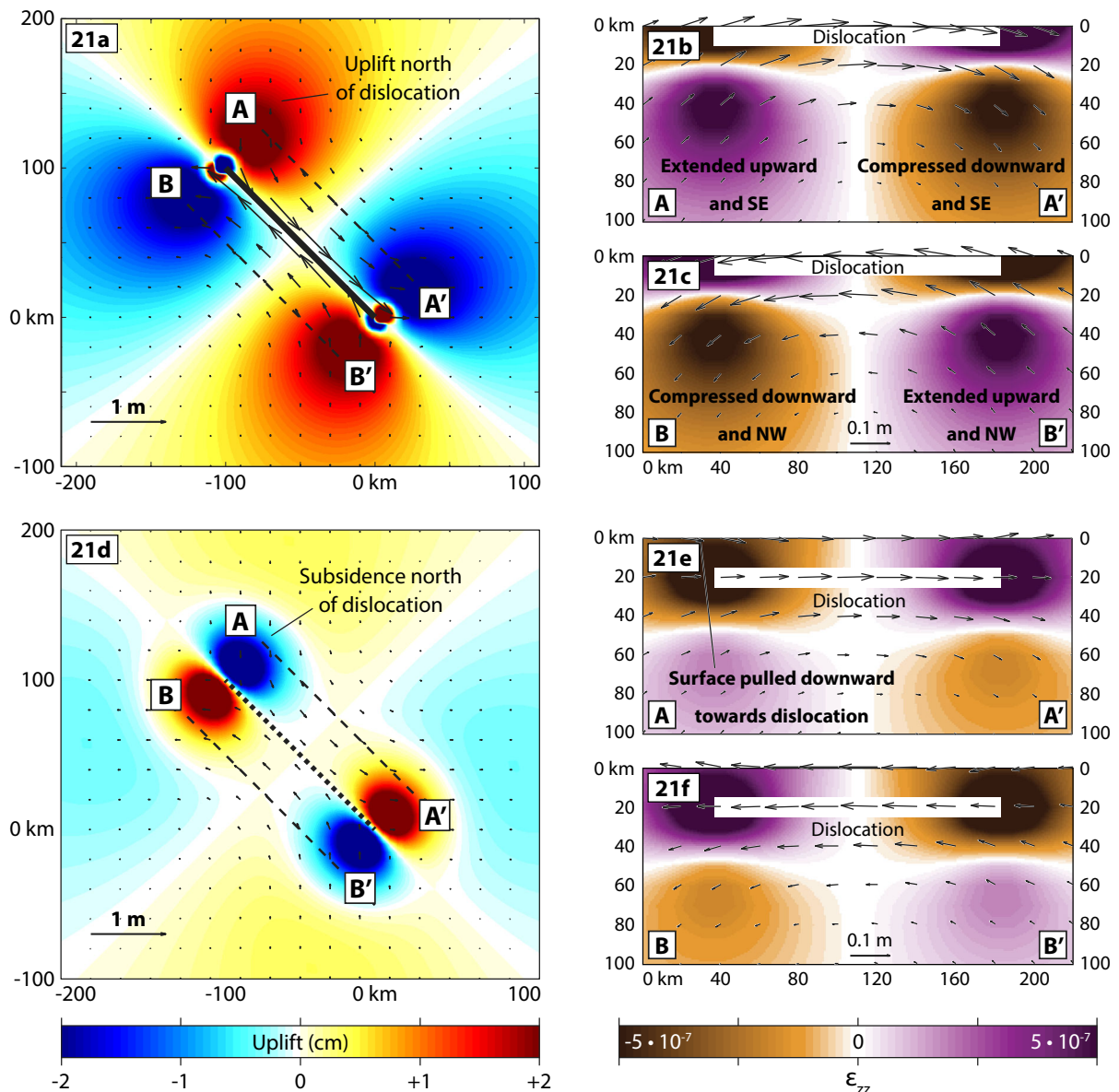


Figure 21

a 2 m of right-lateral slip on a vertical northwest-striking fault from 0 to 10 km depth produces surface uplift in extensional quadrants and subsidence in compressional quadrants. **b, c** Cross sections of coseismic displacement parallel to the dislocation show that material in extensional quadrants is extended upward as well as towards the dislocation, and material in compressional quadrants is compressed downward and away from the dislocation. Material on the *left* half of cross section A-A' corresponds to the Imperial Valley in the El Mayor-Cucapah earthquake. **d** 2 m of right-lateral slip on a vertical northwest-striking fault from 15 to 25 km depth produces near-field subsidence in extensional quadrants and near-field uplift in compressional quadrants. **e, f** Material at the surface just north of the northwest end is pulled downward towards the dislocation

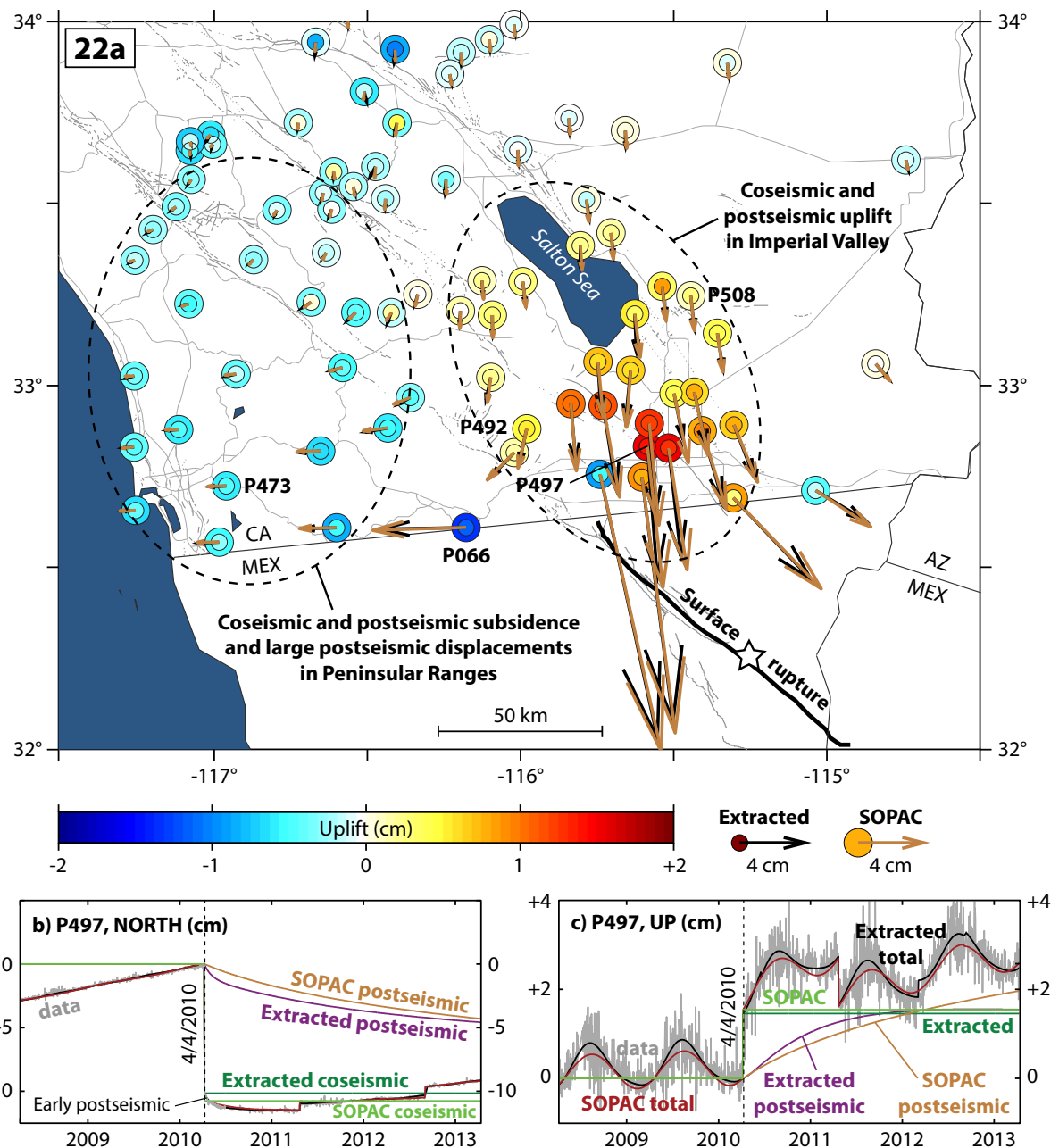


Figure 22

Comparison of extracted coseismic displacements at GPS stations with coseismic displacements estimated by SOPAC. **a** Horizontal and vertical coseismic displacements are generally similar between the two estimates. **b** Time series estimated by SOPAC use only a single decay term and incorrectly ascribe some of the very early horizontal postseismic displacement in the Imperial Valley to coseismic displacement.

c Comparison of vertical displacement time series at station P497 in the Imperial Valley

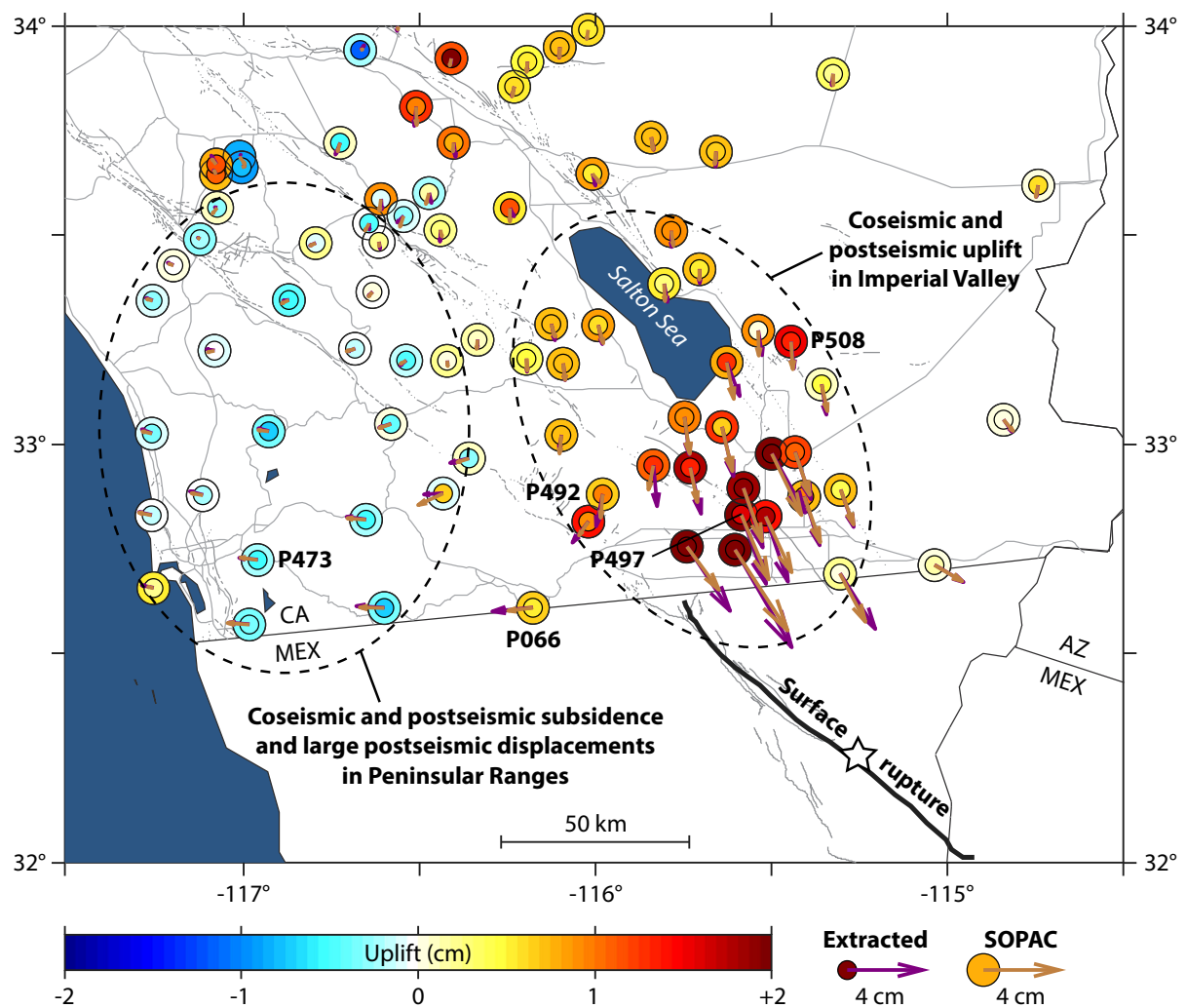


Figure 23

Comparison of cumulative extracted three-year postseismic displacements at GPS stations with cumulative three-year postseismic displacements estimated by SOPAC

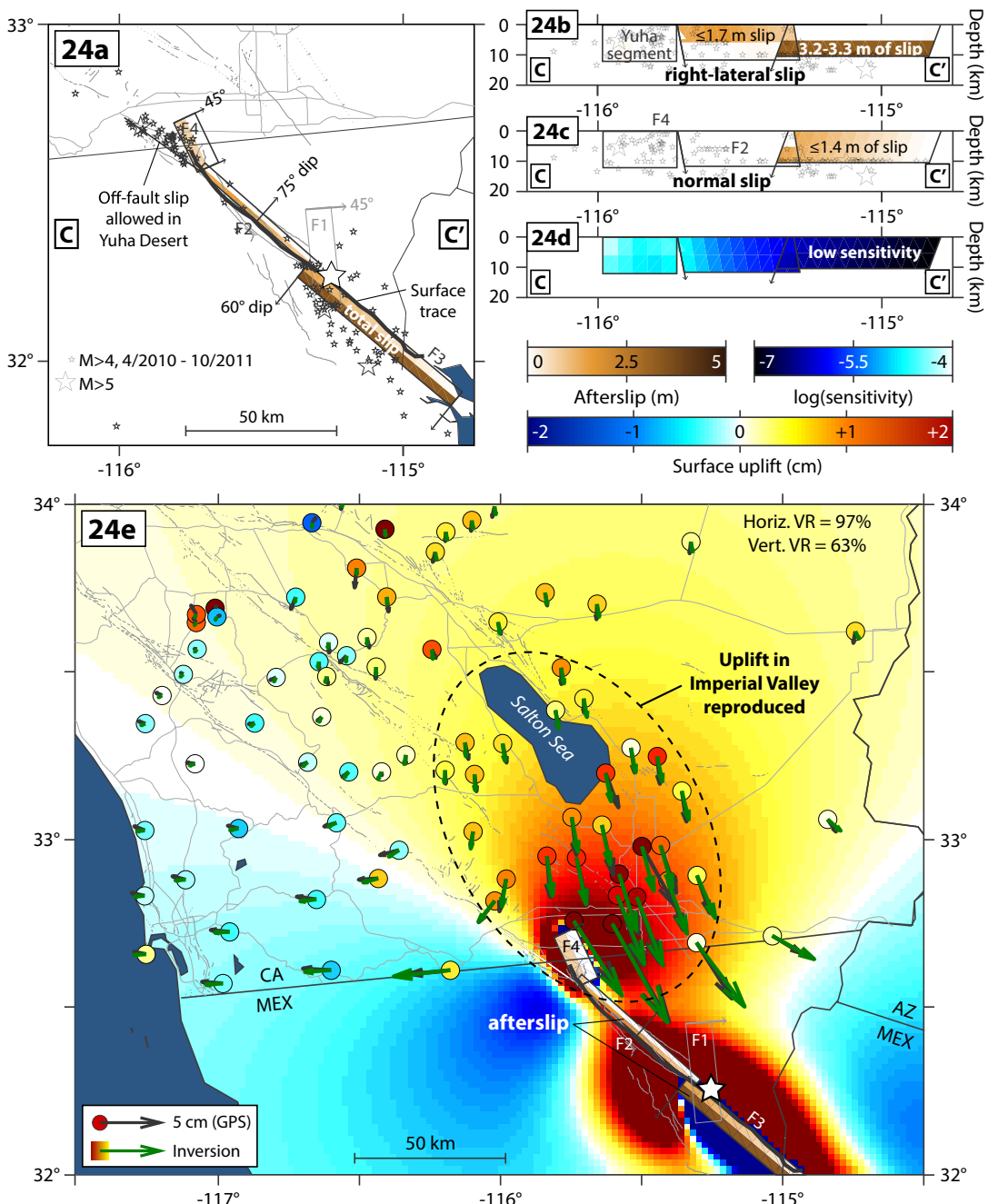


Figure 24

Inversion of 3-year cumulative postseismic GPS displacements for afterslip on the main coseismic rupture planes and in the Yuha Desert.

a Slip is allowed on planes F2, F3, and F4 of the Wei *et al.* (2011) model for the mainshock between 0 and 12 km downdip from their top edges ($\sim 0\text{--}12$ km depth). Slip is also allowed on a 30-km long segment extending northwest into the Yuha Desert to fit the aftershocks and surface creep there to first order; this segment has a vertical dip and extends to 12 km depth.

b-d The inversion assigns up to 1.7 m of right-lateral slip on plane F2 and up to 3.3 m of right-lateral slip and 0–1.4 m of normal slip on plane F3, equivalent in total moment to a $M = 7.2$ earthquake.

e The inversion produces 97 and 63 % variance reductions in horizontal and vertical displacements, respectively.

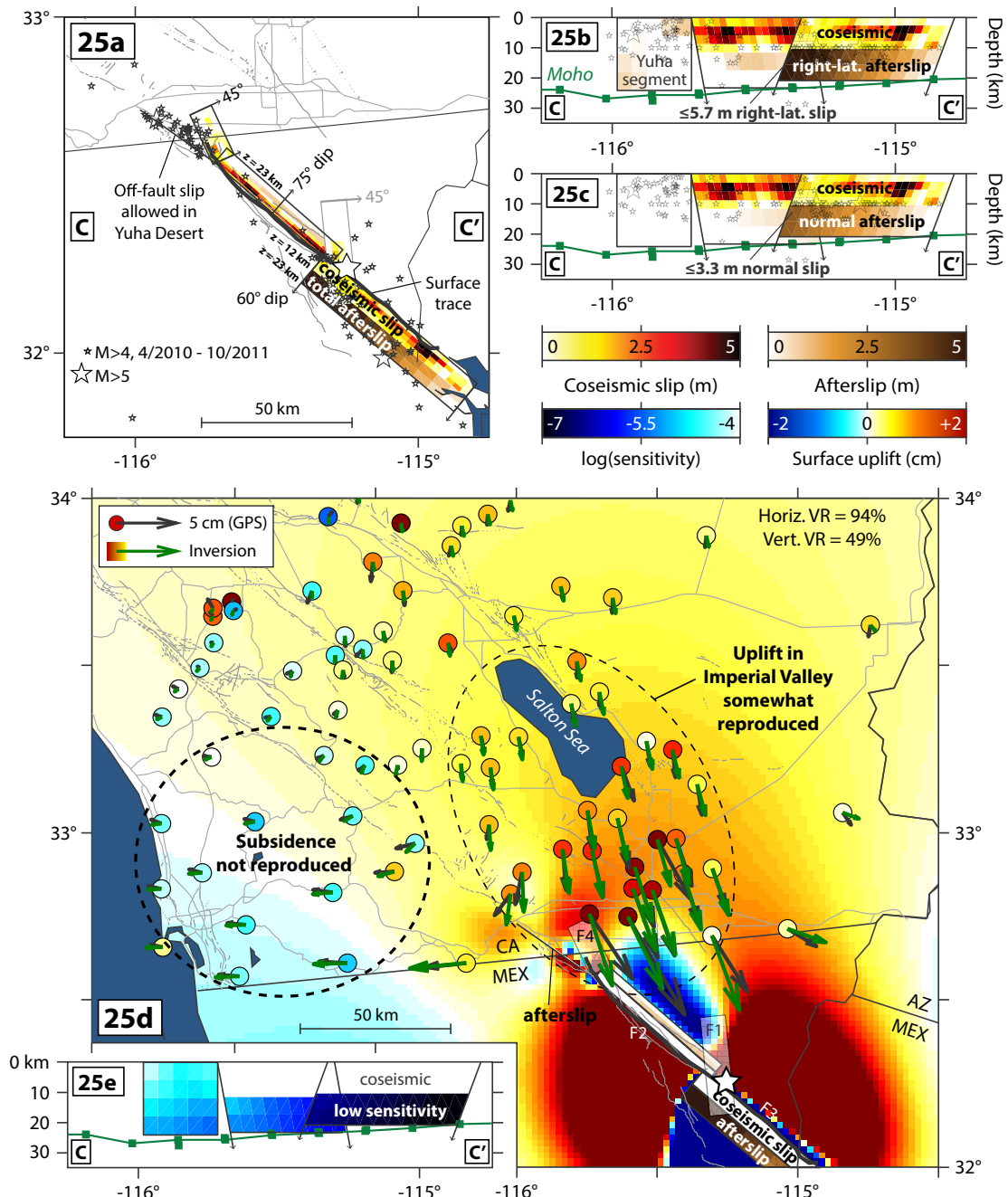


Figure 25

Inversion of 3-year cumulative postseismic GPS displacements for afterslip in the lower crust and Yuha Desert. **a** Slip is allowed on the extensions of slip planes F2 and F3 from the Wei *et al.* (2011) coseismic model into the lower crust, between 12 and 24 km downdip from the top edges of those segments (~ 12 – 24 km depth; 24 km is the approximate Moho depth). Slip is also allowed on a 30-km long segment extending northwest into the Yuha Desert to fit the aftershocks and surface creep there to first order and any possible slip at greater depth; this segment has a vertical dip and extends to 24 km depth. **b, c, e** The inversion assigns up to 5.7 m of right-lateral slip and 3.3 m of normal slip on the lower crustal extension of plane F3, equivalent in total moment to a $M = 7.3$ earthquake. **d** The inversion produces variance reductions of 94 and 49 % in horizontal and vertical displacements, respectively; the observed pattern of uplift and subsidence is visibly less well fit here than in models that allow for slip on the coseismic rupture

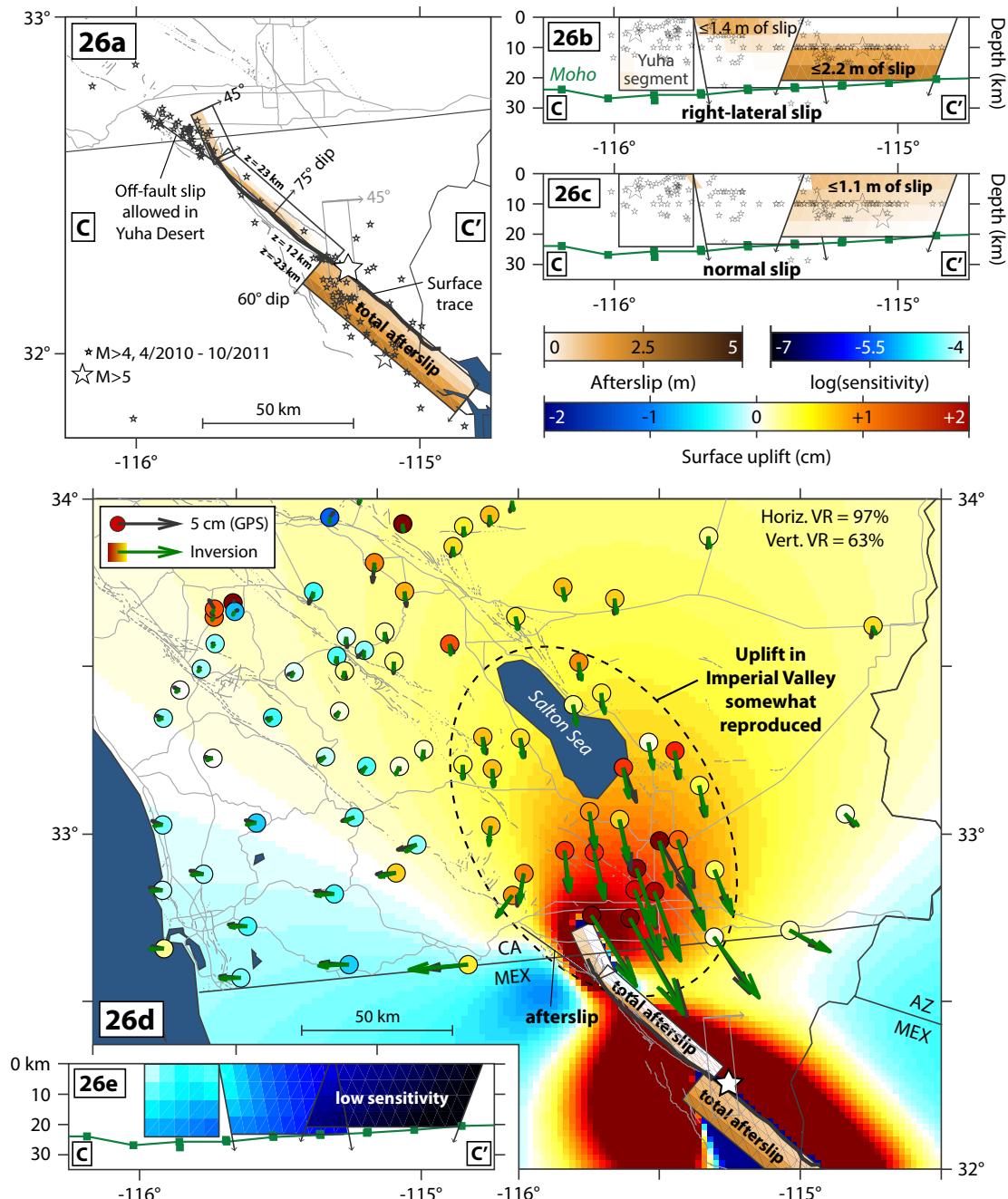


Figure 26

Inversion of 3-year cumulative postseismic GPS displacements for afterslip on the main coseismic rupture planes, on modeled downward extensions of the coseismic rupture planes, and in the Yuha Desert. **a** Slip is allowed on planes F2, F3, and F4 of the Wei *et al.* (2011) model for the mainshock (between 0 and 12 km downdip from their top edges) and on extensions of F2 and F3 into the lower crust (between 12 and 24 km downdip). Slip is also allowed on a 30-km long segment extending northwest into the Yuha Desert to fit the aftershocks and surface creep there to first order and any possible slip at greater depth; this segment has a vertical dip and extends to 24 km depth. **b, c, e** The inversion assigns up to 2.2 m of right-lateral slip and 1.1 m of normal slip on plane F3 and its lower crustal extension, equivalent in total moment to a $M = 7.2$ earthquake. **d** The inversion produces 97 and 63 % variance reductions in horizontal and vertical displacements, respectively

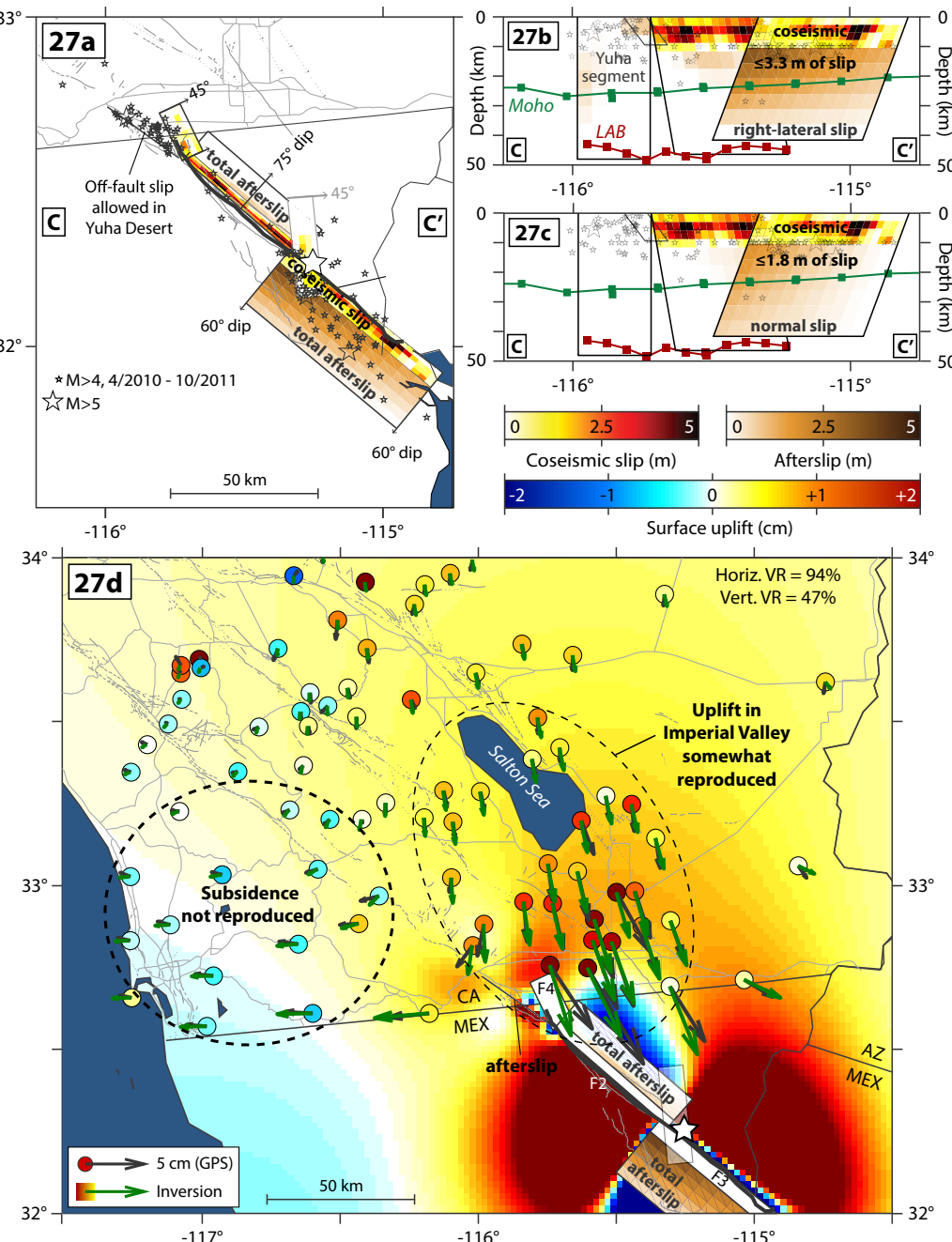


Figure 27
Inversion of 3-year cumulative postseismic GPS displacements for afterslip in the lower crust, mantle lithosphere and Yuha Desert. **a** Slip is allowed on the extensions of slip planes F2 and F3 from the Wei *et al.* (2011) coseismic model into the lower crust and mantle lithosphere, at distances between 12 and 48 km downdip from the top edges of those segments. Slip is also allowed on a 30-km long segment extending northwest into the Yuha Desert to fit the aftershocks and surface creep there to first order and any possible slip at greater depth; this extension has a vertical dip and extends to 48 km depth. **b, c** The inversion assigns up to 3.3 m of right-lateral slip and 1.8 m of normal slip on the deep extension of plane F3, equivalent in total moment to a $M = 7.3$ earthquake. **d** The inversion produces variance reductions of 94 and 47 % in horizontal and vertical displacements, respectively; the distribution of uplift and subsidence is visibly less well fit here than in models that allow for slip on the coseismic rupture

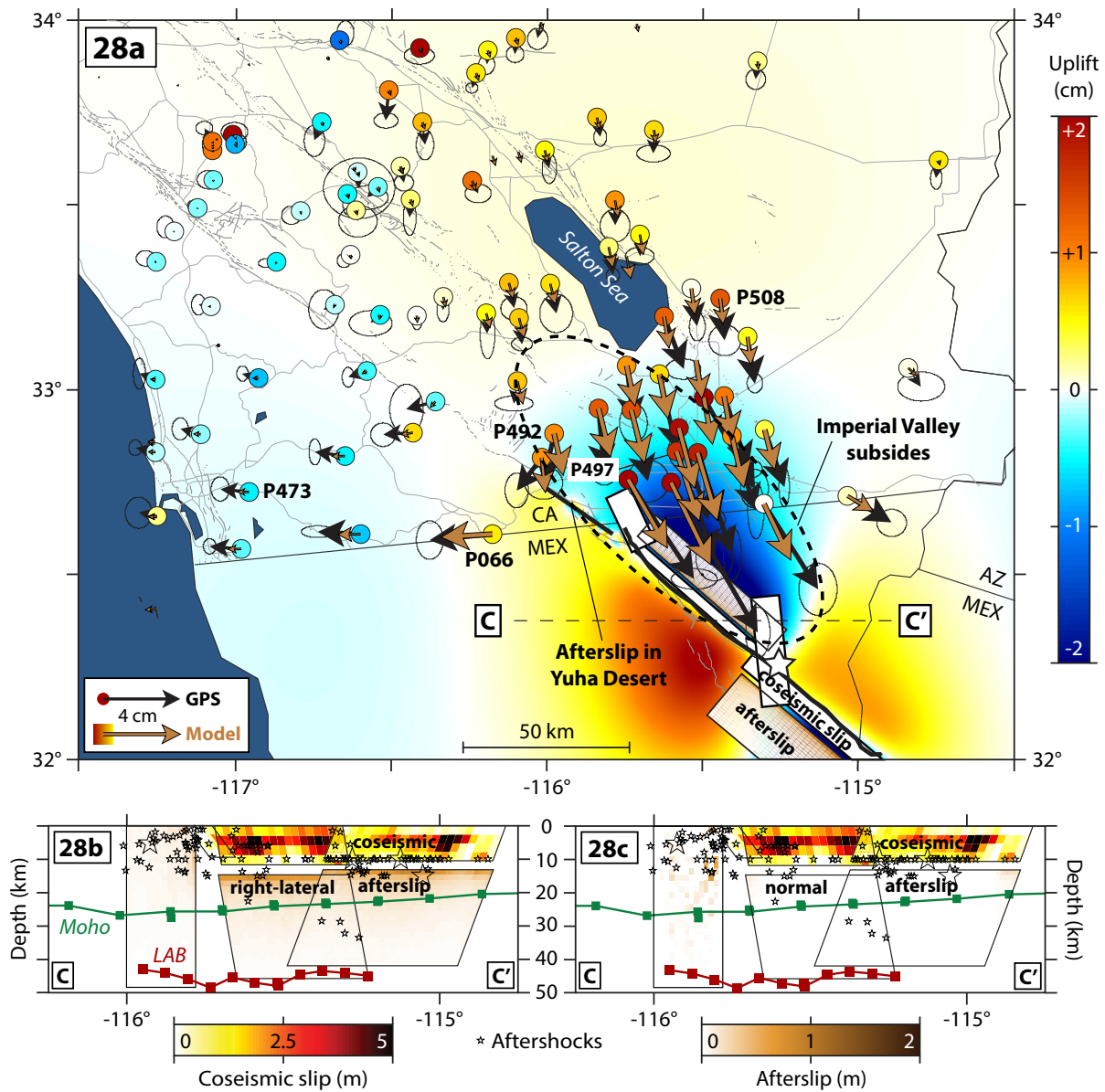


Figure 28

Forward modeling of stress-driven afterslip on modeled downward extensions of coseismic slip planes F2 and F3 in the Wei *et al.* (2011) coseismic model into the lower crust and mantle lithosphere. The afterslip is allowed between 15 and 48 km downdip from the top edges of these planes, is driven by coseismic shear stress changes and is governed by a rate-strengthening friction law with $(a - b)\sigma = 10$ MPa. Slip is also allowed on a 30-km long segment extending northwest into the Yuha Desert; this segment has a vertical dip and extends to 48 km depth.

a This afterslip model produces horizontal surface displacements with the correct azimuth but the wrong pattern of uplift and subsidence. b

c Slip decreases away from the coseismic rupture, as expected for a stress-driven mechanism

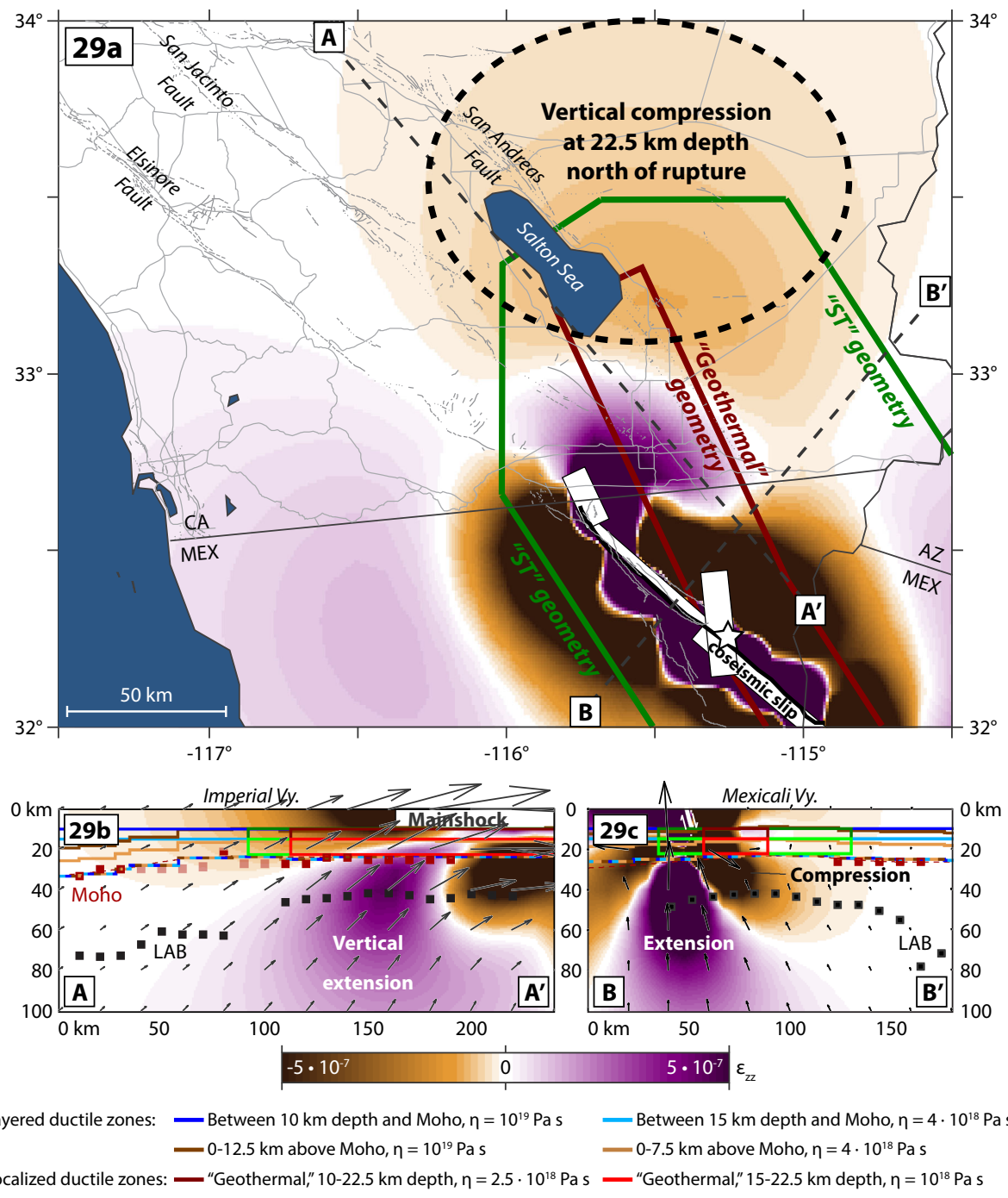


Figure 29

a Mapview and **b, c** cross sections of vertical extension (ϵ_{zz}) imparted by the mainshock at 22.5 km depth (Moho depth in the Salton Trough). The lower crust and mantle lithosphere beneath the northern Imperial Valley and beneath the rupture underwent vertical compression during the mainshock

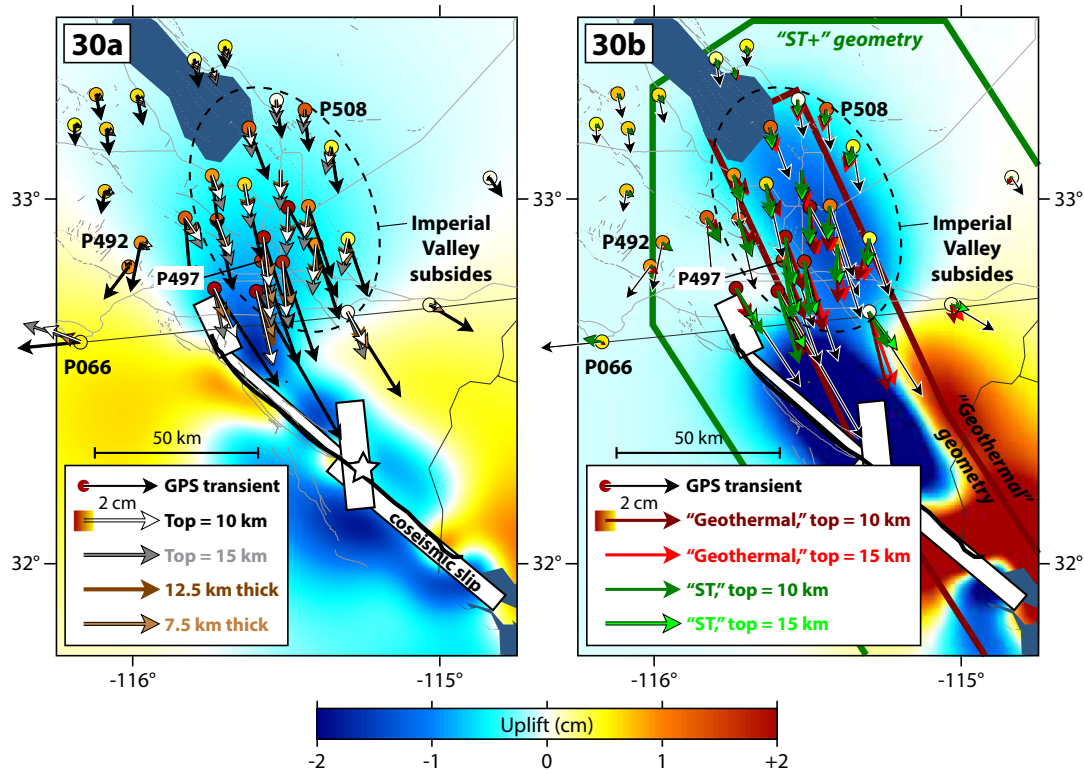


Figure 30

Synthetic three-year surface displacements at GPS stations generated by Newtonian viscoelastic relaxation in the modeled lower crustal ductile zones. All eight models produce subsidence in the Imperial Valley (Fig. 9). **a** Horizontal displacements from the four models with geometries that are not confined to the Salton Trough. Vertical displacements from the model prescribing viscoelastic relaxation between 10 km depth and the Moho. **b** Horizontal displacements from the four models with geometries localized within the Salton Trough. Vertical displacements from the model prescribing viscoelastic relaxation in the “geothermal” geometry below 10 km depth

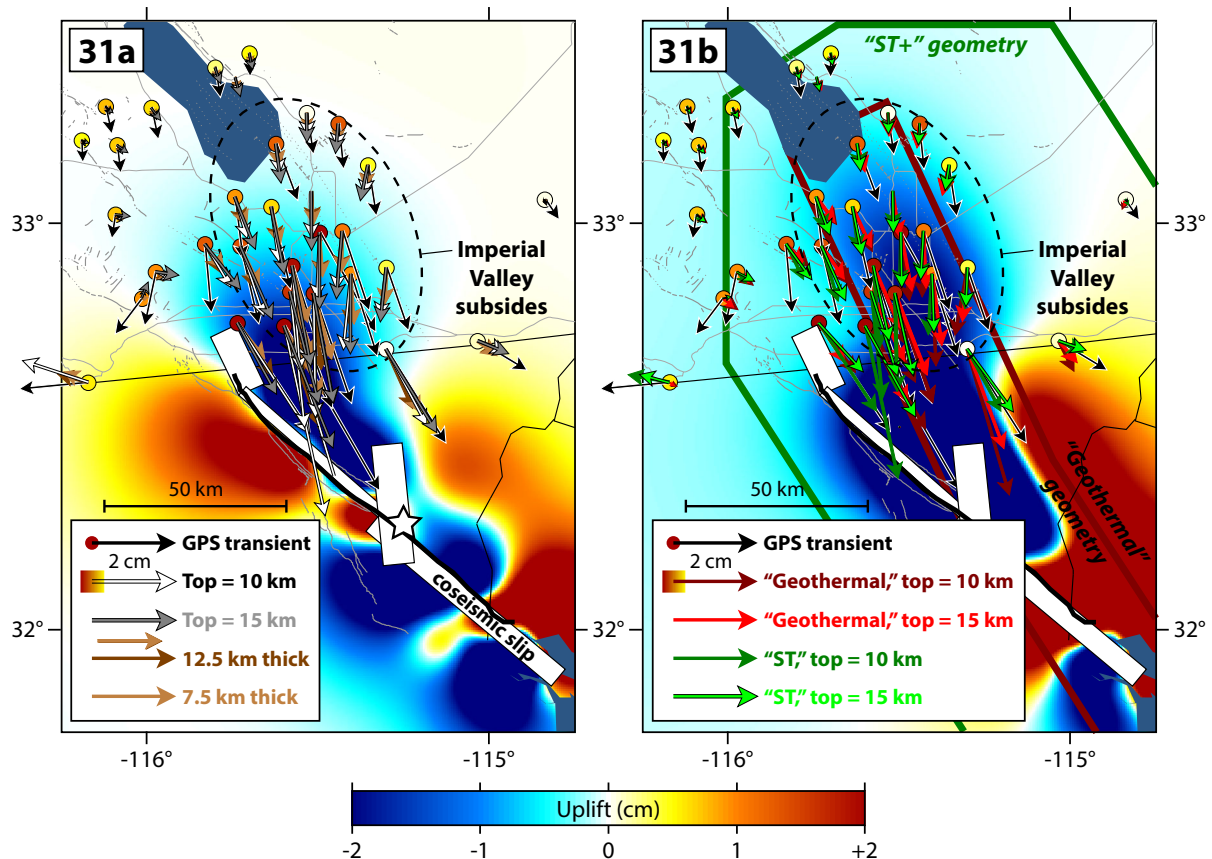


Figure 31

Synthetic three-year surface displacements at GPS stations generated by viscoelastic relaxation with a stress-dependent viscosity ($n = 2.5$) in the modeled lower crustal ductile zones. All eight models produce subsidence in the Imperial Valley (Fig. 32). **a** Horizontal displacements from the four models with geometries that are not confined to the Salton Trough. Vertical displacements from the model prescribing viscoelastic relaxation between 10 km depth and the Moho. **b** Horizontal displacements from the four models with geometries localized within the Salton Trough. Vertical displacements from the model prescribing viscoelastic relaxation in the “geothermal” geometry below 10 km depth

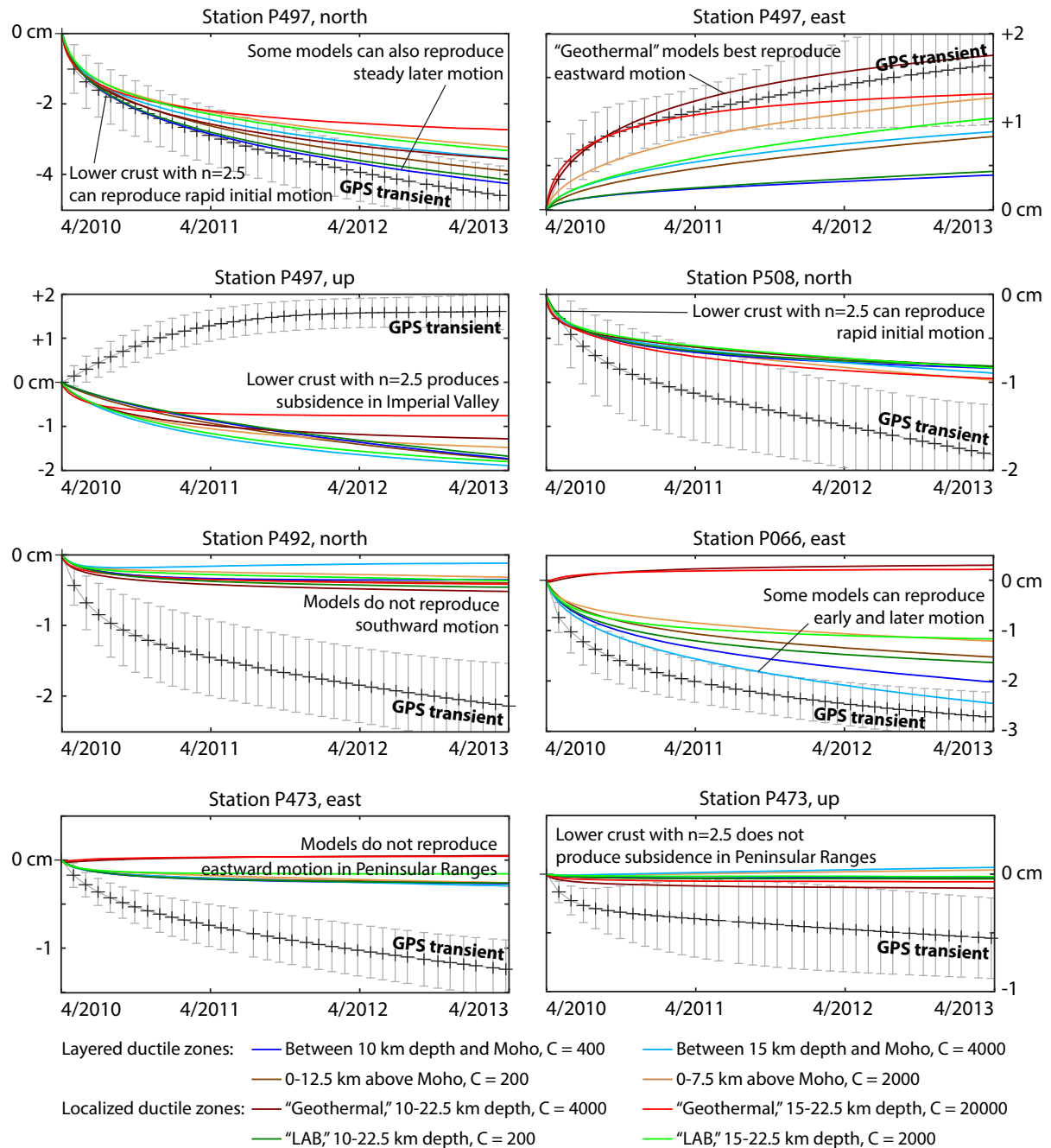


Figure 32

Synthetic time series of surface displacement at several GPS stations (locations indicated in Fig. 30) generated by viscoelastic relaxation with a stress-dependent viscosity ($n = 2.5$) in the modeled lower crustal ductile zones

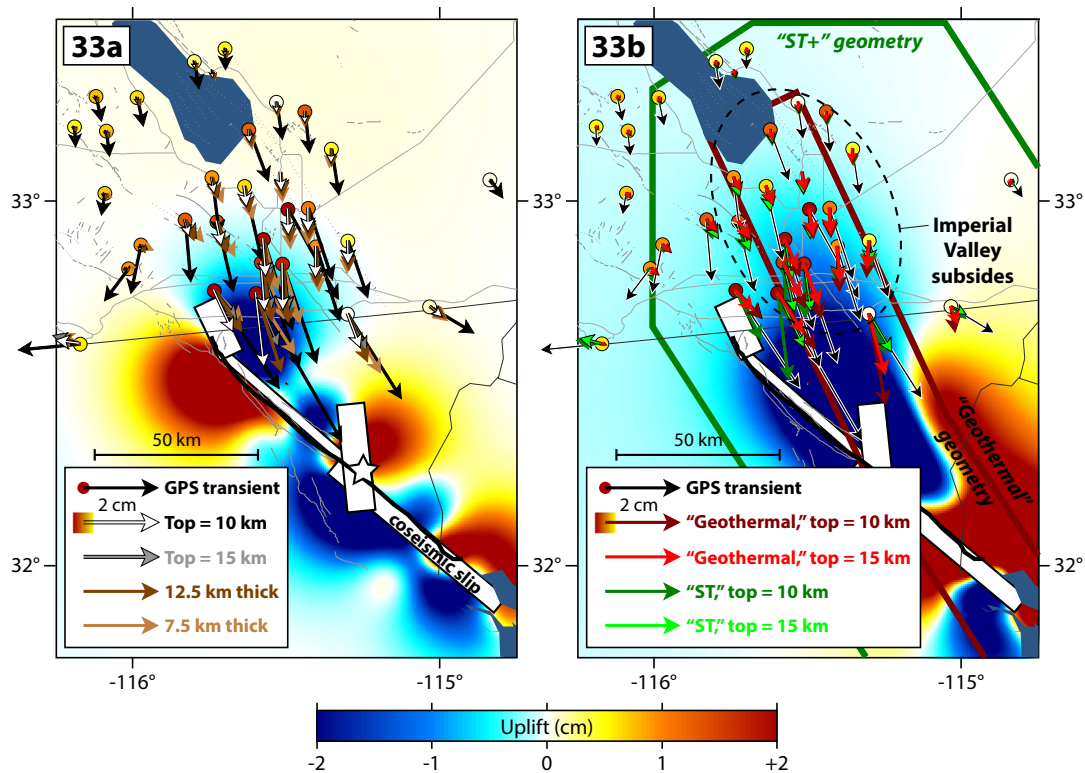


Figure 33

Synthetic three-year surface displacements at GPS stations generated by viscoelastic relaxation with a stress-dependent viscosity ($n = 4$) in the modeled lower crustal ductile zones. All eight models produce subsidence in the Imperial Valley (Fig. 34). **a** Horizontal displacements from the four models with geometries that are not confined to the Salton Trough. Vertical displacements from the model prescribing viscoelastic relaxation between 10 km depth and the Moho. **b** Horizontal displacements from the four models with geometries localized within the Salton Trough. Vertical displacements from the model prescribing viscoelastic relaxation in the "geothermal" geometry below 10 km depth

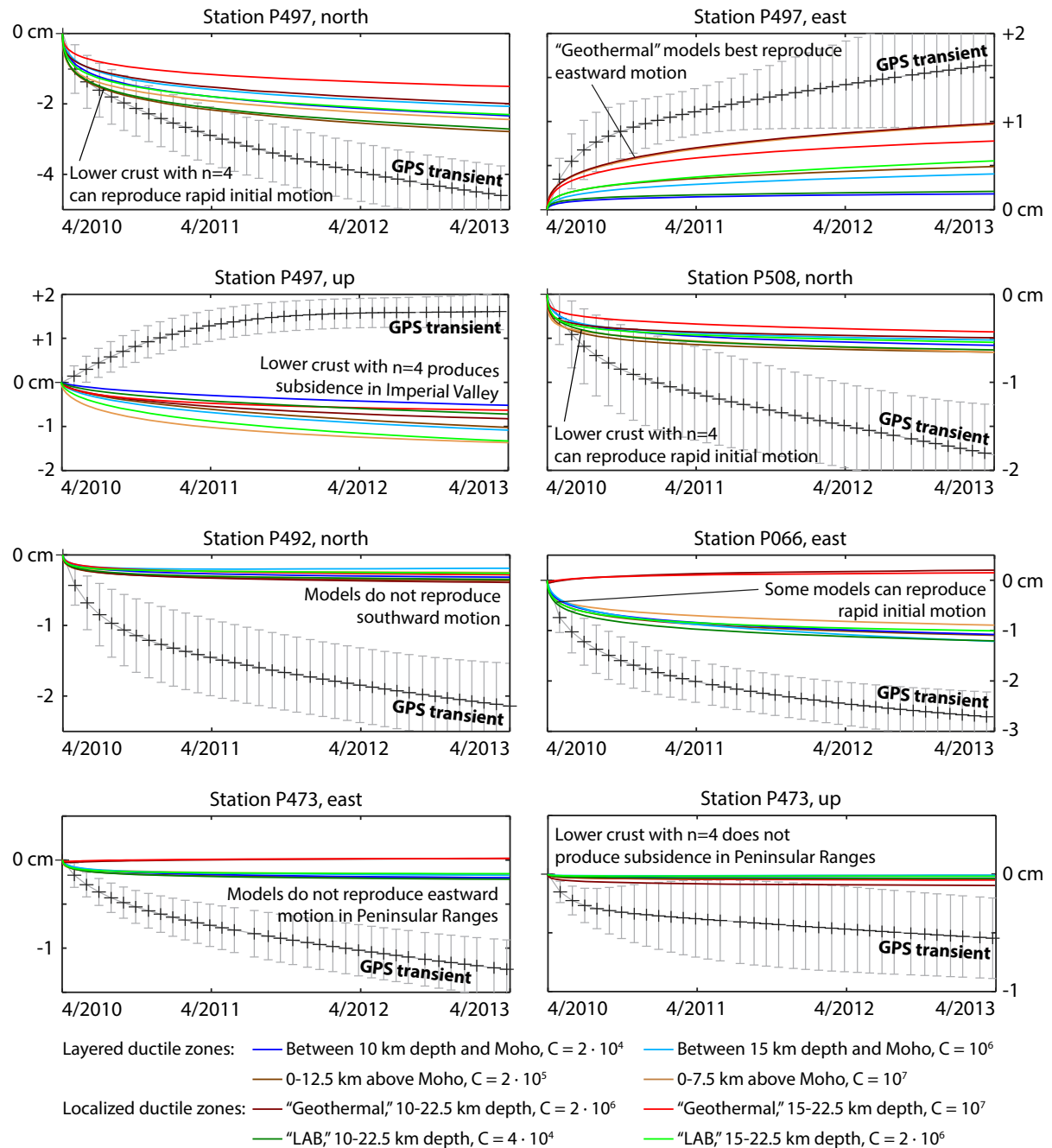


Figure 34

Synthetic time series of surface displacement at several GPS stations (locations indicated in Fig. 30) generated by viscoelastic relaxation with a stress-dependent viscosity ($n = 4$) in the modeled lower crustal ductile zones

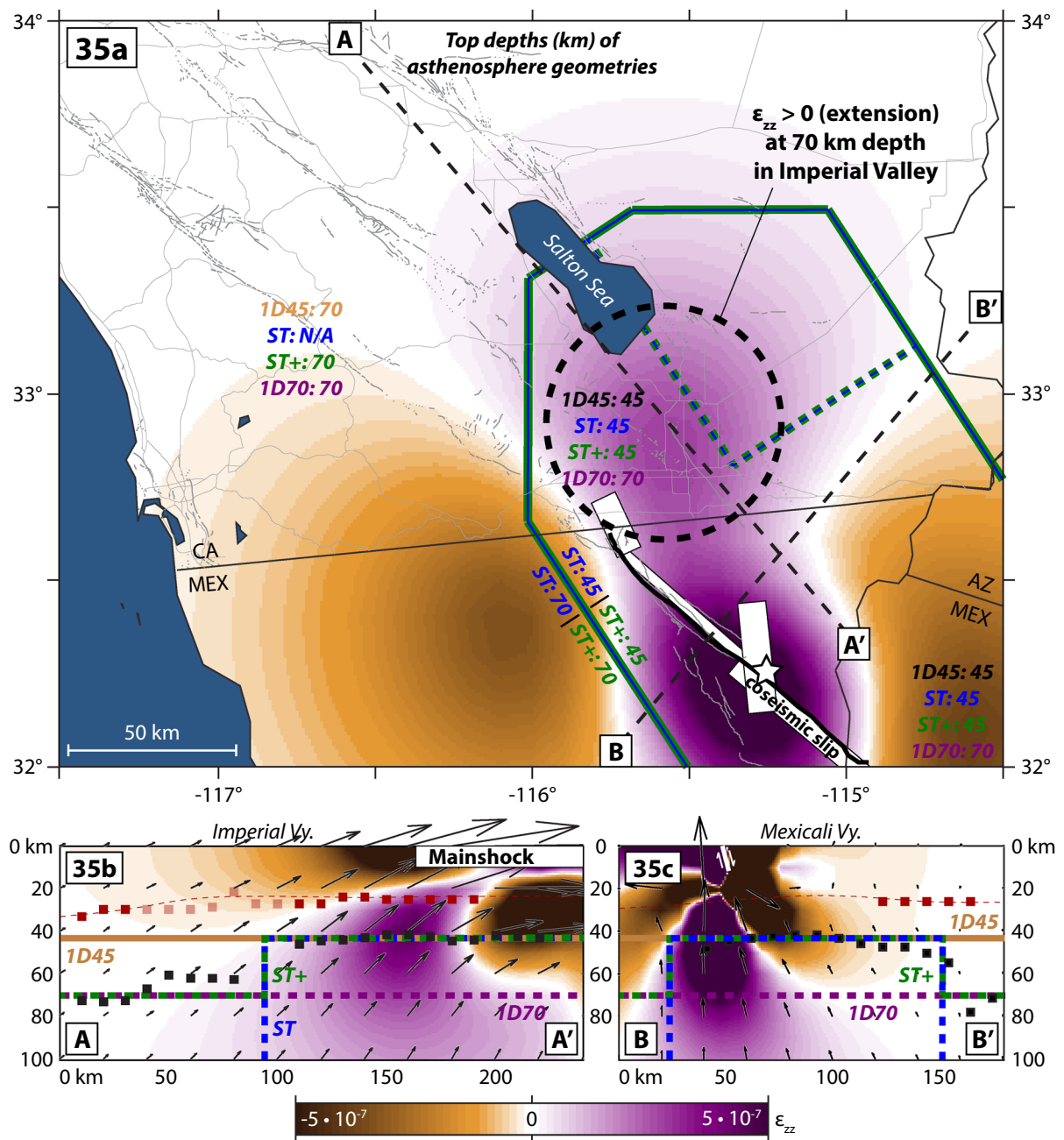


Figure 35

a Mapview and **b, c** cross sections of vertical extension (ϵ_{zz}) imparted by the mainshock at 70 km depth, which is within the asthenosphere in all three model geometries we use. The mainshock imparted vertical extension at 70 km depth beneath the Imperial Valley and beneath the central part of the rupture

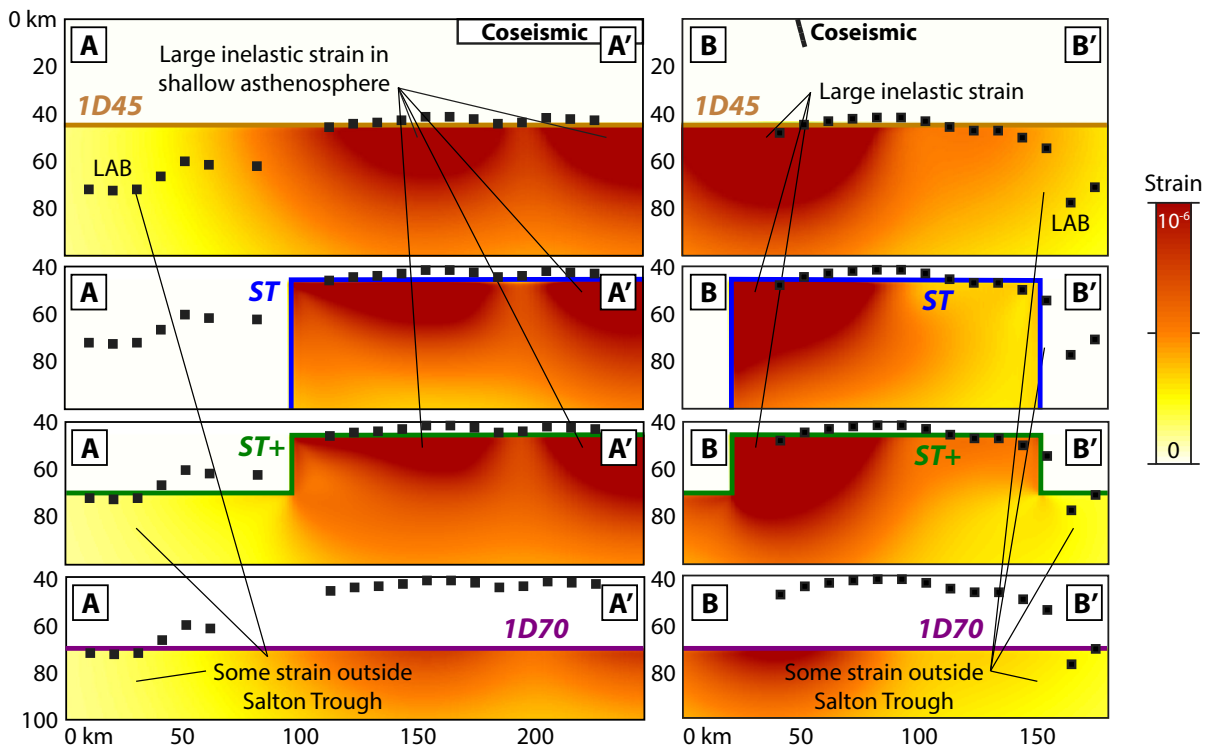


Figure 36

Cross sections of cumulative inelastic (viscous) strain after three years of Newtonian viscoelastic relaxation in the four geometries for the asthenosphere show that although the major viscoelastic relaxation is concentrated close to the rupture, some inelastic strain does occur outside of the Salton Trough

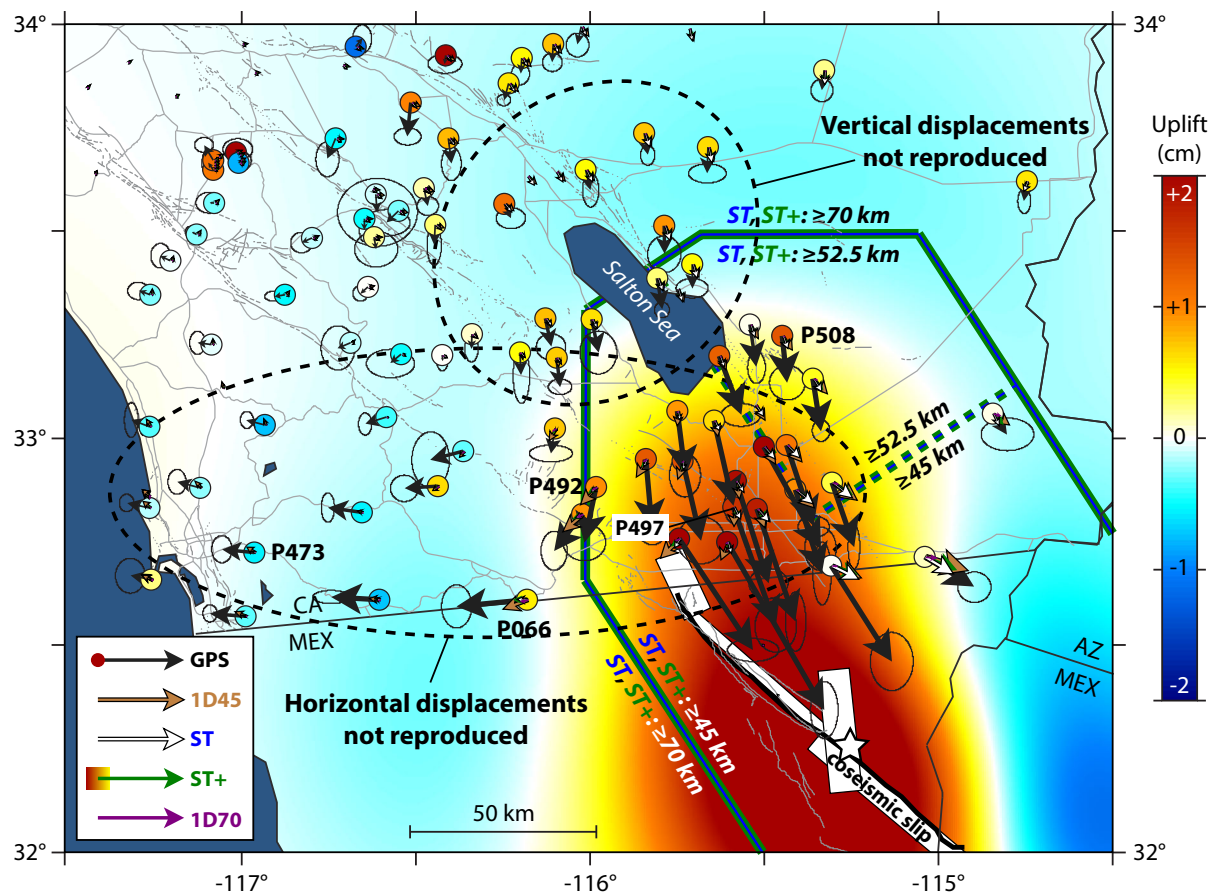


Figure 37

Three-year cumulative surface displacements from viscoelastic relaxation with a stress-dependent viscosity ($n = 3.5$) in the four modeled geometries for the asthenosphere. This mechanism can to some extent reproduce the uplift in the Imperial Valley but does not reproduce the amplitude of subsidence observed in the Peninsular Ranges or the horizontal displacements observed anywhere in southern California

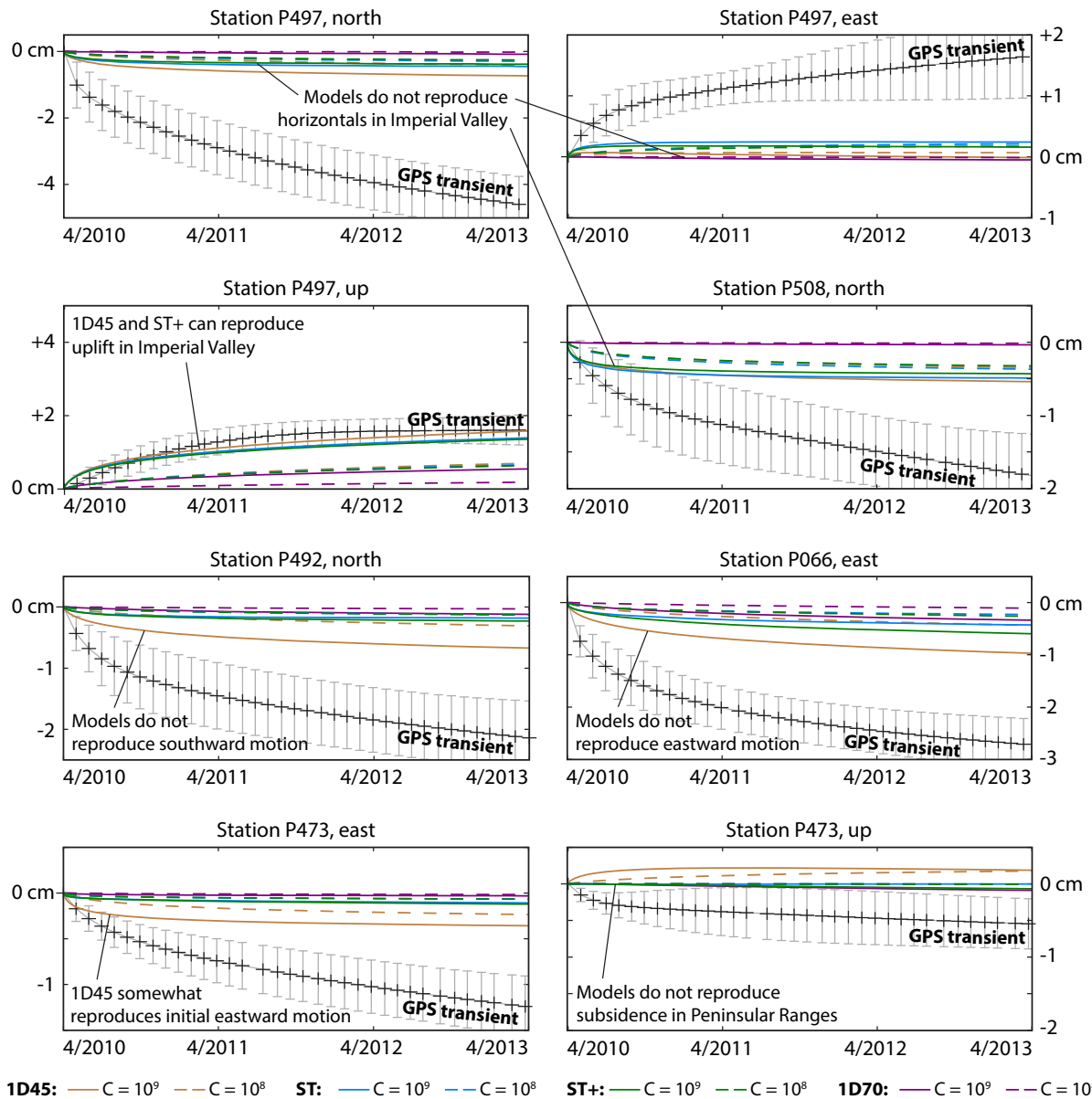


Figure 38

Synthetic time series of surface displacement at several GPS stations (locations indicated in Fig. 37) generated by stress-dependent viscoelastic relaxation ($n = 3.5$) in the modeled geometries for the asthenosphere. This mechanism can reproduce the uplift at station P497 in the Imperial Valley and possibly the rapid early eastward motion at station P473 but no other aspect of the transient

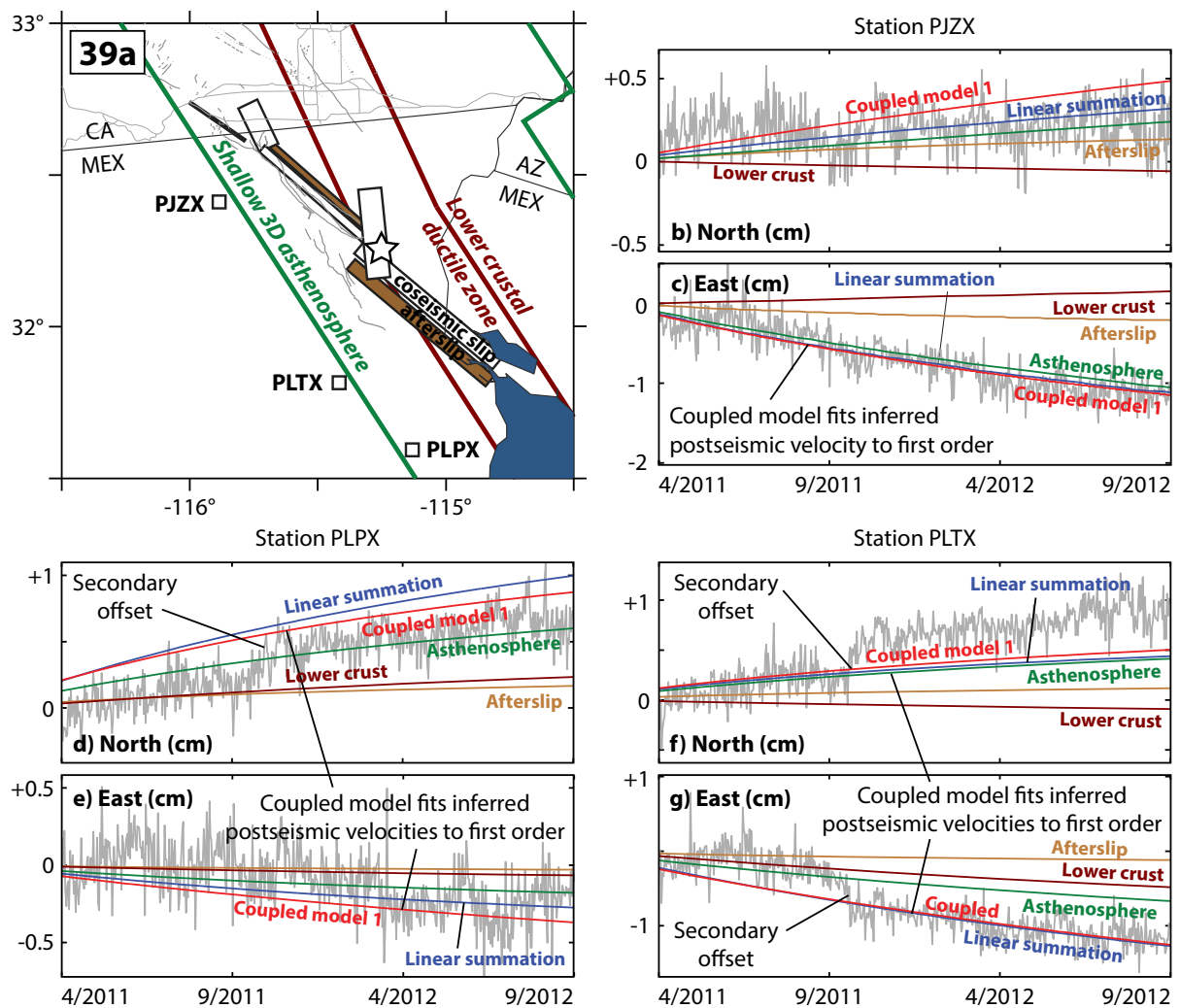


Figure 39

a Locations of stations PJZX, PLPX and PLTX in Mexico compared to the geometry of the first coupled model. **b–g** Comparison of best-fit GPS time series at stations PJZX, PLPX and PLTX in Mexico with synthetic time series of surface displacement generated by the first coupled model

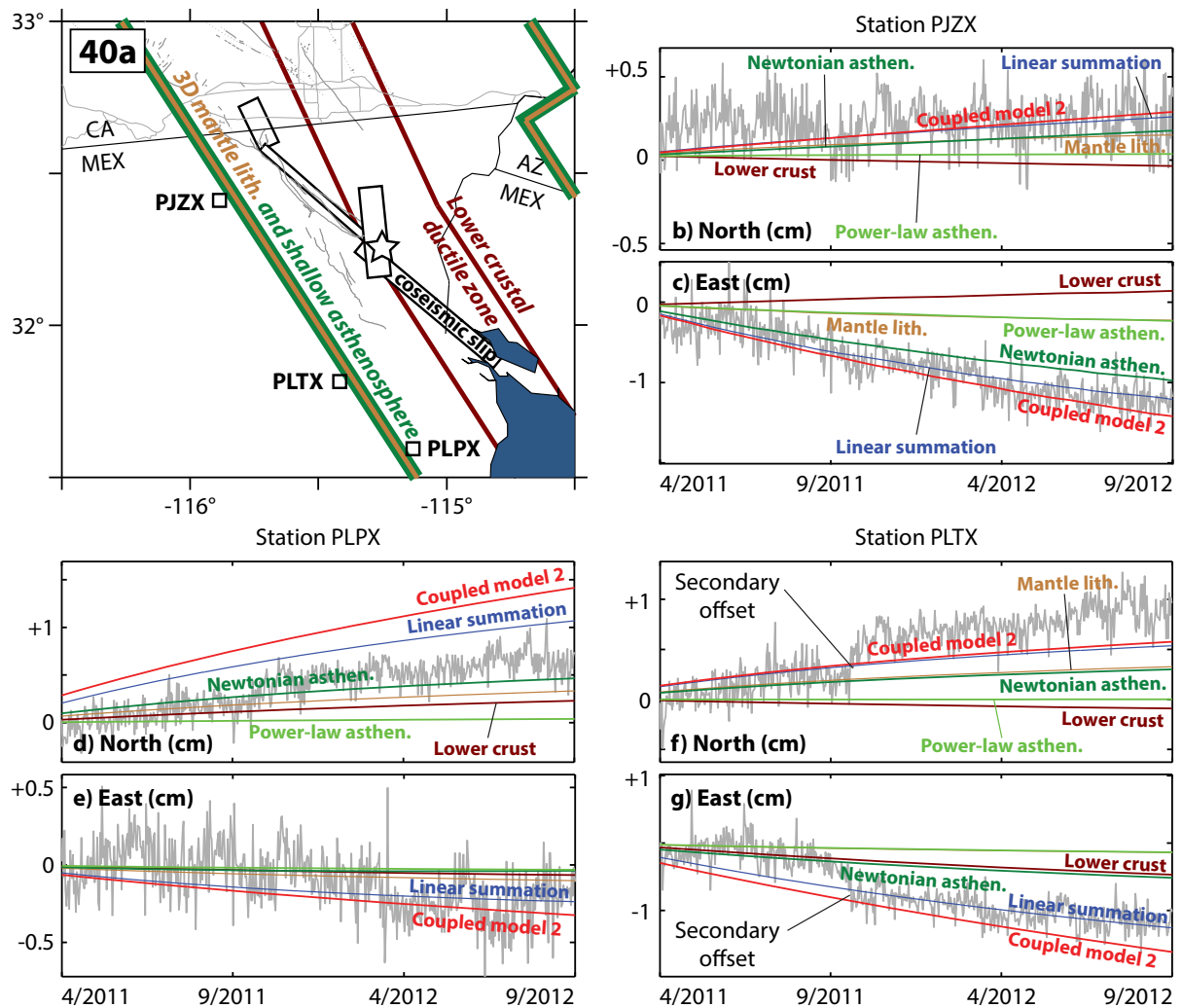


Figure 40

a Locations of stations PJZX, PLPX and PLTX in Mexico compared to the geometry of the second coupled model. **b–g** Comparison of best-fit GPS time series at stations PJZX, PLPX and PLTX in Mexico with synthetic time series of surface displacement generated by the second coupled model

REFERENCES

- BARBOT, S., and FIALKO, Y. Fourier-domain Green's function for an elastic semi-infinite solid under gravity, with applications to earthquake and volcano deformation *Geophys. J. Int.*, 182(2), 568–582, 2010a, doi:[10.1111/j.1365-246X.2010.04655.x](https://doi.org/10.1111/j.1365-246X.2010.04655.x).
- BARBOT, S., and FIALKO, Y. A unified continuum representation of postseismic relaxation mechanisms: semi-analytic models of afterslip, poroelastic rebound and viscoelastic flow, *Geophys. J. Int.*, 182(3), 1124–1140, 2010b, doi:[10.1111/j.1365-246X.2010.04678.x](https://doi.org/10.1111/j.1365-246X.2010.04678.x).
- BARBOT, S., FIALKO, Y., and BOCK, Y. Postseismic Deformation due to the Mw 6.0 2004 Parkfield Earthquake: Stress-Driven Creep
- on a Fault with Spatially Variable Rate-and-State Friction Parameters, *J. Geophys. Res.*, 114(B07405), 2009, doi:[10.1029/2008JB005748](https://doi.org/10.1029/2008JB005748).
- BARBOT, S., LAPUSTA, N., and AVOUAC, J-P. Under the hood of the earthquake machine: Towards predictive modeling of the seismic cycle, *Science*, 336, 707–710, 2012.
- BARBOT, S., AGRAM, P., SIMONS M., and DE MICHELE, M. Change of Apparent Segmentation of the San Andreas Fault Around Parkfield from Space Geodetic Observations Across Multiple Periods, *J. Geophys. Res.*, 118(12), 6311–6327, 2013.
- BILLS, B.G., ADAMS, K.D., and WESNOUSKY, S.G. Viscosity structure of the crust and upper mantle in western Nevada from isostatic rebound patterns of the late Pleistocene Lake Lahontan high shoreline, *J. Geophys. Res.*, 112(B6), 6405, 2007.

- BRUHAT, L., BARBOT, S., and AVOUAC, J.P. *Evidence for postseismic deformation of the lower crust following the 2004 $M_w 6.0$ Parkfield earthquake*, *J. Geophys. Res.*, **116**, 10, 2011.
- BÜRGMANN, R., and DRESEN, G. *Rheology of the lower crust and upper mantle: Evidence from rock mechanics, geodesy, and field observations*, *Ann. Rev. Earth Plan. Sci.*, **36**, 531–567, 2008.
- BUROV, E., *Plate Rheology and Mechanics*, Treatise Geophys., **6**, 99–151, 2007.
- CROWELL, B.W., BOCK, Y., SANDWELL, D.T., and FIALKO, Y. *Geodetic investigation into the deformation of the Salton Trough*, *J. Geophys. Res.*, **118**, 5030–5039, 2013, doi:[10.1002/jgrb.50347](https://doi.org/10.1002/jgrb.50347).
- DENG, J., GURNIS, M., KANAMORI, H., and HAUSSON, E. *Viscoelastic flow in the lower crust after the 1992 Landers California, earthquake*, *Science*, **282**(5394), 1689–1692, 1998.
- FAY, N.P., and HUMPHREYS, E.D. *Fault slip rates, effects of elastic heterogeneity on geodetic data, and the strength of the lower crust in the Salton Trough region, southern California*, *J. Geophys. Res.*, **110**(B09401), 2005.
- FIALKO, Y. *Evidence of fluid-filled upper crust from observations of post-seismic deformation due to the 1992 $M_w 7.3$ Landers earthquake*, *J. Geophys. Res.*, **109**, B08,401, 2004, doi:[10.1029/2004JB002985](https://doi.org/10.1029/2004JB002985).
- FREED, A. M., *Afterslip (and only afterslip) following the 2004 Parkfield, California, earthquake*, *Geophys. Res. Lett.*, **34**, 2007.
- FREED, A.M., and BÜRGMANN, R. *Evidence of power-law flow in the Mojave desert mantle*, *Nature*, **430**, 548–551, 2004.
- GONZALEZ-ORTEGA, A., FIALKO, Y., SANDWELL, D., NAVA-PICHARDO, F.A., FLETCHER, J., GONZALEZ-GARCIA, J., LIPOVSKY, B., FLOYD, M., and FUNNING, G., *El Mayor-Cucapah ($Mw = 7.2$) earthquake: Early near-field postseismic deformation from InSAR and GPS observations*, *J. Geophys. Res.*, **119**, 1482–1497, 2014.
- HAUSSON, E., STOCK, J., HUTTON, K., YANG, W., VIDAL-VILLEGAS, J.A., and KANAMORI, H., *The 2010 $Mw 7.2$ El Mayor-Cucapah Earthquake Sequence, Baja California, Mexico and Southernmost California, USA: Active Seismotectonics along the Mexican Pacific Margin*, *Pure App. Geophys.*, **168**(8–9), 1255–1277, 2011.
- HEARN, E., BÜRGMANN, R., and REILINGER, R., *Dynamics of Izmit earthquake postseismic deformation and loading of the Duzce earthquake hypocenter*, *Bull. Seism. Soc. Am.*, **92**, 172–193, 2002.
- HEARN, E., and BÜRGMANN, R., *The Effect of Elastic Layering on Inversions of GPS Data for Coseismic Slip and Resulting Stress Changes: Strike-Slip Earthquakes*, *Bull. Seism. Soc. Am.*, **95**(5), 2005, doi:[10.1029/2008JB006026](https://doi.org/10.1029/2008JB006026).
- HIRTH, G., and KOHLSTEDT, D.L., *Rheology of the upper mantle and the mantle wedge: a view from the experimentalists*, In: EILER J., Inside the Subduction Factory, *Geophys. Monogr.*, vol. 138, pp. 83–105, Am. Geophys. Soc., Washington, DC, 2003.
- JOHNSON, K.M., BÜRGMANN, R., and FREYMUELLER, J.T., *Coupled afterslip and viscoelastic flow following the 2002 Denali Fault, Alaska earthquake*, *Geophys. J. Int.*, **176**(3), 670–682, 2009.
- JONSSON, S., SEGALL, P., PEDERSEN, R., and BJORNSSON, G., *Post-earthquake ground movements correlated to pore-pressure transients*, *Nature*, **424**, 179–183, 2003.
- KARATO, S.-I., *Deformation of Earth Materials: An Introduction to the Rheology of Solid Earth*, Cambridge Univ. Press, Cambridge, UK, 2008.
- KAUFMANN, G., and AMELUNG, F., *Reservoir-induced deformation and continental rheology in vicinity of Lake Mead, Nevada*, *J. Geophys. Res.*, **105**, 16,341–16,358, 2000.
- KIRBY, S. H., *Rheology of the Lithosphere*, *Rev. Geophys.*, **21**(6), 1458–1487, 1983.
- KROLL, K., COCHRAN, E., RICHARDS-DINGER, K., and SUMY, D., *Aftershocks of the 2010 $Mw 7.2$ El Mayor-Cucapah earthquake reveal complex faulting in the Yuha Desert, California*, *J. Geophys. Res.*, **118**, 2013, doi:[10.1002/2013JB010529](https://doi.org/10.1002/2013JB010529).
- LACHENBRUCH, A.H., SASS, J.H., and GALANIS, S.P., *Heat flow in southernmost California and the origin of the Salton Trough*, *J. Geophys. Res.*, **90**(B8), 6709–6736, 1985, doi:[10.1029/JB090iB08p06709](https://doi.org/10.1029/JB090iB08p06709).
- LEKIC, V., FRENCH, S.W., and FISCHER, K.M., *Lithospheric Thinning Beneath Rifting Regions of Southern California*, *Sci. Exp.*, 2011.
- LIN, J., and STEIN, R.S., *Stress triggering in thrust and subduction earthquakes, and stress interaction between the southern San Andreas and nearby thrust and strike-slip faults*, *J. Geophys. Res.*, **109**(B04401), 2004, doi:[10.1029/2003JB002607](https://doi.org/10.1029/2003JB002607).
- LUTTRELL, K., SANDWELL, D., SMITH-KONTER, B., BILLS, B., and BOCK, Y., *Modulation of the earthquake cycle at the southern San Andreas fault by lake loading*, *J. Geophys. Res.*, **112**(B08411), 2007, doi:[10.1029/2006JB004752](https://doi.org/10.1029/2006JB004752).
- MALSERVISI, R., PLATTNER, C., HACKL, M., and SUAREZ-VIDAL, F., *Implication of the Central Gulf of California (MX) Earthquake cycle in understanding continental plate boundary rheology*, *Eos Trans. AGU*, **93**(51), 2012.
- MARONE, C., SCHOLZ, C.H., and BILHAM, R., *On the mechanics of earthquake afterslip*, *J. Geophys. Res.*, **96**, 8441–8452, 1991.
- MARONE, C. J., *Laboratory-derived friction laws and their application to seismic faulting*, *An. Rev. Earth Planet. Sc.*, **26**, 643–696, 1998.
- MEADE, B., KLINGER, Y., and HETLAND, E., *Inference of multiple earthquake-cycle relaxation timescales from irregular geodetic sampling of interseismic deformation*, *BSSA*, **103**(5), 2824–2835, 2013, doi:[10.1785/0120130006](https://doi.org/10.1785/0120130006).
- MIYAZAKI, S., SEGALL, P., FUKUDA, J., and KATO, T., *Space Time Distribution of Afterslip Following the 2003 Tokachi-oki Earthquake: Implications for Variations in Fault Zone Frictional Properties*, *Geophys. Res. Lett.*, **31**(L06623), 2004, doi:[10.1029/2003GL019410](https://doi.org/10.1029/2003GL019410).
- MONTÉSI, L.G.J., and HIRTH, G., *Grain size evolution and the rheology of ductile shear zones: from laboratory experiments to postseismic creep*, *Earth Planet. Sci. Lett.*, **211**, 97–110, 2003.
- NUR, A., and MAVKO, G., *Postseismic viscoelastic rebound*, *Science*, **183**, 204–206, 1974.
- ORTEGA, F., *Aseismic Deformation in Subduction Megathrusts: Central Andes and North-East Japan*, Ph.D. thesis, California Institute of Technology, 2013.
- PELTZER, G., ROSEN, P., ROGEZ, F., and HUDNUT, K., *Poro-elastic rebound along the Landers 1992 earthquake surface rupture*, *J. Geophys. Res.*, **103**(B12), 30,131–30,145, 1998.
- PERFETTINI, H., and AVOUAC, J.-P., *Postseismic relaxation driven by brittle creep: a possible mechanism to reconcile geodetic measurements and the decay rate of aftershocks, application to the Chi-Chi earthquake, Taiwan*, *J. Geophys. Res.*, **109**(B02304), 2004.
- PERFETTINI, H., and AVOUAC, J.-P., *Modeling afterslip and aftershocks following the 1992 Landers earthquake*, *J. Geophys. Res.*, **112**(B07409), 2007.
- PLATTNER, C., MALSERVISI, R., DIXON, T., LAFEMINA, P., SELLA, G., FLETCHER, J., and SUAREZ-VIDAL, F., *New constraints on relative motion between the Pacific plate and Baja California microplate (Mexico) from GPS measurements*, *GJI*, 2007, doi:[10.1111/j.1365-246X.2007.03494.x](https://doi.org/10.1111/j.1365-246X.2007.03494.x).

- POLLITZ, F. F., *Post-seismic relaxation theory on a laterally heterogeneous viscoelastic model*, *Geophys. J. Int.*, **155**, 55–78, 2003.
- POLLITZ, F.F., BÜRGMANN, R., and THATCHER, W., *Illumination of rheological mantle heterogeneity by the m7.2 2010 el mayor-cucapah earthquake*, *Geochem. Geophys. Geosyst.*, **13**, 2012, doi:[10.1029/2012GC004139](https://doi.org/10.1029/2012GC004139).
- RYMER, M., et al., Triggered Surface Slips in Southern California Associated with the 2010 El Mayor-Cucapah, Baja California, Earthquake, US Geological Survey Open-File Report 2010-1333 and California Geological Survey Special Report 221, 2011.
- SEGALL, P., Earthquake and volcano deformation, Princeton University Press, Princeton, NJ, 2010.
- TAKEUCHI, C.S., and FIALKO, Y., *On the effects of thermally weakened ductile shear zones on postseismic deformation*, *J. Geophys. Res.*, 2013, doi:[10.1002/2013JB010215](https://doi.org/10.1002/2013JB010215).
- TAPE, C., PLESCH, A., SHAW, J.H., and GILBERT, H., *Estimating a Continuous Moho Surface for the California Unified Velocity Model*, *Seism. Res. Lett.*, **83**(4), 728–735, 2012.
- TODA, S., STEIN, R.S., RICHARDS-DINGER, K., and BOZKURT, S.B., *Forecasting the evolution of seismicity in southern California: Animations built on earthquake stress transfer*, *J. Geophys. Res.*, **110**(B05S16), 17, 2005, doi:[10.1029/2004JB003415](https://doi.org/10.1029/2004JB003415).
- WEI, S., et al., *Superficial simplicity of the 2010 El Mayor-Cucapah earthquake of Baja California in Mexico*, *Nature Geosci.*, 615–618, 2011.
- WILLIAMS, C.F., DEANGELO, J., and SASS, J.H., *Heat Flow in the Salton Trough Revisited and Implications for Regional Tectonics*, *Eos Trans. AGU*, **93**(51), 2012.

(Received March 3, 2014, revised November 26, 2014, accepted November 27, 2014, onlinel date January 21, 2015)